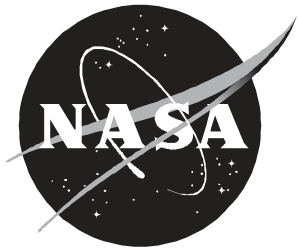

NASA Technical Paper 3495

HZETRN: Description of a Free-Space Ion and Nucleon Transport and Shielding Computer Program

John W. Wilson
Langley Research Center • Hampton, Virginia

Francis F. Badavi
Christopher Newport University • Newport News, Virginia

Francis A. Cucinotta and Judy L. Shinn
Langley Research Center • Hampton, Virginia

Gautam D. Badhwar
Johnson Space Center • Houston, Texas

R. Silberberg
Universities Space Research Association • Washington, D.C.

C. H. Tsao
Naval Research Laboratory • Washington, D.C.

Lawrence W. Townsend
Langley Research Center • Hampton, Virginia

Ram K. Tripathi
Christopher Newport University • Newport News, Virginia

May 1995

Available electronically at the following URL address: http://techreports.larc.nasa.gov/ltrs/ltrs.html

Printed copies available from the following:

NASA Center for AeroSpace Information
800 Elkridge Landing Road
Linthicum Heights, MD 21090-2934
(301) 621-0390

National Technical Information Service (NTIS)
5285 Port Royal Road
Springfield, VA 22161-2171
(703) 487-4650

Contents

Abstract

The high-charge-and-energy (HZE) transport computer program HZETRN is developed to address the problems of free-space radiation transport and shielding. The HZETRN program is intended specifically for the design engineer who is interested in obtaining fast and accurate dosimetric information for the design and construction of space modules and devices. The program is based on a one-dimensional space-marching formulation of the Boltzmann transport equation with a straight-ahead approximation. The effect of the long-range Coulomb force and electron interaction is treated as a continuous slowing-down process. Atomic (electronic) stopping power coefficients with energies above a few A MeV are calculated by using Bethe's theory including Bragg's rule, Ziegler's shell corrections, and effective charge. Nuclear absorption cross sections are obtained from fits to quantum calculations and total cross sections are obtained with a Ramsauer formalism. Nuclear fragmentation cross sections are calculated with a semiempirical abrasion-ablation fragmentation model. The relation of the final computer code to the Boltzmann equation is discussed in the context of simplifying assumptions. A detailed description of the flow of the computer code, input requirements, sample output, and compatibility requirements for non-VAX platforms are provided.

1. Introduction

During the last 40 years, propagation of galactic ions through extended matter and determination of the origin of these ions have been the subject of many studies. Peters (ref. 1) used the one-dimensional equilibrium solution, without including ionization energy loss and radioactive decay, to show that the light ions have their origin in the breakup of heavy particles. Davis (ref. 2) showed that one-dimensional propagation is simplistic and that leakage at the galactic boundary must be taken into account. Ginzburg and Syrovatskii (ref. 3) argued that the leakage can be approximated as a superposition of nonequilibrium one-dimensional solutions. The solution to the steady-state equations was given as a Volterra equation by Gloeckler and Jokipii (ref. 4), which was solved to the first order in the fragmentation cross sections by ignoring energy loss. This provided an approximation of the first-order solution that included ionization energy loss and was only valid at relativistic energies. Lezniak (ref. 5) gave an overview of the cosmic ray propagation and derived a Volterra equation that included the ionization energy loss and evaluated only the unperturbed term. The previous discussion indicates, that for a long time, the main interest of cosmic ray physicists was to achieve first-order solutions in the fragmentation cross sections where path lengths in the interstellar space are on the order of 3 to 4 g/cm^2. Clearly, higher order terms cannot be ignored in accelerator or space shielding transport problems. (See refs. 6–9.) Besides this simplification, previous cosmic ray models have neglected the complicated three-dimensional nature of the fragmentation process.

Several approaches to the solution of high-energy heavy ion propagation that include ionization energy loss have been developed (refs. 6–19) during the last 20 years. All but one (ref. 6) have assumed the straight-ahead approximation and velocity-conserving fragmentation interactions. Only two (refs. 6 and 9) have incorporated energy-dependent cross sections. The approach by Curtis, Doherty, and Wilkinson (ref. 14) for a primary ion beam represented the first-generation secondary fragments as a quadrature over the collision density of the primary beam. Allkofer and Heinrich (ref. 15) used an energy multigroup method in which an energy-independent fragmentation transport approximation was applied within each energy group after which the energy group boundaries were moved according to continuous slowing-down theory. Chatterjee, Tobias, and Lyman (ref. 16) solved

the energy-independent fragment transport equation with primary collision density as a source and neglected higher order fragmentation. The primary source term extended only to the primary ion range from the boundary and the energy-independent transport solution was modified to account for the finite range of the secondary fragment ions.

Wilson (ref. 7) derived an expression for the ion transport problem to the first-order (i.e., first-collision) term and gave an analytical solution for the depth-dose relationship. The more common approximations used in solving the heavy ion transport problem were examined further by Wilson. (See ref. 6.) The effect of conservation of velocity on fragmentation and on the straight-ahead approximation was found to be negligible for cosmic ray applications. Solution methods for representation of the energy-dependent nuclear cross sections were derived. (See ref. 6.) Letaw, Tsao, and Silberberg (ref. 17) approximated the energy loss term and the ion spectra by simple forms for which energy derivatives were evaluated explicitly. The resulting ordinary differential equations in terms of position were solved analytically. This approximation results in the decoupling of motion in space and a change in energy. In Letaw's formalism, the energy shifts were replaced by an effective attenuation factor. Wilson (ref. 8) added the next higher order (i.e., second-collision) term. This term was found to be very important in describing ^{20}Ne beams at 670*A* MeV. The three-term expansion was modified to include the effect of energy variation of the nuclear cross sections. (See ref. 9.) The integral form of the transport equation was also used to derive a numerical marching procedure to solve the cosmic ray transport problem. (See refs. 6 and 12.) This method could accommodate the energy-dependent nuclear cross sections within the numerical procedure. Comparison of the numerical procedure with an analytical solution of a simplified problem (refs. 12 and 13) validated the solution technique to approximately 1-percent accuracy. Several solution techniques and analytical methods have also been developed for testing future numerical solutions of the transport equation. (See refs. 18 and 19.) More recently, an analytical solution for the laboratory ion beam transport problem has been derived with a straight-ahead approximation, velocity conservation at the interaction site, and energy-dependent nuclear cross sections. (See ref. 10.)

From an overview of these past developments, the applications are divided into two categories: a single-ion species with a single energy at the boundary and a broad host of elemental types with a broad continuous energy spectrum. Techniques, which will represent the spectrum over an array of energy values, require vast computer storage and computation speed to maintain sufficient energy resolution for the laboratory beam problem. In contrast, analytical methods (ref. 6), which are applied as a marching procedure (ref. 12) have similar energy resolution problems. This is a serious limitation because a final (i.e., production) high-charge-and-energy (HZE) computer code for cosmic ray shielding must be thoroughly validated by laboratory experiments; some hope exists of having a single code which can be validated in the laboratory. (See refs. 9, 10, 20, and 21.) More recently, a Green's function has been derived which has promise for a code which can be tested in the laboratory and used on space radiation protection applications. (See ref. 22.)

In this paper, the starting point is the derivation of the general Boltzmann equation. By using standard assumptions to derive the straight-ahead equation in the continuous slowing-down approximation and the assumption that heavy projectile breakup conserves velocity, the Boltzmann equation is simplified. A numerical procedure is derived with the coupling of heavy ions to the nucleon fields. Numerical stability and error propagation are discussed. The environmental model required as input to the HZE transport computer program HZETRN is briefly discussed. Atomic and nuclear models used to obtain the transport coefficients are discussed. Monte Carlo results are compared with the numerical procedures and database. Sample results for solar minimum and maximum periods are provided. Detailed descriptions of the flow of the computer code, input requirements, sample output, and compatibility requirements for non-VAX platforms are provided. This program, which is designated LAR-15225, is available through NASA's software technology transfer center COSMIC (Computer Software Management and Information Center) at 382 E. Broad Street, University of Georgia, Athens, GA 30602.

2. Derivation of Boltzmann Equation

Because the volume of any material is mostly electrons, the interaction of energetic ions passing through any material is primarily with these electrons. The cross section for the interactions of electrons is $\sigma^{at} \approx 10^{-16}$ cm^2. The long range of the nuclear Coulomb field also presents a sizable cross section of $\sigma^{c} \approx 10^{-19}$ cm^2 to the passing ion. Ion collisions are dominated by these two processes, but individual collisions have little effect on the passing ions.

Although most collisions in the material are Coulomb collisions with orbital electrons and nuclei, the rare nuclear reactions are of importance because of the significant energy transferred in the reaction and the generation of new energetic particles. The transfer of kinetic energy into new secondary radiations occurs through several processes such as direct knockout of nuclear constituents, resonant excitation followed by particle emission, pair production, and possible coherent effects within the nucleus. Through these processes, a single particle incident on a shield may attenuate through energy transfer to electrons of the media or generate a multitude of secondaries which cause an increase in exposure. The process that dominates depends on energy, particle type, and material composition.

The relevant transport equations are derived on the basis of conservation principles by considering a region of space filled with matter described by appropriate atomic and nuclear cross sections. In figure 1, a small portion of such a region enclosed by a sphere of radius δ is shown. The number of particles of type j leaving a surface element $\delta^2\, d\vec{\Omega}$ is given as $\phi_j\left(\vec{x} + \delta\vec{\Omega}, \vec{\Omega}, E\right)\delta^2\, d\vec{\Omega}$, where $\phi_j\left(\vec{x}, \vec{\Omega}, E\right)$ is the particle flux density, $\vec{x}$ is a vector to the center of the sphere, $\vec{\Omega}$ is normal to the surface element, and E is the particle energy. The projection of the surface element through the sphere center to the opposite side of the sphere defines a flux tube through which pass a number of particles of type j given as $\phi_j\left(\vec{x} - \delta\vec{\Omega}, \vec{\Omega}, E\right)\delta^2\, d\vec{\Omega}$, which would equal the number leaving the opposite face if the tube defined by the projection were a vacuum. The two numbers of particles differ by the gains and losses created by atomic and nuclear collisions as follows:

$$\begin{aligned}\phi_j\left(\vec{x} + \delta\vec{\Omega}, \vec{\Omega}, E\right)\delta^2\, d\vec{\Omega} = {} & \phi_j\left(\vec{x} - \delta\vec{\Omega}, \vec{\Omega}, E\right)\delta^2\, d\vec{\Omega} \\ & + \delta^2\, d\vec{\Omega}\int_{-\delta}^{\delta} dl \sum_k \int \sigma_{jk}\left(\vec{\Omega}, \vec{\Omega}', E, E'\right)\phi_k\left(\vec{x} + l\vec{\Omega}, \vec{\Omega}', E'\right)d\vec{\Omega}'\, dE' \\ & - \delta^2\, d\vec{\Omega}\int_{-\delta}^{\delta} dl\ \sigma_j(E)\,\phi_j\left(\vec{x} + l\vec{\Omega}, \vec{\Omega}, E\right) \end{aligned} \tag{2.1}$$

where $\sigma_j(E)$ and $\sigma_{jk}\left(\vec{\Omega}, \vec{\Omega}', E, E'\right)$ are the media macroscopic cross sections. The cross section $\sigma_{jk}\left(\vec{\Omega}, \vec{\Omega}', E, E'\right)$ represents all those processes by which type k particles moving in direction $\vec{\Omega}'$ with energy E' produce a type j particle in direction $\vec{\Omega}$ with energy E. Note that there may be several reactions that could produce this result, and the appropriate cross sections of equation (2.1) are the inclusive ones. The second term on the right side of equation (2.1) is the source of secondary particles integrated over the total volume $2\delta\left(\delta^2\, d\vec{\Omega}\right)$, and the third term is the loss through nuclear reaction integrated over the same volume. The expansion of the terms of each side and retention of the terms to order δ^3 explicitly result in

$$\delta^2\, d\vec{\Omega}\left[\phi_j\left(\vec{x},\vec{\Omega},E\right)+\delta\vec{\Omega}\cdot\nabla\phi_j\left(\vec{x},\vec{\Omega},E\right)\right] = \delta^2\, d\vec{\Omega}\left[\phi_j\left(\vec{x},\vec{\Omega},E\right)-\delta\vec{\Omega}\cdot\nabla\phi_j\left(\vec{x},\vec{\Omega},E\right)\right.$$
$$+2\delta\sum_k\int\sigma_{jk}\left(\vec{\Omega},\vec{\Omega}',E,E'\right)\phi_k\left(\vec{x},\vec{\Omega}',E'\right)d\vec{\Omega}'\,dE'$$
$$\left.-2\delta\sigma_j(E)\,\phi_j\left(\vec{x},\vec{\Omega},E\right)\right]+O\left(\delta^4\right) \tag{2.2}$$

which can be divided by the cylindrical volume $2\delta\left(\delta^2\, d\vec{\Omega}\right)$ and written as

$$\vec{\Omega}\cdot\nabla\phi_j\left(\vec{x},\vec{\Omega},E\right)=\sum_k\int\sigma_{jk}\left(\vec{\Omega},\vec{\Omega}',E,E'\right)\phi_k\left(\vec{x},\vec{\Omega}',E'\right)d\vec{\Omega}'\,dE'-\sigma_j(E)\,\phi_j\left(\vec{x},\vec{\Omega},E\right)+O(\delta) \tag{2.3}$$

for which the last term $O(\delta)$ approaches zero in the limit as $\delta\to 0$. Equation (2.3) is recognized as the time-independent form of the Boltzmann equation for a dual-species tenuous gas. Atomic collisions preserve the identity of the particle, and both terms on the right side of equation (2.3) contribute. The differential cross sections for the atomic processes have the approximate form

$$\sigma_{jk}^{\mathrm{at}}\left(\vec{\Omega},\vec{\Omega}',E,E'\right)=\sum_n\sigma_{jn}^{\mathrm{at}}(E')\,\delta\left(\vec{\Omega}\cdot\vec{\Omega}'-1\right)\delta_{jk}\delta\left(E+\varepsilon_n-E'\right) \tag{2.4}$$

where n labels the electronic excitation levels and ε_n represents the corresponding excitation energies, which are small (1 to 100 eV) compared with the particle energy E. The atomic terms can then be written as

$$\sum_k\int\sigma_{jk}^{\mathrm{at}}\left(\vec{\Omega},\vec{\Omega}',E,E'\right)\phi_k\left(\vec{x},\vec{\Omega}',E'\right)d\vec{\Omega}'\,dE'-\sigma_j^{\mathrm{at}}(E)\,\phi_j\left(\vec{x},\vec{\Omega},E\right)$$
$$=\sum_n\sigma_{jn}^{\mathrm{at}}(E+\varepsilon_n)\,\phi_j\left(\vec{x},\vec{\Omega},E+\varepsilon_n\right)-\sigma_j^{\mathrm{at}}(E)\,\phi_j\left(\vec{x},\vec{\Omega},E\right)$$
$$\approx\sum_n\sigma_j^{\mathrm{at}}(E)\,\phi_j\left(\vec{x},\vec{\Omega},E\right)+\sum_n\varepsilon_n\frac{\partial}{\partial E}\left[\sigma_{jn}^{\mathrm{at}}(E)\,\phi_j\left(\vec{x},\vec{\Omega},E\right)\right]-\sigma_j^{\mathrm{at}}(E)\,\phi_j\left(\vec{x},\vec{\Omega},E\right)$$
$$=\frac{\partial}{\partial E}\left[S_j(E)\,\phi_j\left(\vec{x},\vec{\Omega},E\right)\right] \tag{2.5}$$

because the stopping power is

$$S_j(E)=\sum_n\sigma_{jn}^{\mathrm{at}}(E)\,\varepsilon_n \tag{2.6}$$

and the atomic cross section is

$$\sigma_j^{\mathrm{at}}(E)=\sum_n\sigma_{jn}^{\mathrm{at}}(E) \tag{2.7}$$

Equations (2.5)–(2.7) permit the rewriting of equation (2.3) in the usual continuous slowing-down approximation as

$$\vec{\Omega}\cdot\nabla\phi_j\left(\vec{x},\vec{\Omega},E\right)-\frac{\partial}{\partial E}\left[S_j(E)\,\phi_j\left(\vec{x},\vec{\Omega},E\right)\right]+\sigma_j(E)\,\phi_j\left(\vec{x},\vec{\Omega},E\right)$$
$$=\int\sum_k\sigma_{jk}\left(\vec{\Omega},\vec{\Omega}',E,E'\right)\phi_k\left(\vec{x},\vec{\Omega}',E'\right)d\vec{\Omega}'\,dE' \tag{2.8}$$

where the cross section of equation (2.8) now contains only the nuclear contributions.

3. Transport Formalism

The Boltzmann equation (2.8), as derived in section 2, can be rewritten as

$$\left[\vec{\Omega}\cdot\nabla-\frac{1}{A_j}\frac{\partial}{\partial E}S_j(E)+\sigma_j(E)\right]\phi_j\left(\vec{x},\vec{\Omega},E\right)=\sum_k\int dE'\,d\vec{\Omega}'\,\sigma_{jk}\left(E,E',\vec{\Omega},\vec{\Omega}'\right)\phi_k\left(\vec{x},\vec{\Omega}',E'\right) \quad (3.1)$$

where $\phi_j\left(\vec{x},\vec{\Omega},E\right)$ is the flux of ions of type j with atomic mass A_j at $\vec{x}$ with motion along $\vec{\Omega}$ and energy E in units of A MeV, $\sigma_j(E)$ is the corresponding macroscopic cross section, $S_j(E)$ is the linear energy transfer (LET), and $\sigma_{jk}\left(E,E',\vec{\Omega},\vec{\Omega}'\right)$ is the production cross section for type j particles with energy E and direction $\vec{\Omega}$ by collision of a type k particle of energy E' and direction $\vec{\Omega}'$. The term that contains $S_j(E)$ on the left side of equation (3.1) is the result of the continuous slowing-down approximation. The solutions of equation (3.1) are unique in any convex region for which the inbound flux of each particle type is specified everywhere on the boundary surface. If the boundary is given as the loci of a two-parameter vector function $\gamma(s,t)$ for which a generic point on the boundary is given by $\vec{\Gamma}$, then the boundary condition is specified by requiring the solution of equation (3.1) to meet

$$\phi_j\left(\vec{\Gamma},\vec{\Omega},E\right)=\psi_j\left(\vec{\Gamma},\vec{\Omega},E\right) \quad (3.2)$$

for each value of $\vec{\Omega}$ such that

$$\vec{\Omega}\cdot\vec{n}\left(\vec{\Gamma}\right)<0 \quad (3.3)$$

where $\vec{n}\left(\vec{\Gamma}\right)$ is the outwardly directed unit normal vector at the boundary surface at point $\vec{\Gamma}$, and ψ_j is the specified boundary condition.

The fragmentation of the projectile and target nuclei is represented by the quantity $\sigma_{jk}\left(E,E',\vec{\Omega},\vec{\Omega}'\right)$, which is composed of three functions

$$\sigma_{jk}\left(E,E',\vec{\Omega},\vec{\Omega}'\right)=\sigma_k(E')\,m_{jk}(E')\,f_{jk}\left(E,E',\vec{\Omega},\vec{\Omega}'\right) \quad (3.4)$$

where $m_{jk}(E')$ is the multiplicity (i.e., average number) of type j particles being produced by a collision of type k of energy E', and $f_{jk}\left(E,E',\vec{\Omega},\vec{\Omega}'\right)$ is the probability density distribution for producing particles of type j of energy E in the direction $\vec{\Omega}$ from the collision of a type k particle with energy E' moving in the direction $\vec{\Omega}'$. For an unpolarized source of projectiles and targets, the energy angle distribution of reaction products can be a function of energies and cosine of the production angle relative to the incident projectile direction. The secondary multiplicities $m_{jk}(E)$ and secondary energy angle distributions are the major unknowns in ion transport theory.

Information on the multiplicity $m_{jk}(E)$ was obtained in the past through experiments with galactic cosmic rays (GCR) as an ion source, and the fragmentation of the ions on target nuclei was observed in nuclear emulsion. (See ref. 23.) Such data are mainly limited by not knowing precisely the identity of the initial or secondary ions and by relatively low-counting rates of each ion type. The heavy ion acceleration by machine reduces the uncertainty because high-counting rates can be obtained with known ion

types. In addition, accelerator experiments provide information, which was not previously available, for the spectral distribution $f_{jk}\left(E, E', \vec{\Omega}, \vec{\Omega}'\right)$. (See ref. 24.)

The spectral distribution function consists of two terms that describe the fragmentation of the projectile and the fragmentation of the struck nucleus as follows (refs. 25 and 26):

$$\sigma_{jk}\left(E, E', \vec{\Omega}, \vec{\Omega}'\right) = \sigma_k(E')\left[\nu_{jk}^P(E') f_{jk}^P\left(E, E', \vec{\Omega}, \vec{\Omega}'\right) + \nu_{jk}^T(E') f_{jk}^T\left(E, E', \vec{\Omega}, \vec{\Omega}'\right)\right] \tag{3.5}$$

where ν_{jk}^P and f_{jk}^P depend only weakly on the target and ν_{jk}^T and f_{jk}^T depend only weakly on the projectile. Although the average secondary velocities associated with f^P are nearly equal to the projectile velocity, the average velocities associated with f^T are near zero. Experimentally,

$$\begin{aligned} f_{jk}^P\left(E, E', \vec{\Omega}, \vec{\Omega}'\right) &\approx \left[\frac{m}{2\pi\left(\sigma_{jk}^P\right)^2}\right]^{3/2} \sqrt{2E}\, \exp\left[-\frac{(\vec{p} - \vec{p}')^2}{2\left(\sigma_{jk}^P\right)^2}\right] \\ &\approx \left[\frac{m}{2\pi\left(\sigma_{jk}^P\right)^2}\right]^{3/2} \sqrt{2E}\, \exp\left[-\frac{\left(\vec{\Omega}\sqrt{2mE} - \vec{\Omega}'\sqrt{2mE'}\right)^2}{2\left(\sigma_{jk}^P\right)^2}\right] \end{aligned} \tag{3.6}$$

where $\vec{p}$ and $\vec{p}'$ are the momenta per unit mass of j and k ions, respectively, and

$$f_{jk}^T\left(E, E', \vec{\Omega}, \vec{\Omega}'\right) \approx \left[\frac{m}{2\pi\left(\sigma_{jk}^T\right)^2}\right]^{3/2} \sqrt{2E}\, \exp\left[-\frac{\vec{p}^2}{2\left(\sigma_{jk}^T\right)^2}\right] \tag{3.7}$$

where σ_{jk}^P and σ_{jk}^T are related to the rms momentum spread of secondary products. These parameters depend only on the fragmenting nucleus. Feshbach and Huang (ref. 27) suggested that the parameters σ_{jk}^P and σ_{jk}^T depend on the average square momentum of the nuclear fragments as described by Fermi motion. A precise formulation of these ideas in terms of a statistical model was obtained by Goldhaber. (See ref. 28.)

4. Approximation Procedures

4.1. Neglect of Target Fragmentation

The use of equations (3.5)–(3.7) in the evaluation of the source term $\zeta_j\left(\vec{x}, \vec{\Omega}, E\right)$ of equation (3.1) results in

$$\begin{aligned} \zeta_j\left(\vec{x}, \vec{\Omega}, E\right) &= \sum_k \int dE'\, d\vec{\Omega}'\, \sigma_k(E')\, \phi_k\left(\vec{x}, \vec{\Omega}', E'\right)\left[\nu_{jk}^P(E') f_{jk}^P\left(E, E', \vec{\Omega}, \vec{\Omega}'\right) + \nu_{jk}^T f_{jk}^T\left(E, E', \vec{\Omega}, \vec{\Omega}'\right)\right] \\ &\equiv \zeta_j^P\left(\vec{x}, \vec{\Omega}, E\right) + \zeta_j^T\left(\vec{x}, \vec{\Omega}, E\right) \end{aligned} \tag{4.1}$$

where as before, the superscripts P and T refer to the fragmentation of the projectile and the target, respectively. The target term is

$$\zeta_j^T\left(\vec{x}, \vec{\Omega}, E\right) = \sum_k \left[\frac{m}{2\pi\left(\sigma_{jk}^T\right)^2}\right]^{3/2} \sqrt{2\mathrm{E}}\, \exp\left[-\frac{mE}{\left(\sigma_{jk}^T\right)^2}\right] \int d\vec{\Omega}' \int_E^\infty dE'\, \nu_{jk}^T(E')\, \sigma_k(E')\, \phi_k\left(\vec{x}, \vec{\Omega}', E'\right) \tag{4.2}$$

which is negligibly small for

$$E \gg \frac{\left(\sigma_{jk}^{T}\right)^2}{m} \tag{4.3}$$

Thus, for calculating the flux at high energy,

$$\zeta_j\left(\vec{x}, \vec{\Omega}, E\right) \approx \zeta_j^P\left(\vec{x}, \vec{\Omega}, E\right) \tag{4.4}$$

4.2. Space Radiations

Space radiations have the convenient property of being nearly isotropic. This fact, coupled with the forward-peaked spectral distribution, leads to a substantial simplification in the source term as follows:

$$\zeta_j^P\left(\vec{x}, \vec{\Omega}, E\right) \approx \sum_k \int dE'\, d\vec{\Omega}'\, \sigma_k(E')\, \nu_{jk}^P(E') \left[\frac{m}{2\pi\left(\sigma_{jk}^P\right)^2}\right]^{3/2} \sqrt{2E'}\, \exp\left[-\frac{\left(\vec{\Omega}\sqrt{2mE} - \vec{\Omega}\sqrt{2mE'}\right)^2}{2\left(\sigma_{jk}^P\right)^2}\right] \phi_k\left(\vec{x}, \vec{\Omega}', E'\right) \tag{4.5}$$

If $\phi_k\left(\vec{x}, \vec{\Omega}', E'\right)$ is assumed to be a slowly varying function of $\vec{\Omega}'$, an expansion about the sharply peaked maximum of the exponential function is possible. Such an expansion is made by letting

$$\vec{\Omega}' = \vec{\Omega} + (\cos\theta - 1)\,\vec{\Omega} + \vec{e}_\phi \sin\theta \tag{4.6}$$

where

$$\cos\theta = \vec{\Omega} \cdot \vec{\Omega}' \tag{4.7}$$

and

$$\vec{e}_\phi = \frac{\vec{\Omega} \times \vec{\Omega}'}{\left|\vec{\Omega} \times \vec{\Omega}'\right|} \tag{4.8}$$

The flux may be expanded as

$$\phi_k\left(\vec{x}, \vec{\Omega}', E'\right) = \phi_k\left(\vec{x}, \vec{\Omega}, E'\right) + \left[\frac{\partial}{\partial\vec{\Omega}}\, \phi_k\left(\vec{x}, \vec{\Omega}, E'\right)\right] \cdot \left[(\cos\theta - 1)\,\vec{\Omega} + \vec{e}_\phi \sin\theta\right] + \ldots \tag{4.9}$$

Substitution of equation (4.9) into equation (4.5) and simplification result in

$$\zeta_j^P\left(\vec{x}, \vec{\Omega}, E\right) \approx \sum_k \int dE'\, \sigma_k(E')\, \nu_{jk}^P(E') \left[\frac{m}{2\pi\left(\sigma_{jk}^P\right)^2}\right]^{3/2} \frac{\sqrt{2}}{\sqrt{E'}}\, \exp\left[-\frac{\left(\sqrt{2mE} - \sqrt{2mE'}\right)^2}{2\left(\sigma_{jk}^P\right)^2}\right]$$

$$\times \left\{\phi_k\left(\vec{x}, \vec{\Omega}, E'\right) - \left[\vec{\Omega} \cdot \frac{\partial}{\partial\vec{\Omega}}\, \phi_k\left(\vec{x}, \vec{\Omega}, E'\right)\right] \left[\frac{\left(\sigma_{jk}^P\right)^2}{2m\sqrt{EE'}}\right] + \ldots\right\} \tag{4.10}$$

The leading term of equation (4.10) is clearly a good approximation of the source term whenever

$$\frac{2mE}{\left(\sigma_{jk}^{P}\right)^{2}} \gg \frac{\vec{\Omega} \cdot \frac{\partial}{\partial \vec{\Omega}} \phi_k\left(\vec{x}, \vec{\Omega}, E'\right)}{\phi_k\left(\vec{x}, \vec{\Omega}, E'\right)} \tag{4.11}$$

The leading term is equivalent to assuming that secondary ions are produced only in the direction of motion of the primary ions. For space radiations, which are nearly isotropic, equation (4.11) is easily met, and neglection of higher order terms in equation (4.10) results in the usual straight-ahead approximation. If radiations are highly anisotropic, then equation (4.11) is not likely to apply. Validity of straight-ahead approximation was studied empirically by Alsmiller et al. (refs. 29 and 30) for proton transport.

4.3. Velocity-Conserving Interactions

Customarily, in cosmic ion transport studies (ref. 31), fragment velocities are assumed to be equal to the fragmenting ion velocity before collision. The order of approximation resulting from such an assumption is derived with the assumption that the projectile energy E' is equal to the secondary energy plus a positive quantity ε,

$$E' = E + \varepsilon \tag{4.12}$$

where ε is assumed to contribute to equation (4.10) only across a small range above zero energy. Substitution of equation (4.12) into equation (4.10) and expansion of the integrand result in

$$\begin{aligned}\zeta_j^P\left(\vec{x}, \vec{\Omega}, E\right) = \sum_k \sigma_k(E)\, \nu_{jk}^P(E) \Bigg\{ & \phi_k\left(\vec{x}, \vec{\Omega}, E\right)\left[1 - \sqrt{\frac{\left(\sigma_{jk}^P\right)^2}{\pi m E}}\right] \\ & + \left[E \frac{\partial}{\partial E} \phi_k\left(\vec{x}, \vec{\Omega}, E\right)\right]\sqrt{\frac{\left(\sigma_{jk}^P\right)^2}{\pi m E}} - \left[\vec{\Omega} \cdot \frac{\partial}{\partial \vec{\Omega}} \phi_k\left(\vec{x}, \vec{\Omega}, E\right)\right]\frac{\left(\sigma_{jk}^P\right)^2}{2mE} + \ldots \Bigg\}\end{aligned} \tag{4.13}$$

Because $\sqrt{\left(\sigma_{jk}^P\right)^2 / mE} \ll 1$, the assumption of velocity conservation at those energies for which most nuclear reactions occur is inferior to the straight-ahead approximation but may be adequate for space radiations where variation of $\phi_k\left(\vec{x}, \vec{\Omega}, E\right)$ with energy is sufficiently smooth. That is

$$E \frac{\partial}{\partial E} \phi_k\left(\vec{x}, \vec{\Omega}, E\right) \approx \phi_k\left(\vec{x}, \vec{\Omega}, E\right)$$

4.4. Decoupling Target and Projectile Flux

Equation (3.1) can be rewritten with equation (4.1) as

$$B_j \phi_j\left(\vec{x}, \vec{\Omega}, E\right) = \sum_k F_{jk}^T \phi_k\left(\vec{x}, \vec{\Omega}, E\right) + \sum_k F_{jk}^P \phi_k\left(\vec{x}, \vec{\Omega}, E\right) \tag{4.14}$$

where the differential operator is given by

$$B_j = \left[\vec{\Omega} \cdot \nabla - \frac{1}{A_j} \frac{\partial}{\partial E} S_j(E) + \sigma_j(E)\right] \tag{4.15}$$

and the integral operator $F_{jk} = F_{jk}^T + F_{jk}^P$ is given by

$$F_{jk}\phi_k\left(\vec{x}, \vec{\Omega}, E\right) = \int dE' \, d\vec{\Omega}' \, \sigma_{jk}\left(E, E', \vec{\Omega}, \vec{\Omega}'\right)\phi_k\left(\vec{x}, \vec{\Omega}', E'\right) \tag{4.16}$$

By defining the flux as the sum of two terms,

$$\phi_j\left(\vec{x}, \vec{\Omega}, E\right) = \phi_j^T\left(\vec{x}, \vec{\Omega}, E\right) + \phi_j^P\left(\vec{x}, \vec{\Omega}, E\right) \tag{4.17}$$

which permits the following separation:

$$B_j\phi_j^P\left(\vec{x}, \vec{\Omega}, E\right) = \sum_k F_{jk}^P\phi_k^P\left(\vec{x}, \vec{\Omega}, E\right) + \sum_k F_{jk}^P\phi_k^T\left(\vec{x}, \vec{\Omega}, E\right) \tag{4.18}$$

$$B_j\phi_j^T\left(\vec{x}, \vec{\Omega}, E\right) = \sum_k F_{jk}^T\phi_k^P\left(\vec{x}, \vec{\Omega}, E\right) + \sum_k F_{jk}^T\phi_k^T\left(\vec{x}, \vec{\Omega}, E\right) \tag{4.19}$$

As noted in connection with equations (4.1)–(4.4), the source term on the right side of equation (4.19) is small at high energies. Assume that

$$\phi_j^T\left(\vec{x}, \vec{\Omega}, E\right) \approx 0 \tag{4.20}$$

for $E \gg \left(\sigma_{jk}^T\right)^2/m$. As a result of equation (4.20) and the fact that the ion range is small compared with its mean free path at low energy,

$$B_j\phi_j^P\left(\vec{x}, \vec{\Omega}, E\right) \approx \sum_k F_{jk}^P\phi_k^P\left(\vec{x}, \vec{\Omega}, E\right) \tag{4.21}$$

$$B_j\phi_j^T\left(\vec{x}, \vec{\Omega}, E\right) \approx \sum_k F_{jk}^T\phi_k^P\left(\vec{x}, \vec{\Omega}, E\right) \tag{4.22}$$

The advantage of this separation is that, once equation (4.21) is solved, equation (4.22) can be solved in closed form. The solution of equation (4.22) is accomplished by noting that the inwardly directed flux ϕ_j^T must vanish on the boundary so that

$$\phi_j^T\left(\vec{x}, \vec{\Omega}, E\right) \approx \sum_k \int_E^{E_\gamma} dE' \, \frac{A_j P_j(E')}{P_j(E)\, S_j(E)} \int dE'' \, d\vec{\Omega} \, \sigma_{jk}^T\left(E', E'', \vec{\Omega}, \vec{\Omega}'\right)$$
$$\times \phi_k^P\left\{\vec{x} + \left[R_j(E) - R_j(E')\right]\vec{\Omega}, \vec{\Omega}', E''\right\} \tag{4.23}$$

where $E_\gamma = R_j^{-1}\left[d + R_j(E)\right]$ with d being the projected distance to the boundary.

The use of equations (3.5) and (3.7) in equation (4.23) yields

$$\phi_j^T\left(\vec{x}, \vec{\Omega}, E\right) \approx \int_E^{E_\gamma} dE' \, \frac{A_j P_j(E')}{P_j(E)\, S_j(E)} \left[\frac{m}{2\pi\left(\sigma_{jk}^T\right)^2}\right]^{3/2} \sqrt{2E'} \, \exp\left[-\frac{mE'}{\left(\sigma_{jk}^T\right)^2}\right]$$
$$\times \zeta_j^T\left\{\vec{x} + \left[R_j(E) - R_j(E')\right]\vec{\Omega}\right\} \tag{4.24}$$

where

$$\zeta_j^T(\vec{x}) = \sum_k \int dE' \, d\vec{\Omega}' \, \sigma_k(E') \, \nu_{jk}^T(E') \, \phi_k^P\left(\vec{x}, \vec{\Omega}', E'\right) \tag{4.25}$$

and σ_{jk}^{T} has been assumed to be a slowly varying function of projectile type k and projectile energy E. If the range of secondary type j ions is small compared with their mean-free-path lengths and the mean free paths of the fragmenting parent ions l_k, then

$$R_j\left[\frac{\left(\sigma_{jk}^{T}\right)^2}{m}\right] \ll l_k \tag{4.26}$$

and the integral of equation (4.24) may be simplified as

$$\phi_j^T\left(\vec{x}, \vec{\Omega}, E\right) \approx \frac{A_j}{S_j(E)}\zeta_j^T(\vec{x})\int_E^{E_\gamma}\left[\frac{m}{2\pi\left(\sigma_{jk}^{T}\right)^2}\right]^{3/2}\sqrt{2E'}\,\exp\left[-\frac{mE'}{\left(\sigma_{jk}^{T}\right)^2}\right]dE' \tag{4.27}$$

which can be reduced into terms of known functions. Thus,

$$\phi_j^T\left(\vec{x}, \vec{\Omega}, E\right) \approx \frac{A_j}{S_j(E)}\zeta_j^T(\vec{x})\,\frac{1}{2\pi\sqrt{\pi}}\left\{\vec{\Gamma}\left[\frac{3}{2}\,\frac{mE}{\left(\sigma_{jk}^{T}\right)^2}\right] - \vec{\Gamma}\left[\frac{3}{2}\,\frac{mE_\gamma}{\left(\sigma_{jk}^{T}\right)^2}\right]\right\} \tag{4.28}$$

in terms of the incomplete gamma function. Equation (4.28) can be shown to be equivalent to

$$\begin{aligned}\phi_j^T\left(\vec{x}, \vec{\Omega}, E\right) \approx \frac{A_j}{S_j(E)}\zeta_j^T(\vec{x})\,\frac{1}{2\pi}\Bigg\{&\frac{1}{2}\mathrm{erfc}\left[\sqrt{\frac{mE}{\left(\sigma_{jk}^{T}\right)^2}}\right] - \frac{1}{2}\mathrm{erfc}\left[\sqrt{\frac{mE_\gamma}{\left(\sigma_{jk}^{T}\right)^2}}\right]\\ &+ \sqrt{\frac{mE}{\pi\left(\sigma_{jk}^{T}\right)^2}}\,\exp\left[-\frac{mE}{\left(\sigma_{jk}^{T}\right)^2}\right] - \sqrt{\frac{mE_\gamma}{\pi\left(\sigma_{jk}^{T}\right)^2}}\,\exp\left[-\frac{mE\sigma}{\left(\sigma_{jk}^{T}\right)^2}\right]\Bigg\}\end{aligned} \tag{4.29}$$

At points sufficiently far from the boundary such that

$$R_j^{-1}(d) \gg \frac{\left(\sigma_{jk}^{T}\right)^2}{m} \tag{4.30}$$

equation (4.28) may be reduced to

$$\phi_j^T\left(\vec{x}, \vec{\Omega}, E\right) \approx \frac{A_j}{S_j(E)}\zeta_j^T(\vec{x})\,\frac{1}{2\pi}\left\{\frac{1}{2}\mathrm{erfc}\left[\sqrt{\frac{mE}{\left(\sigma_{jk}^{T}\right)^2}}\right] + \sqrt{\frac{mE}{\pi\left(\sigma_{jk}^{T}\right)^2}}\,\exp\left[-\frac{mE}{\left(\sigma_{jk}^{T}\right)^2}\right]\right\} \tag{4.31}$$

which is the equilibrium solution because the target fragment spectrum is the difference between the collision source and collision losses. The solution of equation (4.21) is examined in section 4.5.

4.5. Back Substitution and Perturbation Theory

One approach to the solution of equation (4.21) results from the fact that the multiple charged ions tend to be destroyed in nuclear reactions. Thus,

$$F_{jk}^{P} \equiv 0 \qquad (j \geq k) \tag{4.32}$$

This means that there is a maximum j such that

$$B_J\phi_J^P\left(\vec{x}, \vec{\Omega}, E\right) = 0 \tag{4.33}$$

where J is the maximum j. Furthermore,

$$B_{J-1}\phi^P_{J-1}\left(\vec{x}, \vec{\Omega}, E\right) = F^P_{J-1,\,J}\phi^P_J\left(\vec{x}, \vec{\Omega}, E\right) \tag{4.34}$$

and in general,

$$B_{J-N}\phi^P_{J-N}\left(\vec{x}, \vec{\Omega}, E\right) = \sum_{k=1}^{N-1} F^P_{J-N,\,J-k}\phi^P_{J-k}\left(\vec{x}, \vec{\Omega}, E\right) \qquad (N < J-1) \tag{4.35}$$

Note that equations (4.34) and (4.35) constitute solvable problems. The singly and doubly charged ions satisfy

$$B_1\phi^P_1\left(\vec{x}, \vec{\Omega}, E\right) = F^P_{1,\,1}\phi^P_1\left(\vec{x}, \vec{\Omega}, E\right) + \sum_{k=2}^{J} F^P_{1,\,k}\phi^P_k\left(\vec{x}, \vec{\Omega}, E\right) \tag{4.36}$$

Equation (4.36), unlike equations (4.33)–(4.35), is an integral-differential equation that is difficult to solve directly. Equation (4.35) is solvable by perturbation theory, and the resultant series is known to converge rapidly for intermediate and low energies. (See refs. 10 and 32–34.) Note that equations (4.33) and (4.35) are also obtained from perturbation theory as applied to equation (4.21) at the outset. Thus, the perturbation series is expected to converge after the first J plus a few terms.

5. Galactic Ion Transport

5.1. Derivation of GCR Heavy Ion Transport Equation

In this section, the methods of previous nucleon transport studies (ref. 32) are expanded by combining analytical and numerical tools. The galactic cosmic ray ion transport problem is transformed to an integral along the characteristic curve of that particular ion, and the perturbation series (ref. 32) is replaced by a simple numerical procedure. The resulting method reduces the difficulty associated with the low-energy discretization and the restriction to a definite form for the stopping power. The resulting numerical procedure is simple and is not computationally intensive.

Here, the straight-ahead approximation is used, and the target secondary fragments are neglected. (See refs. 6 and 8.) For multiple charged ions, the transport equation can be written as

$$\left[\frac{\partial}{\partial x} - \frac{\partial}{\partial E}\,\tilde{S}_j(E) + \sigma_j\right]\phi_j(x, E) = \sum_{k>j} m_{jk}\sigma_k\phi_k(x, E) \tag{5.1}$$

where $\phi_j(x, E)$ is the flux of ions of type j with atomic mass A_j at x moving along the X-axis at energy E in units of A MeV, σ_j is the corresponding macroscopic nuclear absorption cross section, $\tilde{S}_j(E)$ is the change in E per unit distance, and m_{jk} is the multiplicity of ion j produced by ion k in a collision. The corresponding transport equation for the light ions is

$$\left[\frac{\partial}{\partial x} - \frac{\partial}{\partial E}\,\tilde{S}_j(E) + \sigma_j(E)\right]\phi_j(x, E) = \sum_k \int_E^\infty \sigma_{jk}(E, E')\,\phi_k(x, E')\,dE' \tag{5.2}$$

The quantities m_{jk} and σ_j are assumed to be energy independent in equation (5.1) but are fully energy dependent in equation (5.2).

The range of the ion is given as

$$R_j(E) = \int_0^E \frac{dE'}{\tilde{S}_j(E')} \tag{5.3}$$

The solution to equation (5.1) is found subject to the boundary specification at $x = 0$ and arbitrary E as

$$\phi_j(0, E) = F_j(E) \tag{5.4}$$

Usually, $F_j(E)$ is called the incident beam spectrum.

From Bethe's theory,

$$\tilde{S}_j(E) = \frac{A_p Z_j^2}{A_j Z_p^2} \tilde{S}_p(E) \tag{5.5}$$

which holds for all energies greater than $\approx 100A$ keV, provided that the ion effective charge is used, and leads to

$$\frac{Z_j^2}{A_j} R_j(E) = \frac{Z_p^2}{A_p} R_p(E) \tag{5.6}$$

The subscript p refers to proton. Equation (5.6) is accurate at high energy and only approximately true at low energy because of electron capture by the ion (which effectively reduces its charge), higher order Born corrections to Bethe's theory, and nuclear stopping at the lowest energies. Herein, the parameter ν_j is defined as

$$\nu_j R_j(E) = \nu_k R_k(E) \tag{5.7}$$

so that

$$\nu_j = \frac{Z_j^2}{A_j} \tag{5.8}$$

Equations (5.6)–(5.8) are used in the subsequent development, and the energy variation in ν_j is neglected. The inverse function of $R_j(E)$ is defined as

$$E = R_j^{-1}[R_j(E)] \tag{5.9}$$

For the purpose of solving equation (5.1), the following coordinates are used:

$$\eta_j \equiv x - R_j(E) \tag{5.10}$$

$$\xi_j \equiv x + R_j(E) \tag{5.11}$$

where η_j varies along the particle path, and ξ_j is constant along the particle trajectory. The new fluence functions are defined as

$$\chi_j(\eta_j, \xi_j) \equiv \tilde{S}_j(E)\, \phi_j(x, E) = \psi_j(x, r_j) \tag{5.12}$$

$$\bar{\chi}_k(\eta_j, \xi_j) \equiv \chi_k(\eta_k, \xi_k) \tag{5.13}$$

where

$$\xi_j + \eta_j = \xi_k + \eta_k \tag{5.14}$$

$$\eta_j - \xi_j = \frac{\nu_k}{\nu_j}(\eta_k - \xi_k) \tag{5.15}$$

and $r_j = R_j(E)$. By this coordinate mapping, equation (5.1) becomes

$$\left(2\frac{\partial}{\partial\eta_j}+\sigma_j\right)\chi_j(\eta_j,\xi_j) = \sum_k m_{jk}\sigma_k\frac{\nu_j}{\nu_k}\bar{\chi}_k(\eta_j,\xi_j) \tag{5.16}$$

where σ_j is assumed to be energy independent for simplicity of formalism. There is a small variation in σ_j (≈20 percent) that is accounted for in the code. (See ref. 35.) Equation (5.16) is solved by using line integration with an integrating factor (ref. 12), which results in

$$\mu_j(\eta_j,\xi_j) = \exp\left[\frac{1}{2}\sigma_j(\xi_j+\eta_j)\right] \tag{5.17}$$

Then,

$$\begin{aligned}\chi_j(\eta_j,\xi_j) &= \exp\left[-\frac{1}{2}\sigma_j(\xi_j+\eta_j)\right]\chi_j(-\xi_j,\xi_j)\\ &\quad+\frac{1}{2}\int_{-\xi_j}^{\eta_j}\exp\left[\frac{1}{2}\sigma_j\left(\eta'-\eta_j\right)\right]\sum_k m_{jk}\sigma_k\frac{\nu_j}{\nu_k}\chi_k\left(\eta_k',\xi_k'\right)d\eta'\end{aligned} \tag{5.18}$$

where

$$\eta_k' = \frac{\nu_k+\nu_j}{2\nu_k}\eta' + \frac{\nu_k-\nu_j}{2\nu_k}\xi_j$$

$$\xi_k' = \frac{\nu_k-\nu_j}{2\nu_k}\eta' + \frac{\nu_k+\nu_j}{2\nu_k}\xi_j$$

By defining

$$\psi_j(x,r_j) = \chi_j(\eta_j,\xi_j) \tag{5.19}$$

then

$$\psi_j(x,r_j) = \exp(-\sigma_j x)\,\psi_j(0,r_j+x) + \int_0^x dz\exp(-\sigma_j z)\sum_k m_{jk}\sigma_k\frac{\nu_j}{\nu_k}\psi_k\left(x-z,\,r_k+\frac{\nu_j}{\nu_k}z\right) \tag{5.20}$$

Furthermore,

$$\begin{aligned}\psi_j(x+h,r_j) &= \exp(-\sigma_j h)\,\psi_j(x,r_j+h)\\ &\quad+\int_0^h dz\exp(-\sigma_j z)\sum_k m_{jk}\sigma_k\frac{\nu_j}{\nu_k}\psi_k\left(x+h-z,\,r_k+\frac{\nu_j}{\nu_k}z\right)\end{aligned} \tag{5.21}$$

Equation (5.20) clearly shows that

$$\psi_k(x+h-z,r_k) = \exp[-\sigma_k(h-z)]\,\psi_k(x,r_k+h) + O(h-z) \tag{5.22}$$

which, after substitution into equation (5.21), yields

$$\begin{aligned}\psi_j(x+h,r_j) &= \exp(-\sigma_j h)\,\psi_j(x,r_j+h)\\ &\quad+\int_0^h dz\exp(-\sigma_j z)\sum_k m_{jk}\sigma_k\frac{\nu_j}{\nu_k}\exp[-\sigma_k(h-z)]\,\psi_k\left(x,\,r_k+\frac{\nu_j}{\nu_k}z+h-z\right)\end{aligned} \tag{5.23}$$

which is correct to order h^2. This expression can be further approximated by

$$\psi_j(x+h, r_j) = \exp(-\sigma_j h)\,\psi_j(x, r_j+h) + \sum_k m_{jk}\sigma_k \frac{\nu_j}{\nu_k}\left[\frac{\exp(-\sigma_j h) - \exp(-\sigma_k h)}{\sigma_k - \sigma_j}\right]\psi_k\left(x, r_k + \frac{\nu_j}{\nu_k}h\right) \tag{5.24}$$

which is accurate to $O[(\nu_k - \nu_j)h]$. Equation (5.24) is the basis of the GCR transport computer code GCRTRN. (See refs. 12, 13, and 36.) The nucleon transport equation (5.2) is solved by adding the heavy ion collision source of nucleons to the BRYNTRN computer code (ref. 33) to create HZETRN, which effectively solves equation (5.2) by adding a heavy ion collision source of nucleons to the right side of the equation. Equation (5.24) provides the propagation algorithm for the heavy ions. The corresponding propagation procedure for the light ions (refs. 33, 37, and 38) is

$$\psi(x+h, r) \approx e^{-\sigma h}\psi(x, r+h) + e^{-\sigma h}\int_0^h dz \int_r^\infty dr' f(r+z, r'+z)\,\psi(x, r'+h) \tag{5.25}$$

with the order of h^2.

The following quantities are of interest:

1. The integral fluence is

$$\phi_j(x, >E) = \int_{R_j(E)}^\infty \psi_j(x, r)\,dr \tag{5.26}$$

2. The energy absorbed per gram is

$$D_j(x, >E) = \int_E^\infty A_j \psi_j[x, R_j(E)]\,dE \tag{5.27}$$

3. The dose equivalent is

$$H_j(x, >E) = A_j \int_E^\infty Q_F \psi_j[x, R_j(E)]\,dE \tag{5.28}$$

where Q_F is the quality factor. These quantities are not recommended for use in shield design for protection from GCR but give some relative measure of their biological importance.

5.2. Numerical Procedure

The secondary particle production term of the propagation algorithm for the nucleons in equation (5.25) has been further reduced to a form that can be numerically integrated with ease. Details of the form and its validity are discussed in reference 33. For the heavy ions, the secondary production term (i.e., the second term on the right side of equation (5.24)) does not involve any integration; however, the interpolation of the transformed fluence function is based on the independent variable r_k, which is different from the range of ions r_j of type j given on the left side of the equation. To circumvent the problem, the equation is further modified by using the definition of $\tilde{S}_j(E)$, with E given in units of A MeV; then

$$\tilde{S}_j(E) = \tilde{S}_j(E_j/A_j) = -\frac{\Delta(E_j/A_j)}{\Delta x} = \frac{1}{A_j}\frac{\Delta E_j}{\Delta x} = \frac{1}{A_j}S_j(E_j) \tag{5.29}$$

with

$$S_j(E_j) = Z_j^2 S_p(E_j/A_j) \tag{5.30}$$

where S_p is the proton stopping power, and E_j is the energy in MeV of the ions of type *j*. Then

$$\tilde{S}_j(E) = \frac{1}{A_j} Z_j^2 S_p(E_j/A_j) \equiv \nu_j S_p(E_p) \tag{5.31}$$

where

$$E_p = E_j/A_j \tag{5.32}$$

By rewriting equation (5.19) as

$$\psi_j(x, r_j) \equiv \tilde{S}_j(E)\,\phi_j(x, E) = \nu_j S_p(E)\,\phi_j(x, E) \tag{5.33}$$

the new fluence function can be defined as

$$\psi_j'(x, r) \equiv \nu_j S_p(E)\,\phi(x, E) \equiv \psi_j(x, r_j) \tag{5.34}$$

with $r = r_p = \nu_j r_j$, where

$$r_p = \int_0^E \frac{dE'}{S_p(E')} \tag{5.35}$$

Equation (5.24) becomes

$$\psi_j'(x + h, r) = e^{-\sigma_j h}\psi_j'(x, r + \nu_j h) + \sum_k m_{jk}\sigma_k \left(\frac{e^{-\sigma_j h} - e^{-\sigma_k h}}{\sigma_k - \sigma_j} \right) \frac{\nu_k}{\nu_j} \psi_k'(x, r + \nu_j h) \tag{5.36}$$

so that there is now only one definition of range that is related to energy. The equation can be solved by setting up the proton range grid *r* and marching the solution from $x = 0$ by steps of *h* to the desired thickness.

5.3. Error Propagation

When considering how errors are propagated in the use of equation (5.36), the error is introduced locally by calculating $\psi_j'(x, r + \nu_j h)$ across the energy range grid. By limiting the analysis to the first term of equation (5.36), the error is defined at each range grid r_i such that

$$\psi_j'(x + h, r_i) = e^{-\sigma_j h}\psi_j'(x, r_i + \nu_j h) \tag{5.37}$$

The truncation error ε_i is introduced in the interpolation procedure for the value $\psi_{j,\,\mathrm{int}}'$ and

$$\psi_j'(x, r_i + \nu_j h) = \psi_{j,\,\mathrm{int}}'(x, r_i + \nu_j h) + \varepsilon_i(h) \tag{5.38}$$

After the *m*th step from the boundary, the numerical solution is

$$\psi_j'(mh, r_i) = e^{-\sigma_j h}\psi_{j,\,\mathrm{int}}'[(m-1)h, r_i + \nu_j h] + \sum_{l=0}^{m-1} e^{-\sigma_j (m-l) h}\varepsilon_l(h) \tag{5.39}$$

Suppose $0 \le \varepsilon_l(h) \le \varepsilon(h)$ for all *l*; then the propagated error is bounded by

$$\varepsilon_{\mathrm{prp}}(m) = \sum_{l=0}^{m-1} e^{-\sigma_j (m-l) h}\varepsilon_l(h) \le \varepsilon(h) \sum_{l=0}^{m-1} e^{-\sigma_j (m-l) h} \tag{5.40}$$

Note that

$$\sum_{l=0}^{m-1} e^{-\sigma_j mh} e^{\sigma_j hl} \approx \frac{1}{h\sigma_j}\left(1 - e^{-\sigma_j mh}\right) \tag{5.41}$$

because $h\sigma_j \ll 1$. Clearly, the propagated error on the mth step is bounded by

$$\varepsilon_{\text{prp}}(h) < \frac{\varepsilon(h)}{h\sigma_j}\left(1 - e^{-\sigma_j mh}\right) \tag{5.42}$$

where $\varepsilon(h)$ is the maximum error per step. With the increasing value of m, the propagated error grows with each step to a maximum value of $\varepsilon(h)/h\sigma_j$. Because the increase in the value of h is limited by the perturbation theory, the reduction of the local truncation error is the only viable approach left for reducing the propagated error to a desired level. The same consideration can be applied to the second term of equation (5.36) as the terms are similar in nature. The issue of error propagation in HZETRN is further studied by Shinn and Wilson. (See ref. 39.)

5.4. Numerical Algorithms

The error analysis of section 5.3 results in the conclusion that, to effectively reduce the level of propagated error, the local truncated error must be reduced. Three numerical algorithms are involved in solving equations (5.25)–(5.28) and (5.36): interpolation, integration, and grid generation. The choice of grid distribution that is interrelated to the interpolation and integration methods can increase the efficiency of the code if the number of grids can be reduced.

The interpolation method in HZETRN is the third-order Lagrange's method, which was used successfully in improving BRYNTRN. (See ref. 37.) With the four neighboring interpolation grids (data points) placed on both sides of the interpolated point, the error will tend to be the smallest in the middle interval of all the data points if the grid distribution is rather uniform. (See ref. 40.) The choice of a much higher order Lagrange's method will substantially decrease the efficiency of the computer code because there are more than 10 interpolation calls for each energy point at each step. Other interpolation methods such as a cubic spline were considered but discarded. In general, the splines are more accurate; however, their characteristically large oscillations can result in erroneous solutions.

The procedure for numerical integration that was used in the improved BRYNTRN (ref. 37) is also used here in HZETRN. The procedure is based on the compound quadrature formulation summing over all the subintervals between the grids with the midpoint evaluated by making use of the improved interpolation procedure mentioned previously. A simple numerical method such as Simpson's rule is used to integrate for the subintervals.

Three considerations dictate how the grids should be distributed. The first is the shape of the input spectrum. Because the GCR fluences are several orders of magnitude greater at the lower energies (refs. 41–43), a logarithmic scale is used for the energy or range coordinate as was done in reference 37. The second is the choice of the interpolation method, which requires that the four neighboring grids be as uniformly spaced on a logarithmic scale as possible so that the interpolation error can be minimized. Because the interpolation is performed on the range grid rather than on the energy grid, a uniform grid distribution on a logarithm of range r is desired. The third is the code efficiency, which increased almost quadratically with the decrease in the number of grid points. With the uniform grid points on a logarithmic scale r as the basic structure, the distribution can be modified further to reduce the number of points in the region in which the data are not propagating through the steps. For BRYNTRN, this region occurred below $r_{\min} + h$ (i.e., $\approx$1 g/cm^2) because $r_{\min} \ll 1$ and h is assumed to equal 1 g/cm^2. (See ref. 37.) This also applies to HZETRN, although the interpolation is now at $r_{\min} + \nu_j h$, where ν_j is always equal to or much greater than 1; because in propagating a distance h, all ions with energy below $r_{\min} + h$ are slowed to energies below the first energy grid point.

6. Stopping Power

In passing through a material, an ion loses the greater fraction of its energy to electronic excitation of the material. Although a satisfactory theory of high-energy ion-electron interaction is available in the form of Bethe's theory utilizing the Born approximation, an equally satisfactory theory for low energies is not available. Bethe's high-energy approximation of the energy loss per unit length (i.e., stopping power) is given by

$$S_e = \frac{4\pi N Z_p^2 Z_t e^4}{mv^2}\left\{\ln\left[\frac{2mv^2}{(1-\beta^2)\,I_t}\right] - \beta^2 - \frac{C}{Z_t}\right\} \tag{6.1}$$

where Z_p is the projectile charge, N is the number of target molecules per unit volume, Z_t is the number of electrons per target molecule, m is the electron mass, v is the projectile velocity, $\beta = v/c$, c is the velocity of light, C is the velocity-dependent shell correction term (ref. 44), and I_t is the mean excitation energy given by

$$Z_t \ln(I_t) = \sum_n f_n \ln(E_n) \tag{6.2}$$

where f_n are the electric dipole oscillator strengths of the target, and E_n are the corresponding excitation energies. The sum in equation (6.2) includes discrete and continuum levels. Molecular stopping power is reasonably approximated by the sum of the corresponding empirically derived *atomic* stopping powers for which equations (6.1) and (6.2) imply that

$$Z \ln(I) = \sum_j n_j Z_j \ln(I_j) \tag{6.3}$$

where Z and I pertain to the molecule, Z_j and I_j are the corresponding atomic values, and n_j are the stoichiometric coefficients. This additive rule (eq. (6.3)) is usually called Bragg's rule. (See ref. 45.)

As an input to HZETRN, the high-energy cutoff for the incident GCR spectrum is usually taken to be far beyond the minimum stopping power of ≈2A GeV, where Bethe's theory starts to overestimate and worsens as the energy increases. This overestimation can be corrected by considering that the field of the incoming ion projectile is perturbed by the neighboring polarized atoms. In HZETRN the approximate correction for the polarization effect (i.e., density effect) is based on the work of Sternheimer. (See ref. 46.) In reference 46, the polarization effect corrections for various elements and compounds were evaluated and fitted by the expressions

$$\delta = 0 \qquad (x < x_0) \tag{6.4a}$$

$$\delta = \ln\eta^2 + C + a\,(x_1 - x)^m \qquad (x_o < x < x_1) \tag{6.4b}$$

$$\delta = \ln\eta^2 + C \qquad (x > x_1) \tag{6.4c}$$

where δ is the density effect correction used in the stopping-power formula, $\eta = p/m_o c$, p is the momentum, m_o is the rest mass of the charged particle, c is the velocity of light, and

$$x = (\log_{10} e)\ln\eta = 0.43429 \ln\eta$$

The quantities a, m, x_o, and x_1 are constants that must be evaluated for each material; C is given by

$$C = -2 \ln(I/hv_p - 1) \tag{6.5}$$

where I is the mean ionization potential; the plasma energy $h\nu_p$ of the material is

$$h\nu_p = h\left(ne^2/nm_e\right)^{1/2} \tag{6.6}$$

where n is the electron density in electrons/cm^3, m_e is the rest mass, and e is the charge of an electron. For compounds and mixtures, the effective mean ionization potential can be determined by

$$\ln I = \frac{1}{n}\sum_t n_i \ln I_i \tag{6.7}$$

where n_i is the electron density for the ith element, and I_i is the corresponding atomic ionization potential.

Reference 46 suggests that, for some practical applications, the use of only the asymptotic density effect correction (eq. (6.4c)) may be adequate for all charged particle energies. In reference 47 Armstrong and Alsmiller compared the stopping-power differences between correct expressions and an asymptotic formula for several elements and compounds. The results indicated an overestimation of at most 6 percent when using the asymptotic formula. Therefore, only the asymptotic formula is used in HZETRN. Equation (6.1) with polarization effect modification becomes

$$S_e = \frac{4\pi NZ_p^2 Z_t e^4}{mv^2}\left\{\ln\left[\frac{2mv^2}{(1-\beta^2)\,I}\right] - \beta^2 - \frac{C}{Z_t} - \frac{\delta}{2}\right\} \tag{6.8}$$

The use of equation (6.8) in conjunction with the asymptotic formula of equation (6.4c) does not involve any evaluation of the constants a, m, x_o, and x_1 for the material considered. A comparison of equations (6.1) and (6.8) for different materials is discussed by Shinn et al. (See ref. 48.)

The electronic stopping power for protons is adequately described by equation (6.8) for energies >500 keV for which the shell correction C makes an important contribution up to 10 MeV. (See ref. 49.) For proton energies <500 keV, charge exchange reactions alter the proton charge over much of its path so that equation (6.8) is understood to be an average over the proton charge states. Normally, an average over the charge states is introduced into equation (6.8) so that the effective charge is the rms ion charge and not the average ion charge. At any ion energy, charge equilibrium is established very quickly in all materials. By utilizing the effective charge in equation (6.8), only modest improvement results at energies <500 keV, which presumably indicates the failure of this theory based on the Born approximation. (See refs. 49 and 50.)

The electronic stopping power for alpha particles requires terms in equation (6.8) of higher order in projectile charge Z_p because of corrections to the Born approximation. The alpha stopping power can not be related to the proton stopping power through their effective charges. Parametric fits to experimental data are given by Ziegler in reference 51 for all elements in both gaseous and condensed phases.

The electronic stopping powers for heavier ions are related to the alpha stopping power through their corresponding effective charges. HZETRN uses the effective charges suggested by Barkas (ref. 52) of

$$Z^* = Z_p\left[1 - \exp\left(-125\beta/Z_p^{2/3}\right)\right] \tag{6.9}$$

where Z_p in equation (6.9) is the atomic number of the ion.

At sufficiently low energies, the energy lost by an ion in a nuclear collision becomes important. The nuclear stopping-power theory used in HZETRN is a modification of the theory of Lindhard, Scharff, and Schiott. (See ref. 53.) The reduced energy is given as

$$\varepsilon = \frac{32.53 A_p A_t E}{Z_p Z_t (A_p + A_t)\left(Z_p^{2/3} + Z_t^{2/3}\right)^{1/2}} \tag{6.10}$$

where E is in units of A keV, and A_p and A_t are the atomic masses of the projectile and the target, respectively. The nuclear stopping power in reduced units (ref. 51) is

$$S_n = \begin{cases} 1.59\varepsilon^{1/2} & (\varepsilon < 0.01) \\ \dfrac{1.7\varepsilon^{1/2} \ln(\varepsilon + e^1)}{1 + 6.8\varepsilon + 3.4\varepsilon^{3/2}} & (0.01 < \varepsilon < 10) \\ \dfrac{\ln(0.47\varepsilon)}{2\varepsilon} & (10 < \varepsilon) \end{cases} \tag{6.11}$$

and the conversion factor to units of (eV-atoms/cm^2)/10^{15} is

$$f = \frac{8.426 Z_p A_t A_p}{(A_p + A_t)\left(Z_p^{2/3} + Z_t^{2/3}\right)^{1/2}}$$

The total stopping power S_j is obtained by summing the electronic and nuclear contributions. Other processes of energy transfer such as Bremsstrahlung and pair production for stopping massive ions are unimportant.

For energies greater than a few A MeV, Bethe's equation is adequate if the appropriate corrections to Bragg's rule (refs. 54–56), shell corrections (refs. 44, 49, and 50), and an effective charge are included. Electronic stopping power for protons is calculated from the parametric formulas of Andersen and Ziegler (ref. 49) with some modifications. (See ref. 9.)

Because alpha stopping power is not derivable from the formula for proton stopping power by using the effective charge at low energy, the parametric fits to empirical alpha stopping powers given by Ziegler (ref. 51) are used. Physical state and molecular binding effects are most important for hydrogen (ref. 54); water stopping power was approximated by using the condensed phase parameters for hydrogen and the gas phase experimentally derived parameters for oxygen. Electronic stopping powers for ions with a charge greater than 2 are related to the alpha stopping power by the effective charge of equation (6.9). Figures 2(a), 2(b), and 2(c) show the transport coefficient ranges and stopping powers for five different charge values Z, as calculated by HZETRN for aluminum, water, and liquid hydrogen targets, respectively.

7. Nuclear Database

The nuclear cross sections for neutron and proton interactions are described extensively in references 10 and 33. The heavy ion absorption cross sections σ_{abs} are currently derived from

$$\sigma_{abs} = \pi r_0^2 \left\{A_P^{1/3} + A_T^{1/3} - \left[0.200 + A_P^{-1} + A_T^{-1} - 0.292 \exp\left(-\frac{E}{792}\right)\cos\left(0.229 E^{0.453}\right)\right]\right\}^2 \left(1 + 5E^{-1}\right) \tag{7.1}$$

which for $r_0 = 1.26$ fm were fit to the quantum mechanical nuclear cross sections calculated in reference 57.

In this section, the heavy ion fragmentation mechanism is described by abrasion-ablation formalism. In the abrasion-ablation fragmentation model, the high-energy projectile nuclei collide with

stationary target nuclei. In the abrasion step, those portions of the nuclear volumes that overlap are sheared away by the collision. The remaining projectile piece, called ''a prefragment,'' continues its trajectory with essentially its precollision velocity. As a result of the dynamics of the abrasion process, the prefragment is highly excited and subsequently decays by the emission of nuclear particles. This step is the ablation stage. Final deexcitation is through gamma emission. The resultant isotope is the nuclear fragment whose cross section is measured. The abrasion process can be analyzed with classical geometric arguments (refs. 11, 36, and 58) or methods obtained from formal quantum scattering theory. (See refs. 59 and 60.) The ablation stage can be analyzed with geometric arguments (ref. 11) or more sophisticated methods based on Monte Carlo or intranuclear cascade techniques. (See refs. 61–64.) Predictions of fragmentation cross sections on hydrogen targets are made with the approximate semiempirical parameterization formulas of references 65 and 66. The fragmentation cross sections for other heavier targets are generated by the NUCFRG series of semiempirical fragmentation codes, in particular, the second version NUCFRG2 as described in reference 67.

The amount of nuclear material stripped away in the collision of two nuclei of radius R_P and R_T is taken as the volume of the overlap region times an average attenuation factor. (See refs. 36 and 67.) The relevant formula for the constituents in the overlap volume in the projectile is given by

$$\Delta_{\text{abr}} = FA_P\left[1 - \exp\left(-C_T/\lambda\right)\right] \tag{7.2}$$

where C_T is the chord length at maximum overlap density of the intersecting volume of the projectile and the target λ is the nuclear mean free path, and the expression for F depends on the nature of the collision (i.e., peripheral versus central) and the relative sizes of the colliding nuclei.

From reference 61, for $R_T > R_P$,

$$P = 0.125\,(\mu\nu)^{1/2}\left(\frac{1}{\mu} - 2\right)\left(\frac{1-\beta}{\nu}\right)^2 - 0.125\left[0.5\,(\mu\nu)^{1/2}\left(\frac{1}{\mu} - 2\right) + 1\right]\left(\frac{1-\beta}{\nu}\right)^3 \tag{7.3}$$

and

$$F = 0.75\,(1-\nu)^{1/2}\left(\frac{1-\beta}{\nu}\right)^2 - 0.125\left[3\,(1-\nu)^{1/2} - 1\right]\left(\frac{1-\beta}{\nu}\right)^3 \tag{7.4}$$

with

$$\nu = \frac{R_P}{R_P + R_T} \tag{7.5}$$

$$\beta = \frac{b}{R_P + R_T} \tag{7.6}$$

and

$$\mu = \frac{1}{\nu} - 1 = \frac{R_T}{R_P} \tag{7.7}$$

Equations (7.3) and (7.4) are valid when the collision is peripheral (the two nuclear volumes do not completely overlap). In this case, the impact parameter b is restricted such that

$$R_T - R_P \le b \le R_T + R_P \tag{7.8}$$

If the collision is central, then the projectile nucleus volume completely overlaps the target nucleus volume ($b < R_T - R_P$), and all the projectile nucleons are abraded. In this case, equations (7.3) and (7.4) are replaced by

$$P = -1 \tag{7.9}$$

and

$$F = 1 \tag{7.10}$$

and there is no ablation of the projectile because it was destroyed by the abrasion.

For a peripheral collision with $R_P > R_T$, equations (7.3) and (7.4) (ref. 63) become

$$P = 0.125\,(\mu\nu)^{1/2}\left(\frac{1}{\mu}-2\right)\left(\frac{1-\beta}{\nu}\right)^2 - 0.125\,\{0.5\left(\frac{\nu}{\mu}\right)^{1/2}\left(\frac{1}{\mu}-2\right)\frac{[\,(1/\nu)\,(1-\mu^2)^{1/2}-1\,]\,[\,(2-\mu)\,\mu\,]^{1/2}}{\mu^3}\}\left(\frac{1-\beta}{\nu}\right)^3 \tag{7.11}$$

and

$$F = 0.75\,(1-\nu)^{1/2}\left(\frac{1-\beta}{\nu}\right)^2 - 0.125\,\{\frac{3\,(1-\nu)^{1/2}}{\mu} - \frac{[\,1-(1-\mu^2)^{3/2}\,]\,[\,1-(1-\mu)^2\,]^{1/2}}{\mu^3}\}\left(\frac{1-\beta}{\nu}\right)^3 \tag{7.12}$$

where the impact parameter is restricted such that

$$R_P - R_T \le b \le R_P + R_T \tag{7.13}$$

For a central collision ($b < R_P - R_T$) with $R_P > R_T$, equations (7.11) and (7.12) become

$$P = \left[\frac{1}{\nu}\,(1-\mu^2)^{1/2} - 1\right]\left[1-\left(\frac{\beta}{\nu}\right)^2\right]^{1/2} \tag{7.14}$$

and

$$F = [\,1-(1-\mu^2)^{3/2}\,]\left[1-\left(\frac{\beta}{\nu}\right)^2\right]^{1/2} \tag{7.15}$$

The charge ratio of the nuclear matter removed by the collision is assumed to be that of the parent nucleus. The spectators in the overlap region are assumed loosely bound to the remaining prefragment and are lost in a preequilibrium emission process. (See ref. 67.)

The surface distortion excitation energy of the projectile prefragment following abrasion of the m nucleons is calculated from the clean-cut abrasion formalism of reference 58. For this model, the colliding nuclei are assumed to be uniform spheres with radii R_i ($i = P, T$). In collision, the overlapping volumes shear off so that the resultant projectile prefragment is a sphere with a cylindrical hole gouged out of it. The excitation energy is then determined by calculating the difference in surface area between the distorted sphere and a perfect sphere of equal volume. This excess surface area ΔS is given in reference 61 as

$$\Delta S = 4\pi R_p^2\,[\,1 + P - (1-F)^{2/3}\,] \tag{7.16}$$

where the expressions for P and F differ and depend upon the nature of the collision (i.e., peripheral versus central) and the relative sizes of the colliding nuclei, which were given in previous equations.

The excitation energy associated with surface energy is known to be 0.95 MeV/fm^2 for near-equilibrium nuclei so that

$$E_s' = 0.95\Delta S \tag{7.17}$$

for small surface distortions. When large numbers of nucleons are removed in the abrasion process, equation (7.17) is expected to be an underestimate of the actual excitation. This requires the introduction of an excess excitation factor (refs. 11 and 36) in terms of the number of abraded nucleons Δ_{abr} as

$$f = 1 + \frac{5\Delta_{abr}}{A_p} + [1500 - 320\,(A_p - 12)]\,\frac{\Delta_{abr}^3}{A_p^3} \tag{7.18}$$

which approaches 1 when the impact parameter is large but increases the excess excitation when many nucleons are removed and grossly distorted nuclei are formed by the collisions. (See ref. 11.) The quantity in the brackets accounts for light nuclei having greater excitation energy than heavier nuclei for the same fraction of mass removed (ref. 67) and is limited to values between 0 and 1500. The total excitation energy is then

$$E_s = E_s' f \tag{7.19}$$

which reduces to equation (7.17) for small Δ_{abr}. Also, the assumption is that 100 percent of the fragments with a mass of 5 are unbound, 90 percent of the fragments with a mass of 8 are unbound, and 50 percent of the fragments with a mass of 9 (^{9}B) are unbound. (See ref. 11.)

A secondary contribution to the excitation energy is the transfer of kinetic energy of relative motion across the intersecting boundary of the two ions. The rate of energy loss of a nucleon when it passes through nuclear matter (ref. 68) is taken as 13 MeV/fm, and the energy deposit is assumed to be symmetrically dispersed about the azimuth so that 6.5 (MeV/fm)/nucleon at the interface is the average rate of energy transfer into excitation energy. (See ref. 36.) This energy is transferred in single-particle collision processes, and the energy is transferred to excitation energy of the projectile for half of the events and leaves the projectile excitation energy unchanged for the remaining half of the events. (See ref. 11.) The first estimate of this contribution uses the length of the longest chord C_1 in the projectile surface interface. This chord length is the maximum distance traveled by any target constituent through the projectile interior. The number of other target constituents in the interior region can be found by estimating the maximum chord C_t transverse to the projectile velocity, which spans the projectile surface interface. (See ref. 36.) The total excitation energy from excess surface and spectator interaction is then

$$E_x' = 13 C_1 \left[1 + \frac{1}{3}\,(C_t - 1.5) \right] \tag{7.20}$$

where the second term contributes only if $C_t > 1.5$ fm. Also, the effective longitudinal chord length for these remaining nucleons is assumed to be one third of the maximum chord length.

The decay of highly excited nuclear states is dominated by heavy particle emission. In the present model, a nucleon is assumed to be removed for every 10 MeV of excitation energy. The number of ablated nucleons is

$$\Delta_{abl} = \frac{E_s + E_x}{10} \tag{7.21}$$

In accordance with the previously discussed directionality of the energy transfer, E_x has two values

$$E_x = \begin{cases} E_x' & \text{for } P_x = \dfrac{1}{2} \\ 0 & \text{for } P_{\bar{x}} = \dfrac{1}{2} \end{cases} \tag{7.22}$$

where P_x and $P_{\bar{x}}$ are the corresponding probabilities of occurrence of each value in collisions.

The number ΔA of nucleons removed through the abrasion-ablation process is given as a function of the impact parameter as

$$\Delta A = \Delta_{\text{abr}}(b) + \Delta_{\text{abl}}(b) \tag{7.23}$$

The cross section for the removal of ΔA nucleons is estimated as

$$\sigma(\Delta A) = \pi\left(b_2^2 - b_1^2\right) \tag{7.24}$$

where b_2 is the impact parameter for which the volume of the intersection of the projectile contains Δ_{abr} nucleons and the resulting excitation energies release an additional Δ_{abl} nucleons at the rate of 1 nucleon for every 10 MeV of excitation such that

$$\Delta_{\text{abr}}(b_2) + \Delta_{\text{abl}}(b_2) = \Delta A - \frac{1}{2} \tag{7.25}$$

similarly, for b_1

$$\Delta_{\text{abr}}(b_1) + \Delta_{\text{abl}}(b_1) = \Delta A + \frac{1}{2} \tag{7.26}$$

In the previous discussion, the assumption of straight-line trajectories makes the impact parameter b the distance of closest approach. This assumption makes the abrasion-ablation model a high-energy heavy ion fragmentation model; thus, Coulomb corrections due to low-energy trajectories must be added to the standard abrasion-ablation model. Equations (7.24)–(7.26) can be combined and rewritten (ref. 58) as

$$\sigma(\Delta A) = \pi\left[b\left(\Delta A - \frac{1}{2}\right)^2 - b\left(\Delta A + \frac{1}{2}\right)^2\right] \tag{7.27}$$

Equation (7.27) is retained in NUCFRG2 as written. However, b is no longer taken to be the distance of closest approach as used in equation (7.27) but is redefined in the following discussion.

The equations of motion in the nuclear Coulomb field are given by energy conservation as

$$E_{\text{tot}} = \frac{1}{2}\mu\dot{r}^2 + \frac{l^2}{2\mu r^2} + \frac{Z_P Z_T e^2}{r} \tag{7.28}$$

where E_{tot} is the total kinetic energy in the center-of-mass system at great relative distances, r is the relative distance between the charge centers with time derivative $\dot{r}$, μ is the reduced mass, l is the angular momentum, Z_P and Z_T are the atomic numbers of the projectile and target nucleus, respectively, and e is the electronic charge. The angular momentum is given as

$$l^2 = 2\mu E_{\text{tot}} b^2 \tag{7.29}$$

With the use of equation (7.29) and $\dot{r} = 0$, equation (7.28) becomes

$$E_{\text{tot}} = \frac{E_{\text{tot}} b^2}{r^2} + \frac{Z_P Z_T e^2}{r} \tag{7.30}$$

which can be written as

$$b^2 = r(r - r_m) \tag{7.31}$$

where

$$r_m = \frac{Z_P Z_T e^2}{E_{\text{tot}}} \tag{7.32}$$

Note that r_m is the distance of closest approach for the zero impact parameter. For a given ΔA, equation (7.32) is used in NUCFRG2 to calculate the distance of closest approach and equation (7.31) is used to calculate the impact parameter, which permits extrapolation backward in time along the Coulomb trajectory to the initial impact parameter. (See ref. 69.) This calculated value of b is used in equation (7.27) to evaluate the cross section. Note that the effect of the Coulomb trajectory is to move the separation at impact r to smaller impact parameters b and thus reduce the cross sections, especially at low energy.

A second correction to the trajectory calculation comes from the transfer of kinetic energy into binding energy in the release of particles from the projectile. The total kinetic energy in passing through the reaction zone is reduced from the initial energy E_i to the final energy E_f

$$E_f = E_i - 10\Delta A \tag{7.33}$$

by assuming that 10 MeV is the average binding energy. The kinetic energy used in the closest approach calculation is the average

$$E_{\text{tot}} = \frac{1}{2}(E_i + E_f) = E_i - \frac{1}{2}(10\Delta A) \tag{7.34}$$

As given by equation (7.34), E_{tot} is obviously very crude and equation (7.34) can be refined further.

The distribution of charge Z_F of final projectile fragments of mass A_F are strongly affected by nuclear stability. The charge distribution for a given $\sigma(\Delta A)$ as described by Rudstam (ref. 70) is

$$\sigma(A_F, Z_F) = F_1 \exp\left(-R\left|Z_F - SA_F + TA_F^2\right|^{3/2}\right)\sigma(\Delta A) \tag{7.35}$$

where $R = 11.8/A_F^D$, $D = 0.45$, $S = 0.486$, $T = 3.8 \times 10^{-4}$, and F_1 is a normalizing factor such that

$$\sum_{Z_F} \sigma(A_F, Z_F) = \sigma(\Delta A) \tag{7.36}$$

The Rudstam formula for $\sigma(\Delta A)$ was not used because the ΔA dependence is too simple and breaks down for heavy targets (refs. 11, 36, 71, and 72) and was replaced by equation (7.27) in the abrasion-ablation fragmentation model.

The charge of the removed nucleons ΔZ is calculated according to charge conservation

$$Z_P = Z_F + \Delta Z \tag{7.37}$$

and is divided between the nucleons and hydrogen and helium isotopes according to the following four rules:

1. The abraded nucleons are those removed from that portion of the projectile in the region of overlap with the target. (See ref. 67.) Therefore, the abraded nucleon charge is assumed to be proportional to the charge fraction of the projectile nucleus as

$$Z_{\text{abr}} = Z_P \Delta_{\text{abr}} / A_P \tag{7.38}$$

This, of course, ignores the charge separation caused by the giant dipole resonance model of reference 63. The charge release in the ablation stage is then

$$Z_{\text{abl}} = \Delta Z - Z_{\text{abr}} \tag{7.39}$$

which simply conserves the remaining charge.

2. The alpha particle is known to be unusually tightly bound in comparison with other nucleon arrangements. Because of this unusually tight binding of the alpha particles, the helium production is maximized in the ablation process. (See refs. 11 and 36.) The number of alpha particles is

$$N_{\alpha} = \left[\text{Int}\left(Z_{\text{abl}}/2\right), \text{Int}\left(A_{\text{abl}}/4\right)\right]_{\min} \tag{7.40}$$

where Int(x) denotes the integer part of x. The remaining isotopes are likewise maximized from the remaining ablated mass and charge in the order of decreasing binding energy. (See ref. 69.) The number of protons N_p produced is given by charge conservation as

$$N_p = Z_{\text{abl}} - \sum_i Z_i N_i \tag{7.41}$$

where i ranges over all ablated particles of mass 2, 3, and 4. Similarly, mass conservation requires the number of neutrons N_n produced to be

$$N_n = A_{\text{abl}} - N_p - \sum_i A_i N_i \tag{7.42}$$

3. The calculation is performed for $\Delta A = 1$ to $\Delta A = A_P - 1$, for which the cross section associated with $\Delta A > A_P - 0.5$ is omitted. These are, of course, the central collisions for which the projectile is assumed to disintegrate into single nucleons if $r_P < r_T$. Then

$$N_p = Z_P \tag{7.43}$$

$$N_n = A_P - Z_P \tag{7.44}$$

Other collision products such as the energetic target fragments and mesonic components are ignored. The peripheral collisions with $\Delta A < 0.5$ are also ignored. Most important in these near collisions is the Coulomb dissociation process. (See ref. 73.)

4. The description of the nuclear radius is given by

$$R = 1.29\left(R_{\text{rms}}^2 - R_p^2\right) \tag{7.45}$$

where R_{rms} is the rms radius of the nucleus charge distribution and R_p is the radius of the proton charge distribution. The improvements to the abrasion-ablation model as implemented in NUCFRG2 and comparison with experiments are further described in references 74 and 75.

Finally, the electromagnetic (EM) dissociation cross-section contributions to the nuclear database as implemented in NUCFRG2 must be considered. In electromagnetic dissociation, the virtual photon field of the target nucleus interacts electromagnetically with the constituents of the projectile to cause excitation and eventual breakup. The electromagnetic dissociation model implemented in NUCFRG2 is limited to single nucleon (proton or neutron) removal processes.

The total electromagnetic cross section for one nucleon removal resulting from electric dipole ($E1$) and electric quadrupole ($E2$) interactions is written

$$\begin{aligned}\sigma_{\mathrm{em}} &= \sigma_{E1} + \sigma_{E2} \\ &= \int [N_{E1}(E)\,\sigma_{E1}(E) + N_{E2}(E)\,\sigma_{E2}(E)]\; dE\end{aligned} \tag{7.46}$$

where the virtual photon spectra of energy E produced by the target nucleus (ref. 76) are given for the dipole field by

$$N_{E1}(E) = \frac{1}{E}\frac{2}{\pi}Z^2\alpha\frac{1}{\beta^2}\left[\xi K_0K_1 - \frac{1}{2}\xi^2\beta^2\left(K_1^2 - K_0^2\right)\right] \tag{7.47}$$

and for the quadrupole field by

$$N_{E2}(E) = \frac{1}{E}\frac{2}{\pi}Z^2\alpha\frac{1}{\beta^4}\left[2(1-\beta^2)K_1^2 + \xi(2-\beta^2)^2K_0K_1 - \frac{1}{2}\xi^2\beta^4\left(K_1^2 - K_0^2\right)\right] \tag{7.48}$$

The terms $\sigma_{E1}(E)$ and $\sigma_{E2}(E)$ are the corresponding photonuclear reaction cross sections for the fragmenting projectile nuclei. The terms K_0 and K_1 in the expression for N_{E1} and N_{E2} are modified Bessel functions of the second kind and are also functions of the parameter ξ. The latter is

$$\xi = \frac{2\pi E b_{\mathrm{min}}}{\gamma\beta hc} \tag{7.49}$$

where E is the virtual photon energy, b_{min} is the minimum impact parameter below which the collision dynamics are dominated by nuclear interactions rather than by EM interactions, β is the speed of the target measured from the projectile rest frame as a fraction of the speed of light c, h is Planck's constant, and γ is the usual Lorentz's factor from special relativity $\gamma = (1-\beta^2)^{-1/2}$. The minimum impact parameter is

$$b_{\mathrm{min}} = (1 + x_d)\,b_c + \frac{\pi a_0}{2\pi} \tag{7.50}$$

where $x_d = 0.25$ and

$$a_0 = \frac{Z_P Z_T e^2}{m_0 v^2} \tag{7.51}$$

allows for trajectory deviation from a straight line. (See ref. 77.) The critical impact parameter for single-nucleon removal is

$$b_c = 1.34\left[A_P^{1/3} + A_T^{1/3} - 0.75\left(A_P^{-1/3} + A_T^{-1/3}\right)\right] \tag{7.52}$$

with A_P and A_T being the projectile and target nucleon numbers, respectively.

The photonuclear cross sections $\sigma_{E1}(E)$ and $\sigma_{E2}(E)$ are Lorentzian shaped and somewhat sharply peaked in energy. Therefore, photon spectral functions can be taken outside of the integral of equation (7.46) to yield the approximate form (ref. 76) of

$$\sigma_{\mathrm{em}} \approx N_{E1}(E_{\mathrm{GDR}})\int\sigma_{E1}(E)\; dE + N_{E2}(E_{\mathrm{GQR}})\,E_{\mathrm{GQR}}^2\int\sigma_{E2}(E)\;\frac{dE}{E^2} \tag{7.53}$$

where E_{GDR} and E_{GQR} are the energies at the peaks of the $E1$ and $E2$ photonuclear cross sections, respectively. These integrals of photonuclear cross sections, integrated over energy, are evaluated with the following sum rules (ref. 76):

$$\int \sigma_{E1}(E)\ dE = 60\frac{N_P Z_P}{A_P} \tag{7.54}$$

and

$$\int \sigma_{E2}(E)\ \frac{dE}{E^2} = 0.22 f Z_P A_P^{2/3} \tag{7.55}$$

In equations (7.54) and (7.55), N_P is the number of neutrons, Z_P is the number of protons, and A_P is the mass number of the projectile nucleus. The fractional exhaustion of the energy-weighted sum rule in equation (7.55) (ref. 68) is

$$f = \begin{cases} 0.9 & (A_P > 100) \\ 0.6 & (40 < A_P \le 100) \\ 0.3 & (40 \le A_P) \end{cases} \tag{7.56}$$

In equation (7.53), E_{GDR} and E_{GQR} are the energies at the peaks of the $E1$ and $E2$ photonuclear cross sections, respectively. For the dipole term (ref. 68),

$$E_{\mathrm{GDR}} = \frac{hc}{2\pi}\left[\frac{m^* c^2 R_0^2}{8J}\left(1 + u - \frac{1 + \varepsilon + 3u}{1 + \varepsilon + u}\varepsilon\right)\right]^{-1/2} \tag{7.57}$$

with

$$u = \frac{3J}{Q'} A_P^{-1/3} \tag{7.58}$$

and

$$R_0 = r_0 A_P^{1/3} \tag{7.59}$$

where $\varepsilon = 0.0768$, $Q' = 17$ MeV, $J = 36.8$ MeV, $r_0 = 1.18$ fm, and m^* is 0.70 of the nucleon mass. For the quadrupole term,

$$E_{\mathrm{GQR}} = \frac{63}{A_P^{1/3}} \tag{7.60}$$

Finally, the single-proton or single-neutron removal cross sections are obtained from σ_{em} (eq. (7.53)) by using proton- and neutron-branching ratios $g_i\,(i = p, n)$. Then

$$\sigma(i) = g_i \sigma_{\mathrm{em}} \qquad (i = p \text{ or } n) \tag{7.61}$$

The proton-branching ratio has been parameterized by Westfall et al. (ref. 68) as

$$g_p = \min\left[\frac{Z_P}{A_P}, 1.95 \exp(-0.075 Z_P)\right] \tag{7.62}$$

where Z_P is the number of protons, and the minimum value of the two quantities in brackets is to be taken. This parameterization is satisfactory for heavier nuclei $(Z_P > 14)$; however, for light nuclei, the following branching ratios are used instead:

$$g_p = \begin{cases} 0.5 & (Z_P < 6) \\ 0.6 & (6 \le Z_P \le 8) \\ 0.7 & (8 < Z_P < 14) \end{cases} \tag{7.63}$$

For neutrons, the branching ratio is

$$g_n = 1 - g_p \tag{7.64}$$

Figure 3 shows the absorption cross section as a function of energy for six different projectile charge numbers Z_P, as calculated by HZETRN for aluminum, water, and liquid hydrogen targets. The importance of the target size on the systematic variation of the absorption cross section with projectile mass is clearly seen. Small target nuclei preferentially fragmentize heavy ions, which is important to shield performance. (See ref. 78.)

Among the best known fragmentation cross sections are those for carbon ion beams on carbon targets. Measurements have been made at four energies (250*A* MeV in ref. 79, 600*A* MeV in ref. 80, and 1.05*A* and 2.1*A* GeV in ref. 81) and are compared in figure 4 with the results from NUCFRG2 cross-section calculation. The effects of the Coulomb trajectory are clearly apparent on the lighter mass fragments of lithium and beryllium which exhibit a change in slope below 100*A* MeV. Such Coulomb effects will be even more important for projectile and fragments of greater charge. Figure 5 shows the results of very-low-energy (11.7*A* MeV) oxygen projectiles onto a molybdenum target (ref. 82) where Coulomb effects are very important. The resulting charge removal cross sections seem well represented by NUCFRG2 calculation even at low energies. The process whereby a nucleon is exchanged between the oxygen projectile and the target nucleus is referred to as ''exchange poles.'' As shown in figure 5, the addition of exchange poles to the model will bring charge removal cross sections into agreement as can be judged by the proton exchange pole (neutron removal) contribution for proton exchange.

Figure 6 shows three projectile-target combinations for which two groups of experimenters have taken measurements at nearly the same energy (1.55*A* GeV in ref. 83 and 1.88*A* GeV in ref. 84). On the basis of NUCFRG2 calculations, very small cross-section differences are expected to exist at these high energies. (See fig. 4.) Cross sections NUCFRG2 tend to favor the data of Westfall et al. (ref. 84) and lie 10 to 50 percent above that of Cummings et al. (See ref. 83.) Perhaps the most encouraging result of the comparison with the data of Cummings et al. is that trends in NUCFRG2 below aluminum measurements $(Z_F = 13)$ of Westfall et al. appear in reasonable agreement with the results of Cummings et al. down to neon fragments $(Z_F = 10)$. The NUCFRG2 fragmentation cross sections below neon remains untested.

To better quantify the comparison of results shown in figure 6, χ^2 analysis is used. The test data of the fragmentation model in NUCFRG2 are compared with the experimental data of Cummings et al. (ref. 83) and Westfall et al. (ref. 84) and shown in table I for iron projectiles on three targets. Shown in table I are the total χ^2 values and the average χ^2 contributions per degree of freedom n. Clearly, the data for producing aluminum fragments in the experiments of Westfall et al. show large systematic errors, which are nearly the sole contribution to the χ^2 values. The elimination of the aluminum data from the experiments of Westfall et al. is shown in the table as the values in parentheses. By excluding the aluminum data, the model then shows good agreement with the data of Westfall et al. for carbon and copper targets. The greater discrepancy for the lead targets surely results from the simplified nuclear matter distribution; the use of a diffusive surface model rather than the uniform sphere model is recommended. When comparing the model with the data of Cummings et al., similar trends are shown with

target mass, but the overall agreement with the data of Cummings et al. is inferior to the agreement with the data of Westfall et al. as was previously noted in the discussion of figure 6.

Table I. χ^2 Analysis of Iron Fragmentation Model

Shield + target	NUCFRG2-Westfall[a]		NUCFRG2-Cummings	
	χ^2	χ^2/n	χ^2	χ^2/n
Fe + C	50.2 (16.0)	5 (1.8)	48.3	3.7
Fe + Cu	200.6 (22.9)	20 (2.5)	78.1	6.0
Fe + Pb	177.4 (56.2)	18 (6.2)	83.1	6.7

[a]All values in parentheses exclude Westfall's aluminum cross section.

The χ^2 analysis has been used to compare how well the results of one experimental group compare with the results of another. Such a comparison is shown in table II. Again, the values in parentheses eliminate the aluminum data contribution of Westfall et al. What is clear from table II is that the model represents the two sets of experimental data better than either experimental data set represents the other. This is the best that can be hoped for within the present experimental uncertainty.

Table II. χ^2 Analysis of Iron Fragmentation Experiments

Shield + target	Westfall[a]-Cummings		Cummings-Westfall[a]	
	χ^2	χ^2/n	χ^2	χ^2/n
Fe + C	85.6 (43.3)	8.6 (4.8)	54.6 (33.6)	5.5 (3.7)
Fe + Cu	424.4 (108.4)	42.4 (12.0)	160.3 (69.4)	16.0 (7.7)
Fe + Pb	348.8 (79.5)	34.9 (8.8)	143.4 (55.8)	14.3 (6.2)

[a]All values in parentheses exclude Westfall's aluminum cross section.

Figures 7(a), 7(b), and 7(c) show the fragmentation cross sections as calculated by NUCFRG2 as a function of projectile and fragment mass numbers at four different projectile energies for aluminum, water, and liquid hydrogen targets, respectively. It is difficult to interpret the data directly in terms of shield performance. However, the ion fragmentation at lower energies is clearly most effective for complex target nuclei as can be seen by comparing the aluminum cross sections at 25*A* MeV in figure 7(a) with those of liquid hydrogen in figure 7(c). In contrast at high energies, the hydrogen target distributes the mass of the fragments more broadly than the aluminum targets as seen by comparing the results at 2400*A* MeV in figures 7(a) and 7(c). The water target displays both of these characteristics simultaneously.

8. Environmental Model

Calculations and measurements show that HZE ions in GCR particle fluxes vary inversely with solar activity. This dependency indicates that, at maximum solar activity, the GCR particle flux is at a minimum, and at minimum solar activity, the GCR particle flux reaches a maximum. This process of flux variation results from the shielding of the inner part of the solar system by the magnetic fields that are being carried away from the solar surface by the solar wind and varies periodically during an 11- to 13-year cycle. This shielding process is particularly effective in low-energy GCR particles. Calculations have shown that, for energies of 100*A* MeV or less, the GCR particle flux variation between solar minimum and solar maximum is a factor of 10 or more. At GCR particle energies above a few hundred *A* MeV, the effect of solar modulation on GCR particle flux gradually decreases and above approximately 10*A* GeV becomes negligible.

A numerical description of the previous solar modulation must be supplied as an input to the environmental model of any space radiation transport computer code including HZETRN. The environmental model of Badhwar and O'Neill is used in HZETRN. (See ref. 42.) This model is based on fitting measured differential energy spectra of 1954–1989 to stationary Fokker-Planck equation solutions to estimate the diffusion coefficient or the equivalent deceleration parameter Φ in units of MV. Reference 42 shows that, independent of energy, this approach fits the available data within an error of ±10 percent rms. By using the calculated diffusion coefficient, the GCR spectra of hydrogen, helium, carbon, oxygen, silicon, and iron are estimated. The spectra of the remaining elements were scaled to the previous elements by following reference 43. The environmental model data (i.e., solar maxima-minima) available in HZETRN are for the years 1958–1959, 1970–1971, 1981–1982, and 1989 solar maxima and 1965, 1977, and 1986–1987 solar minima.

Based on the model of reference 42 used in HZETRN, figure 8 shows the predicted fluxes of 1977 solar minimum and 1981 solar maximum as a function of energy for five different charge groups. Figure 9 shows the flux ratio of the 1981 solar maximum compared with the 1977 solar minimum for five different charge groups in the energy range of 0.1 to 10^6 MeV. As discussed previously, the two spectra are essentially identical at energies above 50*A* GeV, while at lower energies, the ratio can be 1:10 or less depending on the ion type.

Solar flare occurrence is correlated with solar activity and the most important events seem to occur during the ascending or descending phase of the solar cycle. The four solar particle events (SPE) of February 1956, November 1960, August 1972, and October 1989 are widely used to estimate flare-shielding requirements. Fitted fluence energy spectra of these four events (refs. 85–88), King's-fitted spectrum of 1972, and Webber's fit (ref. 89) are as follows:

1. February 1956

$$\phi_P(>E) = 1.5\times10^9 \exp\left(-\frac{E-10}{25}\right) + 3\times10^8 \exp\left(-\frac{E-100}{320}\right)$$

2. November 1960

$$\phi_P(>E) = 7.6\times10^9 \exp\left(-\frac{E-10}{12}\right) + 3.9\times10^8 \exp\left(-\frac{E-100}{80}\right)$$

3. August 1972

$$\phi_P(>E) = 6.6\times10^8 \exp\left(-\frac{E-100}{30}\right)$$

4. October 1989

$$\phi_P(>E) = 8.65\times10^{10} \exp\left[-\frac{P(E)}{59.261}\right]$$

5. August 1972 (King spectrum)

$$\phi_P(>E) = 7.9\times10^9 \exp\left(-\frac{E-30}{26.5}\right)$$

6. Webber spectrum with 100 MV rigidity

$$\phi_P(>E) = 1.0\times10^9 \exp\left[\frac{239.1-P(E)}{100}\right]$$

where E is the energy in MeV, $P(E) = \sqrt{E(E+1876)}$ is the rigidity, and $\phi_P(>E)$ is the proton integral fluence in protons/cm^2. Figure 10 shows the fitted spectra. The flare of October 1989 produced

the greatest number of protons less than 4 MeV, and the flare of August 1972 produced the greatest number of protons between 4 and 150 MeV. The February 1956 flare produced approximately one tenth as many protons greater than 10 MeV as the 1972 and 1989 flares, but it delivered far more protons of 200 MeV or greater than the three other flares. The November 1960 flare exhibited intermediate characteristics.

9. HZETRN Benchmarking

In this section, the subject of HZETRN validation is addressed. Ideally, validation should be accomplished with detailed transport data obtained from carefully planned and controlled experiments; unfortunately, such data are scarce. Although useful for comparative purposes, the atmospheric propagation measurements (ref. 36) used previously are clearly not definitive because they consist of integral fluences of as many as 10 different nuclear species combined into a single datum. Although limited quantities of HZE dosimetry measurements from manned space missions (e.g., Skylab) are available (ref. 90), numerous assumptions about the relationship between the dosimeter location and spacecraft shield thickness and geometry must be made to estimate astronaut dose with GCR codes. Because many of these assumptions may involve inherently great uncertainties (i.e., factors of 2 or greater), differences in results are difficult to attribute to the particular assumptions or approximations that may have been used in the analysis. Without definitive GCR transport measurements with which to compare code predictions, other methods of validation must be considered. One such method is to compare HZETRN with limited available proton transport Monte Carlo results. (See ref. 87.)

In reference 87 comparisons of the results obtained for a hypothetical problem with four different proton transport codes are presented. The hypothetical problem was to determine the dose, as a function of depth in water, resulting from a typical solar flare proton spectrum normally incident on a semi-infinite slab shield which is followed by the slab of water. The water was assumed to be 30 g/cm^2 thick. The solar proton spectrum was taken to be exponential in rigidity (Webber spectrum of section 8) with a characteristic rigidity of 100 MV and was normalized to 10^9 protons/cm^2 with energy >30 MeV. The Nucleon Transport Code (NTC) (ref. 91) is used here and compared with HZETRN.

Figures 11(a) and 11(b) show the total dose in gray (Gy) and total dose equivalent in sievert (Sv) for 20 g/cm^2 shields of aluminum and iron, respectively, followed by 30 g/cm^2 of water. For both shields, the code correlation is good. At water depths >20 g/cm^2, HZETRN predictions are slightly greater than NTC because of the 400-MeV cutoff in the NTC calculation. (See ref. 37.)

Figures 12(a) and 12(b) show the secondary neutron dose in gray (Gy) and secondary neutron dose equivalent in sievert (Sv) for 20 g/cm^2 shields of aluminum and iron, respectively, followed by 30 g/cm^2 of water. For both shields, the code correlation is only fair, which results partly from the grid coarseness of the Monte Carlo secondary neutron prediction runs and current limitations in the neutron transport database and elastic scattering propagation. (See ref. 33.)

Other comparisons of HZETRN with analytic functions are reported in references 35, 39, and 75.

10. HZETRN Computational Results

In this section results from applying HZETRN to different targets and environmental periods (i.e., solar minimum or maximum) are presented to provide a sufficiently broad database for code testing. The emphasis is on information that can be extracted directly from a typical execution of HZETRN. Therefore, environmental periods of the 1977 solar minimum and 1981 solar maximum and target materials of aluminum, water, and liquid hydrogen are used. Although HZETRN-calculated dose equivalent results are based on the International Commission on Radiological Protection ICRP-26 and ICRP-60 (refs. 92 and 93) quality factor recommendations, only the dose equivalent results for ICRP-60 are shown here. The calculations include the following results for skin dose and blood-forming organ (BFO) dose:

1. Flux contributions from carbon, oxygen, calcium, and iron ions at different energies
2. Total and individual ions, dose and dose equivalent contributions for skin (0-cm surface dose), and BFO (5-cm-depth dose) at different depths
3. Flux contributions, total dose and dose equivalent contributions for skin (0 cm), and BFO (5 cm) at different linear energy transfers (LET)

Major shortcomings of the HZETRN calculations are as follows:

1. All secondary particles from HZE interactions are presently assumed to be produced with a velocity equal to that of the incident particle; this is conservative for neutrons produced in HZE particle fragmentations
2. Meson contributions to the propagating radiation fields are neglected
3. Target fragments in HZE reactions are neglected
4. Angular dependence, especially in neutron propagation is neglected

These data are not all conservative and probably account for the 15- to 30-percent underestimation of the exposure. As discussed in references 94 and 95, the main sources of uncertainty are the input nuclear fragmentation model and the incident GCR spectrum. Taken together, they could easily impose an uncertainty factor of 2 or more in the astronaut risk estimate. This is especially true for track structure dependent biological models. (See refs. 78 and 96.)

Figures 13–16 show the flux of carbon, oxygen, calcium, and iron ions in aluminum targets for the 1977 and 1981 solar periods at depths of 0, 10, 20, and 30 g/cm^2 in the energy range of $10^{-2}A$ to 10^5A MeV. Similarly, figures 17–24 show the flux for water and liquid hydrogen targets. In all figures the effect of solar minimum and solar maximum periods are demonstrated through a reduction in the magnitude of the particular ion flux during solar maximum. Figures 13–24 demonstrate that lighter target materials such as liquid hydrogen have better attenuation characteristics than heavier target materials such as aluminum for all target depths.

Figure 25 shows skin dose, Gy and dose equivalent, Sv, when using ICRP-60 quality factors in aluminum, water, and liquid hydrogen targets for the 1977 and 1981, 1982 solar periods at depths of 0 to 30 g/cm^2. Only a modest gain in protection is displayed by aluminum shielding. A water shield shows substantially better attenuation characteristics. Liquid hydrogen has excellent shielding characteristics. These results are demonstrated more clearly in figure 26, which shows skin dose, Gy, and dose equivalent, Sv, when using ICRP-60 quality factors in aluminum, water, and liquid hydrogen targets for the 1977 and 1981 solar periods at depths of 0 to 30 g/cm^2. In figure 26, the effect of the atomic and nuclear properties of the target is demonstrated by increases in skin doses for larger target nuclei.

Figures 27–29 show skin dose, Gy, and figures 30–32 show dose equivalent, Sv, when using ICRP-60 quality factors for six different charge groups in aluminum, water, and liquid hydrogen targets for the 1977 and 1981 solar periods at depths of 0 to 30 g/cm^2. The better attenuation properties of the liquid hydrogen target versus aluminum target at all target depths are shown for the given charge groups for both solar epochs.

Figures 33–40 show the attenuation behavior of GCR in aluminum, water, and liquid hydrogen at the 5-cm-BFO depth. The dosimetric characteristics of different target materials as a function of target depth are similar to those in figures 13–32, except here an additional attenuation exists in all data because of an additional 5 g/cm^2 of water.

Figures 41–49 show skin flux and dosimetric characteristics of GCR components in aluminum, water, and liquid hydrogen targets for the 1977 and 1981 solar periods for the LET range of 1 to 10^5 MeV/cm of water at depths of 0, 10, 20, and 30 g/cm^2. The presence of the primary components of

GCR from proton to iron is clearly demonstrated as inflections in all figures. The attenuation characteristics of lighter targets such as liquid hydrogen versus heavier targets such as aluminum are shown at all depths and LET ranges.

Figures 50–58 show 5-cm-BFO flux and dosimetric characteristics of GCR components in aluminum, water, and liquid hydrogen targets for the 1977 and 1981 solar periods for the LET range of 1 to 10^5 MeV/cm of water at depths of 0, 10, 20, and 30 g/cm^2. As before, the dosimetric characteristics of different target materials as a function of target depth are similar to those in figures 41–49, except here an additional attenuation exists in all figures because of an additional 5 g/cm^2 of water. As in figures 41–49, the presence of the primary components of GCR from proton to iron is clearly demonstrated as inflections, and the attenuation characteristics of lighter targets such as liquid hydrogen versus heavier targets such as aluminum are shown at all depths and LET ranges.

The use of the HZETRN code and the control of the options to generate a typical output are discussed in appendix A. A complete sample output with the options of appendix A is provided in appendix B.

11. Concluding Remarks

The study of free-space radiations is essential for estimation of the risk factors for long-duration manned space flights. The estimates of galactic cosmic ray (GCR) ion flux inside a space module can be made by calculating quantities such as energy and linear energy transfer (LET) spectra. The estimation of doses and LET spectra by numerical predictive techniques, such as HZETRN, is essential for any long-duration manned space mission.

This paper reports the progress in computer code development for space radiation studies and shield design for future NASA space programs; the HZETRN code is a state-of-the-art fast computational tool available for a design engineer to obtain answers to some of the radiation questions that arise in planning any mission. However, major uncertainties in nuclear cross sections, environmental models, and astronaut risk affect the overall accuracy of the predictions of any analytical-computational technique. These uncertainties have a major impact on the proposed shield design for any mission and the subsequent mission cost. Much work remains to accurately resolve the problems with nuclear cross-section calculations, environmental model development, and risk estimate methods.

NASA Langley Research Center
Hampton, VA 23681-0001
February 14, 1995

Appendix A

HZETRN Description

A1. Program Structure

The main program and each subroutine or function module begins with a brief description of its purpose. The program has 8358 lines, is written in FORTRAN 77, and was developed on a VAX 4000 scaler minicomputer under the VMS operating system; in its current version, the program requires 463 blocks (237056 bytes) of storage space. However, the program is essentially platform and operating system independent. The complete computer code consists of a main program HZETRN, 63 subroutines, and 37 function modules. Table AI provides a list of the subroutines and function modules in the order in which they appear in the program. The overall structure of HZETRN is shown in figure A1, which includes input requirements and output options.

Table AI. HZETRN Program Modules

No.	Program module	Type[a]	No.	Program module	Type[a]	No.	Program module	Type[a]
1	MATTER	S	35	DENSEFF	F	69	FB	F
2	DMETRIC	S	36	ATOPA	S	70	SLOPE	F
3	PRPGT	S	37	ACOEF	F	71	ELSEC	F
4	OD	F	38	CCOEF	F	72	XTOT	F
5	TS	F	39	ATOPN	S	73	XTOTLM	F
6	F2	S	40	BUILD	F	74	XSEC	F
7	FRAG	F	41	SNF	F	75	ABSEC	F
8	XSECFRG	F	42	TEXP	F	76	LZEVAP	S
9	YIELDX	S	43	TSQR	F	77	ASIGM	S
10	YIELDN	S	44	RMAT	F	78	XTEST	S
11	YIELDA	S	45	SIONA	F	79	SPLCN	S
12	YIELDT	S	46	ZEFF	F	80	SPLIN	S
13	PXN	S	47	RTIS	F	81	PRPLI	S
14	YIELD1	S	48	MGAUSS	S	82	FD	S
15	YIELD2	S	49	IUNI	S*	83	LITEST	S
16	YIELD3	S	50	IBI	S*	84	TBARLI	S
17	YIELD4	S	51	QXZ114	F*	85	LIFRAG	S
18	NAND	F	52	QXZ115	S*	86	RADIUS	F
19	YIELDH	S	53	QXZ116	S*	87	XLISEC	F
20	YIELDLI	S	54	QXZ117	S*	88	LKOSPC	S
21	YIELDEM	F	55	SUTPAR	S*	89	E3MAX	F
22	BESSEL	F	56	QXZ060	S*	90	WDKO	S
23	GEODA	S	57	QXZ061	S*	91	LQESPC	S
24	BSEACH	S	58	QXZ062	S*	92	WQE	F
25	DELTA	S	59	QXZ063	F*	93	DERF	F
26	FPOFB	S	60	QXZ111	S*	94	GCRFLUX	S
27	LIMIT	S	61	QXZ112	S*	95	FBERT	S
28	GEOFR	S	62	QXZ119	S*	96	BERTINI	S
29	RADLI	F	63	PHTOINT	S	97	RANFT	S
30	EOFS	S	64	PHI	F	98	FDNP	S
31	CROSS0	S	65	PHTOD	S	99	Q60	F
32	QOFS	F	66	ELSPEC	S	100	SFBERT	S
33	ATOE	S	67	XPP	F			
34	ATOPP	S	68	XNP	F			

[a] S—subroutine module.
F—function module.
S*—subroutine module taken from LaRC-NASA mathematical library (N2-3D).
F*—function module taken from LaRC-NASA mathematical library (N2-3D).

A2. HZETRN Input Requirements

The complete program is composed of the HZETRN source code (HZEALH2O.FOR in the COSMIC library) and three input data files. In the current version, HZEALH2O.FOR requires the following input files:

1. ATOMIC.DAT
2. NUCLEAR.DAT
3. JSCCOSMC.DAT

The following is a brief description of each file and how to set up the input flags if any are required.

1. FORTRAN code HZEALH2O.FOR is set up to transport galactic cosmic ray (GCR) particles in free space (geomagnetic cutoffs are ignored) through a given thickness of the aluminum shield followed by a given depth of water. Besides the setting of array dimensions for the energy grid points and isotope fragment number, which are defined in the PARAMETER statement throughout the code as II=45 and IJ=59, respectively, the only changes to the code required for any run are in the MAIN module and subroutine MATTER. In addition the user has the option of changing the isotope table that is used to represent the transported particle fields of the GCR particles in the shield or target material in function TS.

a. In the MAIN module, the following two integer variables must be defined:

(1) IPRGCR, which specifies the extent (1, 2, or 3) of printed information, with 2 being a good choice for most calculations

(2) IYEAR, which specifies the year in the solar cycle to be used (solar maxima for the years 1958, 1970, 1981, and 1989 and solar minima for the years 1965, 1977, and 1986)

b. In subroutine MATTER, the following arrays and variables must be defined:

(1) Dimension of array XAL, which specifies the depth in the aluminum shield where dosimetric quantities are to be calculated and printed. The depth within the aluminum shield is determined by summing the elements of array XAL. For example, if XAL has a dimension of 3 and is defined in the data statement as DATA XAL/5,5,10/, the transport calculation results will be printed for the following depths of the shield material:

(a) Depth 1: XAL(1)=5 g/cm^2

(b) Depth 2: XAL(1)+XAL(2)=5+5=10 g/cm^2

(c) Depth 3: XAL(1)+XAL(2)+XAL(3)=5+5+10=20 g/cm^2

(2) Dimension of array XWAT. The discussion in paragraph 1.b.(1) also applies to the array XWAT for water.

Note that for the shield and target material the particle fields are transported and calculated by default in steps of H=1 g/cm^2 throughout the program, and the discussion in paragraphs 1.b.(1) and 1.b.(2) refers only to the depths for which data are to be printed.

(3) Variables NTOT1 and NTOT2 must be equal to the dimensions of XAL and XWAT arrays, respectively. For example, if XAL has dimension 3 and XWAT has dimension 5, then NTOT1 and NTOT2 are defined by

```
DATA NTOT1,NTOT2/3,5/
```

(4) The following physical properties of the shield and target material are included: NAT is the number of elements in the shield or target—NAT=1 for aluminum, NAT=2 for water, DN is the overall density of the shield or target in g/cm^3, ATRG is the atomic mass number of each element of the shield or target, ZTRG is the atomic charge number of each element of the shield or target, and DENSTRG is the number of atoms/g of each element of the shield or target. DENSTRG is calculated from

```
DENSTRG(I)=[N0*R(I)]/SUM[R(I)*ATRG(I)]
```

where N0 is the Avogadro number taken as 6.023E23 atoms/gram-atom, R(I) is the number of atoms/molecule, and ATRG(I) is the mass in gram/gram-atom of the Ith element in the shield or target. For a simple material like aluminum, DENSTRG becomes

DENSTRG(1)=(6.023E23*1)/(1*27.0)=2.23E22 (for Al)

For a compound material like water, DENSTRG becomes

DENSTRG(1)=(6.023E23*2)/(2*1.008+1*16.0)=6.68E22 (for H)

DENSTRG(2)=(6.023E23*1)/(2*1.008+1*16.0)=3.34E22 (for O)

Note that only 3 significant figures are retained for compatibility with the generated data files. Also, note that arrays ATRG, ZTRG, and DENSTRG currently have a dimensional limit of 5. For a more complex material with NAT>5, the dimensions of ATRG, ZTRG, and DENSTRG must be adjusted appropriately.

(5) The transport of chosen particles in the shield or target is represented by a user-provided isotope table that is defined in function TS. The arrays APRO and ZPRO in common block PROJ contain the mass and charge numbers of transported isotopes. The isotope table can be changed by choosing a different table or, if more or less than 59 isotopes are needed, by adjusting variable IJ=59 in the PARAMETER statement throughout the codes to reflect a larger or smaller isotope table.

2. ATOMIC.DAT is the energy, range, and stopping-power database for water and aluminum. For any other material, the source code will automatically generate a file called NEWRMAT.DAT during execution. This file should be appended to the ATOMIC.DAT master data file for future transport runs. Note that DENSTRG format is E12.3, which permits only three significant figures.

3. NUCLEAR.DAT is the absorption and fragmentation cross-section database for water and aluminum. For any other material, the source code will automatically generate a file called NEWNUC59.DAT during execution. This file should be appended to the NUCLEAR.DAT master data file for future transport runs. Note that DENSTRG format is E12.3, which permits only three significant figures.

4. JSCCOSMC.DAT is the environmental model database taken from references 42 and 43 for the solar maxima for the years 1958, 1970, 1981, and 1989 and solar minima for the years 1965, 1977, and 1986.

A3. Compiler Dependencies

Besides the usual compiler-dependent OPEN and REAL*8 statements, which must be checked by the HZEALH2O.FOR code user, the source code has one compiler-dependent feature in subroutine QXZ061, which must be modified if this code is to be run on a non-VAX platform. In QXZ061,

variables THIRD and SIXTH are defined in OCTAL format and must be modified to conform with a non-VAX compiler octal number format. Besides these trivial changes, the rest of the source code should run on any platform with a FORTRAN compiler.

A4. Program Execution

To provide the users of HZEALH2O.FOR with a detailed description of a typical run, the following input conditions are used to generate the sample output given in appendix B:

1. IPRGCR=2
2. IYEAR=4 (1977 solar minimum)
3. XAL(3)=5,5,10 (aluminum depths of 5, 10, and 20 g/cm^2)
4. XWAT(5)=1,1,1,1,1 (water depths of 1, 2, 3, 4, and 5 g/cm^2)

The sample output is divided into 36 blocks (A,...,Z and AA,...,JJ). Each block includes a brief description of the flow of the program and how to interpret the output.

Block A prints the values of the physical properties (mass, charge, density, etc.) of the target material, which in almost all cases is water. These quantities are used in the function RTIS. In RTIS the input data file ATOMIC.DAT is accessed to see if it contains the energy, range, and stopping power of the chosen target material. This is accomplished by comparing the supplied physical properties of the target with those available in ATOMIC.DAT. If the physical properties are the same, then the energy, range, and stopping-power arrays are loaded from ATOMIC.DAT. If ATOMIC.DAT does not have the information for the target of interest, then a host of other subroutines and functions are called to generate the appropriate energy, range, and stopping-power arrays. This new information is written into the file NEWRTIS.DAT. The user has the responsibility to append NEWRTIS.DAT to ATOMIC.DAT after the program execution for future use. The user is then informed that all appropriate arrays in RTIS are initialized, and the message RTIS IS INITIALIZED is printed.

Next, the user is informed that the 1977 solar minimum is chosen as the environmental model. The program searches the input data file JSCCOSMC.DAT to load and scale the flux arrays in HZEALH2O.FOR for later transport calculations.

Then, the program reads the physical properties (same quantities as previously read in RTIS) of the shield material from subroutine MATTER. The subroutine MATTER, as discussed previously, is the only module that the user has to modify to accommodate new shield and target materials. Once the shield material information is read from MATTER, the information concerning the transported particle field absorption and fragmentation cross sections for the shield material is read from the input data file NUCLEAR.DAT. This is accomplished by calling function TS. In TS, as in RTIS, the physical properties of the aluminum shield material are compared with those available in NUCLEAR.DAT. If the physical properties are the same, then the absorption and fragmentation cross-section arrays are loaded from NUCLEAR.DAT. If NUCLEAR.DAT does not have the information for the shield material of interest, then a host of other subroutines and functions are called to generate the appropriate cross-section arrays. This information is written into the file NEWNUC59.DAT. As in RTIS, the user has the responsibility to append NEWNUC59.DAT to NUCLEAR.DAT for future runs. The user is then informed that all appropriate cross-section arrays are initialized and the message MATERIAL FOR TS 1 FOUND ON NUCLEAR.DAT FILE is printed.

The physical properties of the shield material are used in function RMAT to load energy, range, and stopping-power arrays for the shield material from input data file ATOMIC.DAT. RMAT is identical to RTIS, except that it is designed to calculate or load the energy, range, and stopping-power arrays for shield material rather than for target material. As in RTIS, if the ATOMIC.DAT does not have the information for the shield material, a new file called NEWRMAT.DAT is generated which will have to be

appended to ATOMIC.DAT for future runs. Finally, when all appropriate arrays in RMAT are initialized, the message RMAT IS INITIALIZED is printed.

Block B contains the depth values of the shield material in g/cm^2 at which transported quantities are printed. The first depth value corresponds to the free-space boundary or X=0 g/cm^2. The quantities for the transported particles are atomic mass, atomic charge, integral flux for a given isotope in particles/cm^2-yr, dose in cGy, and dose equivalent in cSv according to the International Commission on Radiological Protection ICRP-26 and ICRP-60 guidelines are printed for charge Z=0 to Z=28. Note that dose and dose equivalent can be easily converted to engineering units by the following:

$$1 \text{ rad} = 1 \text{ centiGray (cGy)} = 0.01 \text{ Gy}$$

$$1 \text{ rem} = 1 \text{ centiSievert (cSv)} = 0.01 \text{ Sv}$$

Then, the minimum and maximum energy, *A* MeV, and range, g/cm^2, that were used to calculate the previous flux quantities are printed.

Block C prints the cumulative integral flux and dosimetric values at the depths of the shield material that correspond to the same depths as block B. The cumulative transported quantities are grouped into six charge groups of Z=0, Z=1, Z=2, 3≤Z≤10, 11≤Z≤20, and 21≤Z≤28. The units for integral flux, dose, and dose equivalents are the same as for block B.

Then, the total cumulative integral flux and dosimetric values for all six charge groups are printed.

Block D contains the depth values of shield material at which transport quantities are calculated and stored. The depth increment is set by default to H=1 g/cm^2. The printing of depth values stops when the first depth of the shield material as defined in subroutine MATTER is reached.

Blocks E, H, and K are similar to block B.

Blocks F, I, and L are similar to block C.

Blocks G and J are similar to block D. At this stage, calculations for the aluminum shield material are complete and the program begins to read information for the target material.

Block M prints the values of the physical properties (mass, charge, density, etc.) of the target material, as defined in subroutine MATTER. These quantities are used in function RMAT. As described in the second half of block A, these physical properties are compared with those available in the input data file ATOMIC.DAT, and the appropriate arrays for energy, range, and stopping power are either loaded from ATOMIC.DAT or calculated and stored in NEWRMAT.DAT. As in block A, the user has the responsibility to append NEWRMAT.DAT to ATOMIC.DAT after the program execution for future use.

Blocks N, Q, S, U, W, and Y are similar to block B.

Blocks O, R, T, V, X, and Z are similar to block C.

Block P is similar to block D. At this stage, calculations for the water target material are complete and the program begins the stopping-power calculations for the shield and target materials.

Block AA is the start of the printed transported quantities as a function of stopping power S=LET. It contains the depth values of the shield material in g/cm^2, at which the transported quantities are calculated. The first depth value corresponds to the free-space boundary at X=0 g/cm^2. The printed quantities for the transported particles are LET in MeV/(g/cm^2), integral flux at a given LET in particles/cm^2 yr, dose in cGy, and dose equivalent in cSv to ICRP-26 and ICRP-60 guidelines.

Blocks BB, CC, and DD are similar to block AA. The printed quantities in blocks AA, ..., DD are LET-related quantities in the shield material.

Block EE prints the transported quantities as a function of LET for the target material at a target depth of X=0 g/cm^2.

Blocks FF, GG, HH, II, and JJ are similar to block EE.

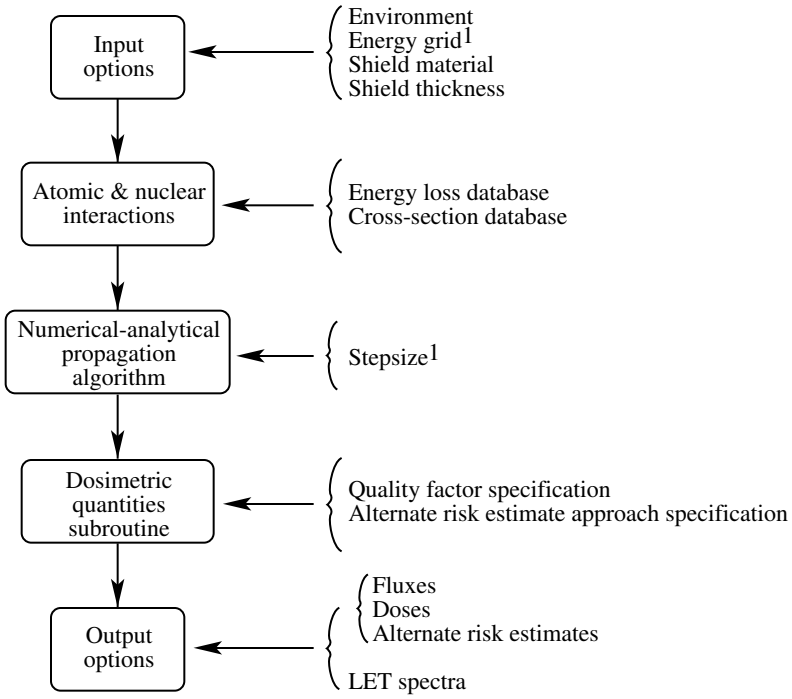

[1]Designates semiflexible inputs.

Figure A1. Computational structure of HZETRN.

References

1. Peters, B.: The Nature of Primary Cosmic Radiation. *Progress in Cosmic Ray Physics*, J. G. Wilson, ed., Interscience Publ., Inc., 1958, pp. 191–242.

2. Davis, Leverett, Jr.: On the Diffusion of Cosmic Rays in the Galaxy. *Proceedings of the Moscow Cosmic Ray Conference*, International Union of Pure and Applied Physics (Moscow), 1960, pp. 220–225.

3. Ginzburg, V. L.; and Syrovatskii, S. I. (H. S. H. Massey, transl., and D. Ter Haar, ed.): *The Origin of Cosmic Rays*. Macmillan Publ., 1964.

4. Gloeckler, G.; and Jokipii, J. R.: Physical Basis of the Transport and Composition of Cosmic Rays in the Galaxy. *Phys. Rev. Lett.*, vol. 22, no. 26, June 30, 1969, pp. 1448–1453.

5. Lezniak, J. A.: The Extension of the Concept of the Cosmic-Ray Path-Length Distribution to Nonrelativistic Energies. *Astrophys. & Space Sci.*, vol. 63, no. 2, July 1979, pp. 279–293.

6. Wilson, John W.: *Analysis of the Theory of High-Energy Ion Transport*. NASA TN D-8381, 1977.

7. Wilson, J. W.: Depth-Dose Relations for Heavy Ion Beams. *Virginia J. Sci.*, vol. 28, no. 3, 1977, pp. 136–138.

8. Wilson, John W.: *Heavy Ion Transport in the Straight Ahead Approximation*. NASA TP-2178, 1983.

9. Wilson, John W.; Townsend, L. W.; Bidasaria, H. B.; Schimmerling, Walter; Wong, Mervyn; and Howard, Jerry: ^{20}Ne Depth-Dose Relations in Water. *Health Phys.*, vol. 46, no. 5, May 1984, pp. 1101–1111.

10. Wilson, John W.; Lamkin, Stanley L.; Farhat, Hamidullah; Ganapol, Barry D.; and Townsend, Lawrence W.: *A Hierarchy of Transport Approximations for High Energy Heavy (HZE) Ions*. NASA TM-4118, 1989.

11. Wilson, John W.; Townsend, Lawrence W.; and Badavi, F. F.: A Semiempirical Nuclear Fragmentation Model. *Nucl. Instrum. & Methods Phys. Res.*, vol. B18, no. 3, Feb. 1987, pp. 225–231.

12. Wilson, John W.; and Badavi, F. F.: Methods of Galactic Heavy Ion Transport. *Radiat. Res.*, vol. 108, 1986, pp. 231–237.

13. Wilson, John W.; and Townsend, L. W.: A Benchmark for Galactic Cosmic-Ray Transport Codes. *Radiat. Res.*, vol. 114, no. 2, May 1988, pp. 201–206.

14. Curtis, S. B.; Doherty, W. R.; and Wilkinson, M. C.: *Study of Radiation Hazards to Man on Extended Near Earth Missions*. NASA CR-1469, 1969.

15. Allkofer, O. C.; and Heinrich, W.: Attenuation of Cosmic Ray Heavy Nuclei Fluxes in the Upper Atmosphere by Fragmentation. *Nucl. Phys.*, vol. B71, no. 3, Mar. 25, 1974, pp. 429–438.

16. Chatterjee, A.; Tobias, C. A.; and Lyman, J. T.: Nuclear Fragmentation in Therapeutic and Diagnostic Studies With Heavy Ions. *Spallation Nuclear Reactions and Their Applications*, B. S. P. Shen and M. Merker, eds., D. Reidel Publ. Co., 1976, pp. 169–191.

17. Letaw, John; Tsao, C. H.; and Silberberg, R.: Matrix Methods of Cosmic Ray Propagation. *Composition and Origin of Cosmic Rays*, Maurice M. Shapiro, ed., Kluwer Academic Publ., 1983, pp. 337–342.

18. Ganapol, Barry D.; Townsend, Lawrence W.; and Wilson, John W.: *Benchmark Solutions for the Galactic Ion Transport Equations: Energy and Spatially Dependent Problems*. NASA TP-2878, 1989.

19. Townsend, Lawrence W.;Ganapol, Barry D.; and Wilson, John W.: Benchmark Solutions for Heavy Ion Transport Code Validation. Abstracts of Papers for the *Thirty-Seventh Annual Meeting of the Radiation Research Society and Ninth Annual Meeting of the North American Hyperthermia Group*, Mar. 1989.

20. Schimmerling, Walter; Miller, Jack; Wong, Mervyn; Rapkin, Marwin; Howard, Jerry; Spieler, Helmut G.; and Jarret, Blair V.: The Fragmentation of 670 A MeV Neon-20 as a Function of Depth in Water. *Radiat. Res.*, vol. 120, 1989, pp. 36–71.

21. Schimmerling, Walter: Ground-Based Measurements of Galactic Cosmic Ray Fragmentation in Shielding. *Adv. Space Res.*, vol. 12, no. 2–3, 1992, pp. (2)445–(2)459.

22. Wilson, John W.; Townsend, L. W.; Lamkin, S. L.; and Ganapol, B. D.: A Closed-Form Solution to HZE Propagation. *Radiat. Res.*, vol. 122, 1990, pp. 223–228.

23. Cleghorn, T. F.; Freier, P. S.; and Waddington, C. J.: The Energy Dependence of the Fragmentation Parameters and Mean Free Paths of Cosmic-Ray Nuclei With $Z \geq 10$. *Canadian J. Phys.*, vol. 46, no. 10, May 1968, pp. S572–S577.

24. Heckman, H. H.; Greiner, D. E.; Lindstrom, P. J.; and Bieser, F. S.: Fragmentation of ^{14}N Nuclei at 29 GeV: Inclusive Isotope Spectra at 0°. *Phys. Rev. Lett.*, vol. 28, no. 14, Apr. 3, 1972, pp. 926–929.

25. Heckman, H. H.: *Heavy Ion Fragmentation Experiments at the Bevatron*. NASA CR-142589, 1975.

26. Raisbeck, G. M.; and Yiou, F.: Production Cross Sections of Be Isotopes in C and O Targets Bombarded by 2.8-GeV α Particles: Implications for Factorization. *Phys. Rev. Lett.*, vol. 35, no. 3, July 21, 1975, pp. 155–159.

27. Feshbach, H.; and Huang, K.: Fragmentation of Relativistic Heavy Ions. *Phys. Lett.*, vol. 47B, no. 4, Nov. 26, 1973, pp. 300–302.

28. Goldhaber, A. S.: Statistical Models of Fragmentation Processes. *Phys. Lett.*, vol. 53B, no. 4, Dec. 23, 1974, pp. 306–308.

29. Alsmiller, R. G., Jr.; Irving, D. C.; Kinney, W. E.; and Moran, H. S.: The Validity of the Straight-Ahead Approximation in Space Vehicle Shielding Studies. *Second Symposium on Protection Against Radiations in Space*, Arthur Reetz, Jr., ed., NASA SP-71, 1965, pp. 177–181.

30. Alsmiller, R. G., Jr.; Irving, D. C.; and Moran, H. S.: Validity of the Straightahead Approximation in Space-Vehicle Shielding Studies, Part II. *Nucl. Sci. & Eng.*, vol. 32, no. 1, Apr. 1968, pp. 56–61.

31. Curtis, S. B.; and Wilkinson, M. C.: The Heavy Particle Hazard—What Physical Data Are Needed? *Proceedings of the National Symposium on Natural and Manmade Radiation in Space*, E. A. Warman, ed., NASA TM X-2440, 1972, pp. 1007–1015.

32. Wilson, John W.; and Lamkin, Stanley L.: Perturbation Theory for Charged-Particle Transport in One Dimension. *Nucl. Sci. & Eng.*, vol. 57, no. 4, Aug. 1975, pp. 292–299.

33. Wilson, John W.; Townsend, Lawrence W.; Nealy, John E.; Chun, Sang Y.; Hong, B. S.; Buck, Warren W.; Lamkin, S. L.; Ganapol, Barry D.; Khan, Ferdous; and Cucinotta, Francis A.: *BRYNTRN: A Baryon Transport Model*. NASA TP-2887, 1989.

34. Wilson, John W.; Townsend, Lawrence W.; Ganapol, Barry; Chun, Sang Y.; and Buck, Warren W.: Charged-Particle Transport in One Dimension. *Nucl. Sci. & Eng.*, vol. 99, no. 3, July 1988, pp. 285–287.

35. Shinn, Judy L.; John, Sarah; Tripathi, Ram K.; Wilson, John W.; Townsend, Lawrence W.; and Norbury, John W.: *Fully Energy-Dependent HZETRN (A Galactic Cosmic-Ray Transport Code)*. NASA TP-3243, 1992.

36. Wilson, John W.; Townsend, Lawrence W.; and Badavi, Forooz F.: Galactic HZE Propagation Through the Earth's Atmosphere. *Radiat. Res.*, vol. 109, no. 2, Feb. 1987, pp. 173–183.

37. Shinn, Judy L.; Wilson, John W.; Weyland, Mark; and Cucinotta, Francis A.: *Improvements in Computational Accuracy of BRYNTRN (A Baryon Transport Code)*. NASA TP-3093, 1991.

38. Cucinotta, F. A.: *Extension of BRYNTRN to Monoenergetic Light Ion Beams*. NASA TP-3472, 1994.

39. Shinn, Judy L.; and Wilson, John W.: *An Efficient HZETRN (A Galactic Cosmic Ray Transport Code)*. NASA TP-3147, 1992.

40. Yakowitz, Sidney; and Szidarovszky, Ferenc: *An Introduction to Numerical Computations*, Second ed., Macmillan Publ., 1989.

41. Adams, J. H., Jr.; Silberberg, R.; and Tsao, C. H.: *Cosmic Ray Effects on Microelectronics. Part I—The Near-Earth Particle Environment*. NRL Memo. Rep. 4506—Pt. I, U.S. Navy, Aug. 1981. (Available from DTIC as AD A103 897.)

42. Badhwar, G. D.; and O'Neill, P. M.: Improved Model of Galactic Cosmic Radiation for Space Exploration Missions. *Nucl. Tracks & Radiat. Meas.*, vol. 20, no. 3, July 1992, pp. 403–410.

43. Adams, James H., Jr.: *Cosmic Ray Effects on Microelectronics*, Part IV. NRL Memo. Rep. 5901 (Revised), U.S. Navy, Dec. 31, 1987.

44. Walske, M. C.; and Bethe, H. A.: Asymptotic Formula for Stopping Power of K-Electrons. *Phys. Rev.*, vol. 83, 1951, pp. 457–458.

45. Bragg, W. H.; and Kleeman, R.: On the α Particles of Radium, and Their Loss of Range in Passing Through Various Atoms and Molecules. *Philos. Mag. & J. Sci.*, ser. 6, vol. 10, no. 57, Sept. 1905, pp. 318–340.

46. Sternheimer, R. M.: The Density Effect for the Ionization Loss in Various Materials. *Phys. Rev.*, vol. 88, no. 4, Nov. 15, 1952, pp. 851–859.

47. Armstrong, T. W.; and Alsmiller, R. G., Jr.: An Approximate Density-Effect Correction for the Ionization Loss of Charged Particles. *Nucl. Instrum. & Methods*, vol. 82, 1970, pp. 289–290.

48. Shinn, Judy L.; Farhat, Hamidullah; Badavi, Francis F.; and Wilson, John W.: *Polarization Correction for Ionization Loss in a Galactic Cosmic Ray Transport Code (HZETRN)*. NASA TM-4443, 1993.

49. Andersen, Hans Henrik; and Ziegler, James F.: *Hydrogen Stopping Powers and Ranges in all Elements*. Pergamon Press, Inc., 1977.

50. Janni, Joseph F.: Calculations of Energy Loss, Range, Pathlength, Straggling, Multiple Scattering, and the Probability of Inelastic Nuclear Collisions for 0.1- to 1000-MeV Protons. AFWL-TR-65-150, U.S. Air Force, Sept. 1966. (Available from DTIC as AD 643 837.)

51. Ziegler, J. F.: *Helium-Stopping Powers and Ranges in All Elemental Matter.* Pergamon Press, Inc., 1977.

52. Barkas, Walter H.: *Nuclear Research Emulsions. Volume 1—Techniques and Theory.* Academic Press, 1973.

53. Lindhard, J.; Scharff, M.; and Schiott, H. E.: Range Concepts and Heavy Ion Ranges (Notes on Atomic Collisions, II). *Mat.-Fys. Medd.—K. Dan. Vidensk. Selsk.*, vol. 33, no. 14, 1963, pp. 1–42.

54. Wilson, J. W.; and Kamaratos, E.: Mean Excitation Energy for Molecules of Hydrogen and Carbon. *Phys. Lett.*, vol. 85A, no. 1, Sept. 7, 1981, pp. 27–29.

55. Wilson, J. W.; Chang, C. K.; Xu, Y. J.; and Kamaratos, E.: Ionic Bond Effects on the Mean Excitation Energy for Stopping Power. *J. Appl. Phys.*, vol. 53, no. 2, Feb. 1982, pp. 828–830.

56. Wilson, J. W.; and Xu, Y. J.: Metallic Bond Effects on Mean Excitation Energies for Stopping Powers. *Phys. Lett.*, vol. 90A, no. 5, July 12, 1982, pp. 253–255.

57. Wilson, J. W.; and Townsend, L. W.: An Optical Model for Composite Nuclear Scattering. *Canadian J. Phys.*, vol. 59, no. 11, Nov. 1981, pp. 1569–1576.

58. Bowman, J. D.; Swiatecki, W. J.; and Tsang, C. F.: *Abrasion and Ablation of Heavy Ions*. LBL-2908, Univ. of California, July 1973.

59. Townsend, L. W.; Wilson, J. W.; Cucinotta, F. A.; and Norbury, J. W.: Comparison of Abrasion Model Differences in Heavy Ion Fragmentation—Optical Versus Geometric Models. *Phys. Rev. C*, vol. 34, no. 4, Oct. 1986, pp. 1491–1494.

60. Cucinotta, Francis A.; and Dubey, Rajendra R.: *Final State Interactions and Inclusive Nuclear Collisions*. NASA TP-3353, 1993.

61. Gosset, J.; Gutbrod, H. H.; Meyer, W. G.; Poskanzer, A. M.; Sandoval, A.; Stock, R.; and Westfall, G. D.: Central Collisions of Relativistic Heavy Ions. *Phys. Rev. C*, vol. 16, no. 2, Aug. 1977, pp. 629–657.

62. Hüfner, J.; Schäfer, K.; and Schürmann, B.: Abrasion-Ablation in Reactions Between Relativistic Heavy Ions. *Phys. Rev. C*, vol. 12, no. 6, Dec. 1975, pp. 1888–1898.

63. Morrissey, D. J.; Marsh, W. R.; Otto, R. J.; Loveland, W.; and Seaborg, G. T.: Target Residue Mass and Charge Distributions in Relativistic Heavy Ion Reactions. *Phys. Rev. C*, vol. 18, no. 3, Sept. 1978, pp. 1267–1274.

64. Guthrie, Miriam P.: *EVAP-4: Another Modification of a Code To Calculate Particle Evaporation From Excited Compound Nuclei*. ORNL-TM-3119, U.S. Atomic Energy Commission, Sept. 10, 1970.

65. Silberberg, R.; Tsao, C. H.; and Shapiro, M. M.: Semiempirical Cross Sections, and Applications to Nuclear Interactions of Cosmic Rays. *Spallation Nuclear Reactions and Their Applications*, B. S. P. Shen and M. Merker, eds., D. Reidel Publ. Co., 1976, pp. 49–81.

66. Silberberg, R.; Tsao, C. H.; and Letaw, John R.: Improvement of Calculations of Cross Sections and Cosmic-Ray Propagation. *Composition and Origin of Cosmic Rays*, Maurice M. Shapiro, ed., D. Reidel Publ. Co., 1983, pp. 321–336.

67. Wilson, J. W.; Shinn, J. L.; Townsend, L. W.; Tripathi, R. K.; Badavi, F. F.; and Chun, W. Y.: NUCFRG2: A Semiempirical Nuclear Fragmentation Model. *Nucl. Instrum. & Methods Phys. Res. B*, vol. 94, 1994, pp. 95–102.

68. Westfall, G. D.; Wilson, Lance W.; Lindstrom, P. J.; Crawford, H. J.; Greiner, D. E.; and Heckman, H. H.: Fragmentation of Relativistic ^{56}Fe. *Phys. Rev. C*, vol. 19, no. 4, Apr. 1979, pp. 1309–1323.

69. Wilson, John W.; Chun, Sang Y.; Badavi, Francis F.; and John, Sarah: *Coulomb Effects in Low-Energy Nuclear Fragmentation*. NASA TP-3352, 1993.

70. Rudstam, G.: Systematics of Spallation Yields. *Zeitschrift fur Naturforschung*, vol. 21a, no. 7, July 1966, pp. 1027–1041.

71. Townsend, Lawrence W.; Wilson, John W.; Norbury, John W.; and Bidasaria, Hari B.: *An Abrasion-Ablation Model Description of Galactic Heavy-Ion Fragmentation*. NASA TP-2305, 1984.

72. Townsend, L. W.; Wilson, J. W.; and Norbury, J. W.: A Simplified Optical Model Description of Heavy Ion Fragmentation. *Canadian J. Phys.*, vol. 63, no. 2, Feb. 1985, pp. 135–138.

73. Norbury, John W.; and Townsend, Lawrence W.: *Electromagnetic Dissociation Effects in Galactic Heavy-Ion Fragmentation*. NASA TP-2527, 1986.

74. Townsend, Lawrence W.; Wilson, John W.; Tripathi, Ram K.; Norbury, John W.; Badavi, Francis F.; and Khan, Ferdous: *HZEFRG1: An Energy-Dependent Semiempirical Nuclear Fragmentation Model*. NASA TP-3310, 1993.

75. Wilson, John W.; Chun, Sang Y.; Badavi, Forooz F.; Townsend, Lawrence W.; and Lamkin, Stanley L.: *HZETRN: A Heavy Ion/Nucleon Transport Code for Space Radiations*. NASA TP-3146, 1991.

76. Bertulani, Carlos A.; and Baur, Gerhard: Electromagnetic Processes in Relativistic Heavy Ion Collisions. *Phys. Rep.*, vol. 163, nos. 5 & 6, June 1988, pp. 299–408.

77. Aleixo, A. N. F.; and Bertulani, C. A.: Coulomb Excitation in Intermediate-Energy Collisions. *Nucl. Phys.*, vol. A505, no. 2, Dec. 11, 1989, pp. 448–470.

78. Kim, A.; Wilson, J. W.; Thibeault, S. A.; Nealy, J. E.; Badavi, F. F.; and Kiefer, R. L.: *Galactic Cosmic Radiation Shield Performance Studies*. NASA TP-3473, 1994.

79. Kidd, J. M.; Lindstrom, P. J.; Crawford, H. J.; and Woods, G.: Fragmentation of Carbon Ions at 250 MeV/Nucleon. *Phys. Rev. C*, vol. 37, no. 6, June 1988, pp. 2613–2623.

80. Webber, W. R.; Kish, J. C.; and Schrier, D. A.: Individual Isotopic Fragmentation Cross Sections of Relativistic Nuclei in Hydrogen, Helium, and Carbon Targets. *Phys. Rev. C*, vol. 41, no. 2, Feb. 1990, pp. 547–565.

81. Olson, D. L.; Berman, B. L.; Greiner, D. E.; Heckman, H. H.; Lindstrom, P. J.; and Crawford, H. J.: Factorization of Fragment-Production Cross Sections in Relativistic Heavy-Ion Collisions. *Phys. Rev. C*, vol. 28, no. 4, Oct. 1983, pp. 1602–1613.

82. Lefort, Marc: Mass Distribution in Dissipative Reactions—The Frontier Between Fusion and Deep Inelastic Transfers. *Deep-Inelastic and Fusion Reactions With Heavy Ions*, W. von Oertzen, ed., *Lecture Notes in Physics*, Springer-Verlag, vol. 117, 1980, pp. 25–42.

83. Cummings, J. R.; Binns, W. R.; Garrard, T. L.; Israel, M. H.; Klarmann, J.; Stone, E. C.; and Waddington, C. J.: Determination of the Cross Sections for the Production of Fragments From Relativistic Nucleus-Nucleus Interactions. I. Measurements. *Phys. Rev. C*, third ser., vol. 42, no. 6, Dec. 1990, pp. 2508–2529.

84. Westfall, G. D.; Wilson, Lance W.; Lindstrom, P. J.; Crawford, H. J.; Greiner, D. E.; and Heckman, H. H.: Fragmentation of Relativistic ^{56}Fe. *Phys. Rev. C*, vol. 19, no. 4, Apr. 1979, pp. 1309–1323.

85. Wilson, John W.: Environmental Geophysics and SPS Shielding. Workshop on the Radiation Environment of the Satellite Power System, Walter Schimmerling and Stanley B. Curtis, eds., LBL-8581 (Contract W-7405-ENG-48), Univ. of California, Sept. 15, 1978, pp. 33–116.

86. Alsmiller, R. G., Jr.; and Scott, W. W.: *Comparisons of Results Obtained With Several Proton Penetration Codes*, Part 2. NASA CR-95141, 1968.

87. Alsmiller, R. G., Jr.; and Scott, W. W.: *Comparisons of Results With Several Proton Penetration Codes*. NASA CR-88880, 1967.

88. Nealy, John E.; Simonsen, Lisa C.; Sauer, Herbert H.; Wilson, John W.; and Townsend, Lawrence W.: *Space Radiation Dose Analysis for Solar Flare of August 1989*. NASA TM-4229, 1990.

89. King, Joseph H.: Solar Proton Fluences for 1977–1983 Space Missions. *J. Spacecr. & Rockets*, vol. 11, no. 6, June 1974, pp. 401–408.

90. Benton, E. V.; Henke, R. P.; and Peterson, D. D.: Plastic Nuclear Track Detector Measurements of High-LET Particle Radiation on Apollo, Skylab and ASTP Space Missions. *Nucl. Track Detect.*, vol. 1, no. 1, 1977, pp. 27–32.

91. Kinney, W. E.: *The Nucleon Transport Code, NTC*. ORNL-3610, U.S. Atomic Energy Commission, Aug. 1964.

92. Recommendations of the International Commission on Radiological Protection. ICRP Publ. 26, Pergamon Press, Inc., 1987.

93. Recommendations of the International Commission on Radiological Protection. ICRP Publ. 60, Pergamon Press, Inc., 1964.

94. Townsend, Lawrence W.; Wilson, John W.; and Nealy, John E.: Space Radiation Shielding Strategies and Requirements for Deep Space Missions. SAE Tech. Paper Ser. 891433, July 1989.

95. Townsend, L. W.; and Wilson, J. W.: An Evaluation of Energy-Independent Heavy Ion Transport Coefficient Approximations. *Health Phys.*, vol. 54, no. 4, Apr. 1988, pp. 409–412.

96. Wilson, J. W.; Kim, M.; Schimmerling, W.; Badavi, F. F.; Thibeault, S. A.; Cucinotta, F. A.; Shinn, J. L.; and Kiefer, R.: Issues in Space Radiation Protection: Galactic Cosmic Rays. *Health Phys*., vol. 68, no. 1, 1995, pp. 50–58.

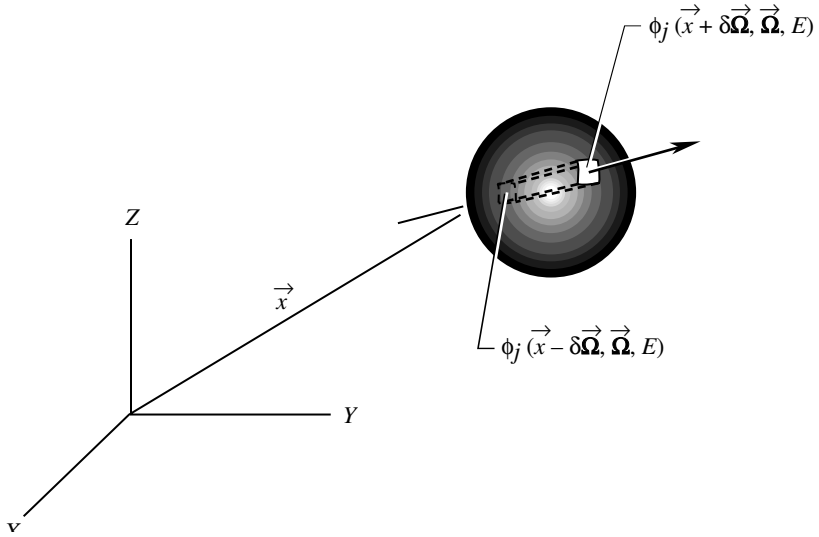

Figure 1. Transport of particles through spherical region.

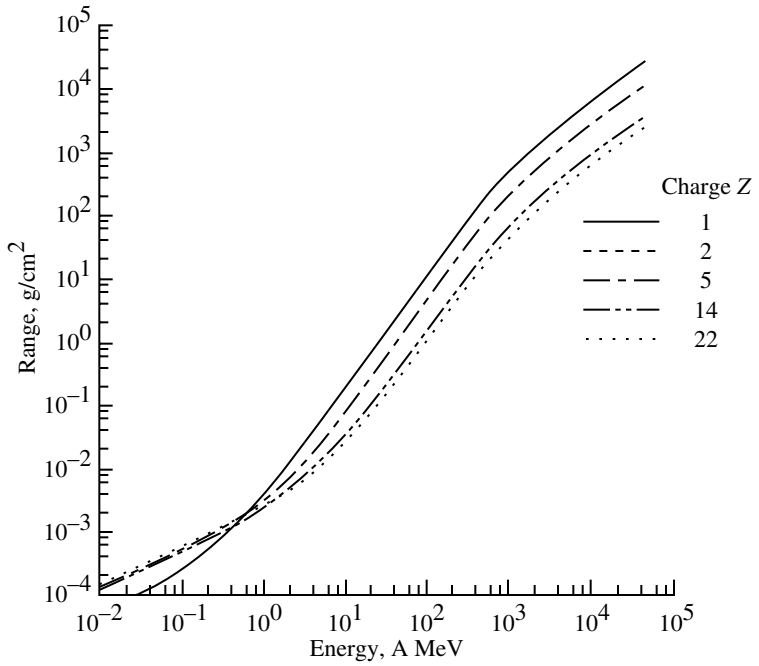

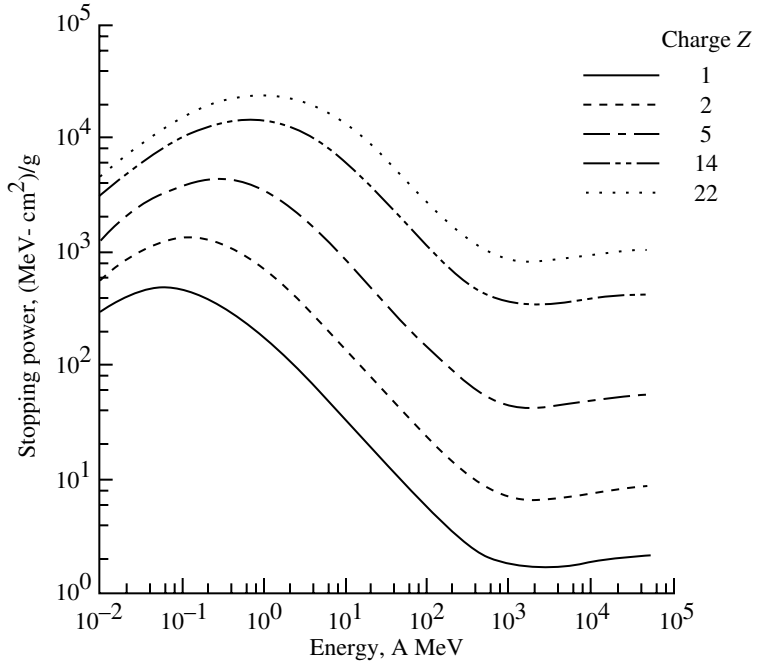

(a) Range and stopping power in aluminum.

Figure 2. Linear energy transfer (LET).

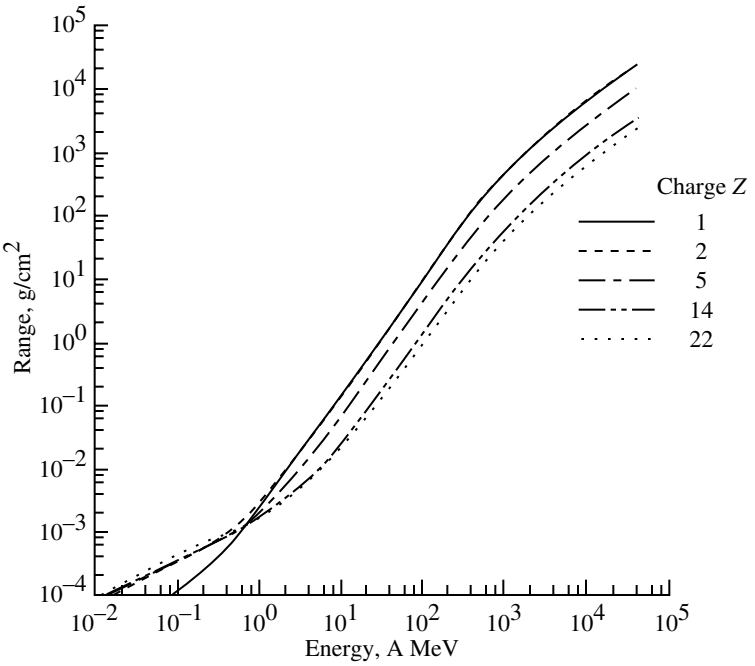

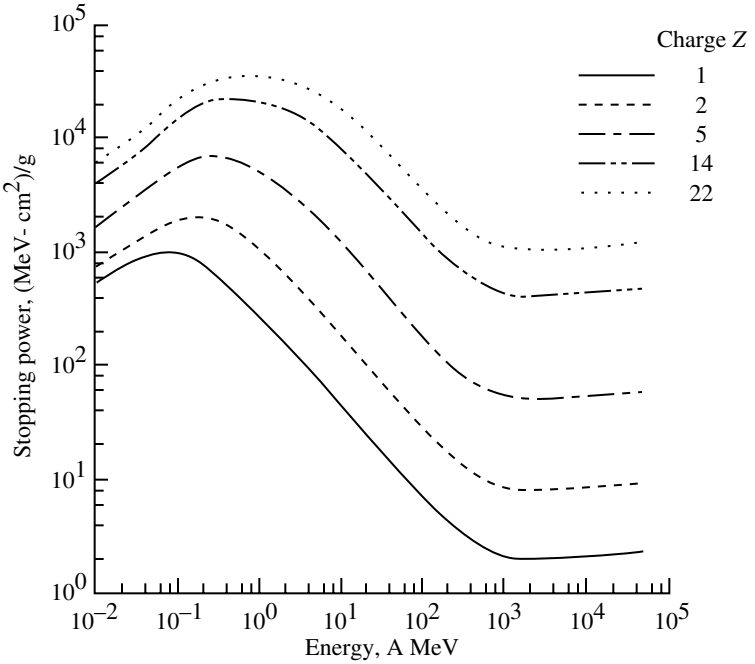

(b) Range and stopping power in water.

Figure 2. Continued.

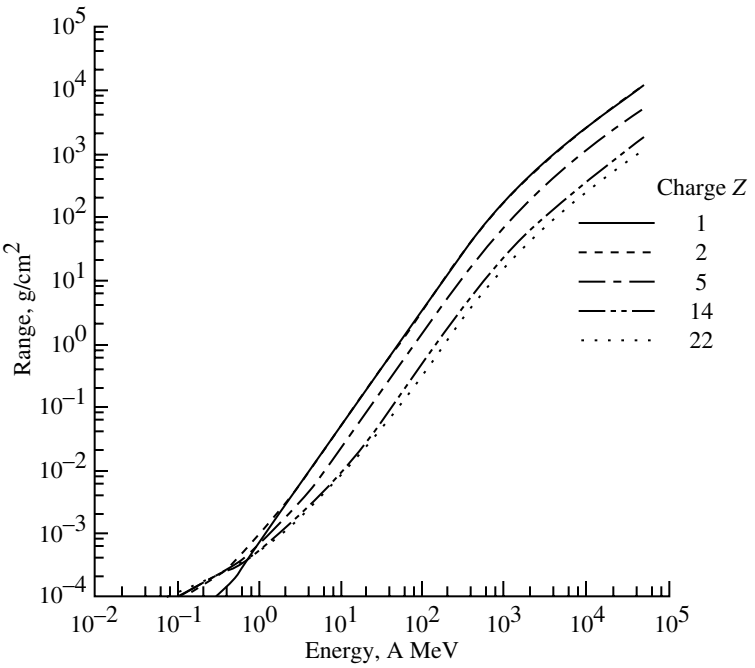

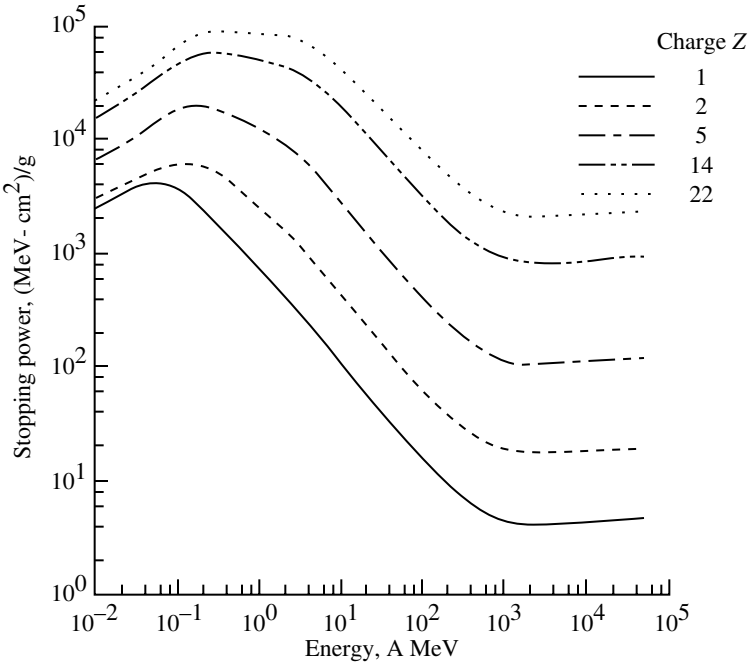

(c) Range and stopping power in liquid hydrogen.

Figure 2. Concluded.

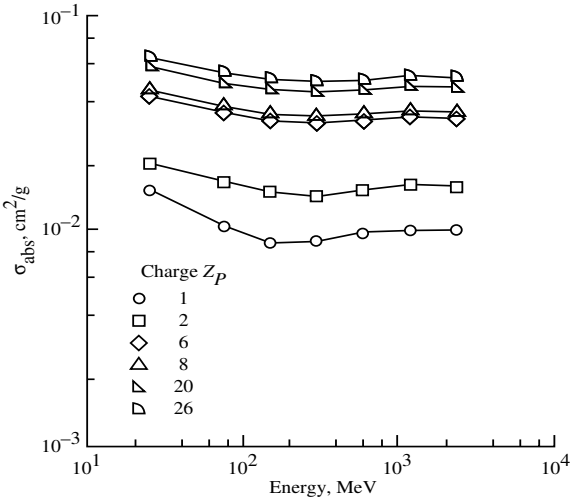

(a) Aluminum target.

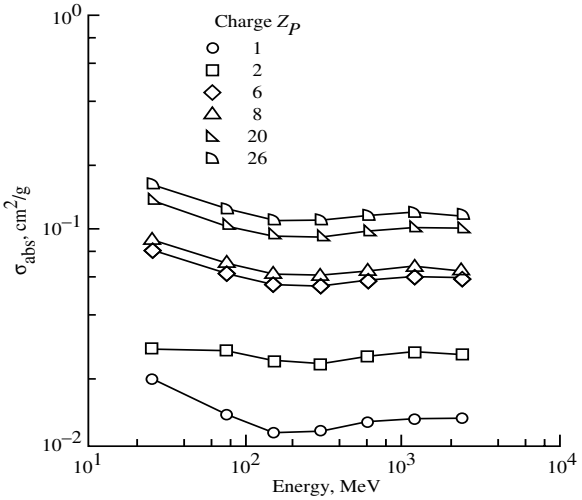

(b) Water target.

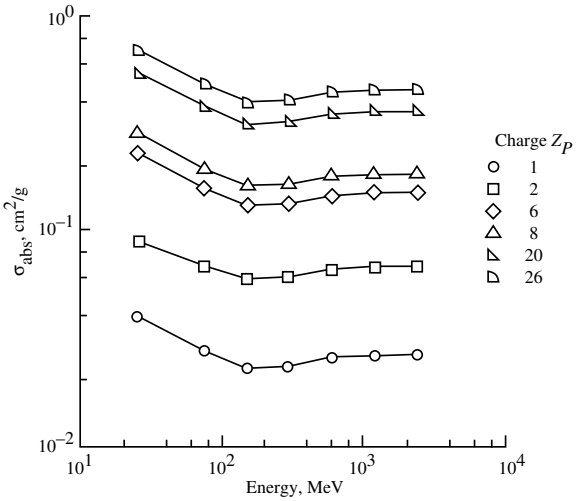

(c) Liquid hydrogen target.

Figure 3. Absorption cross section σ_{abs}.

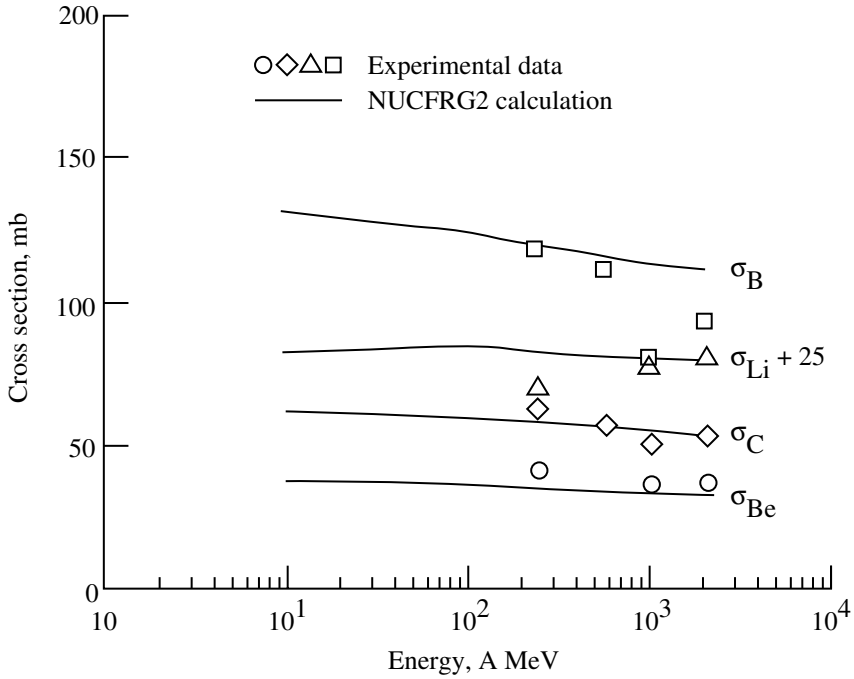

Figure 4. Charge-removal cross sections for carbon on carbon.

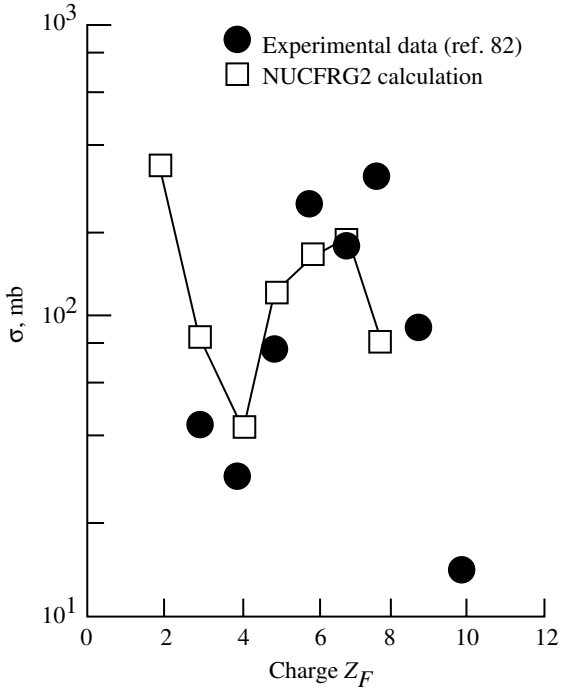

Figure 5. Charge-removal cross sections for 11.7*A*-MeV oxygen projectile on molybdenum target.

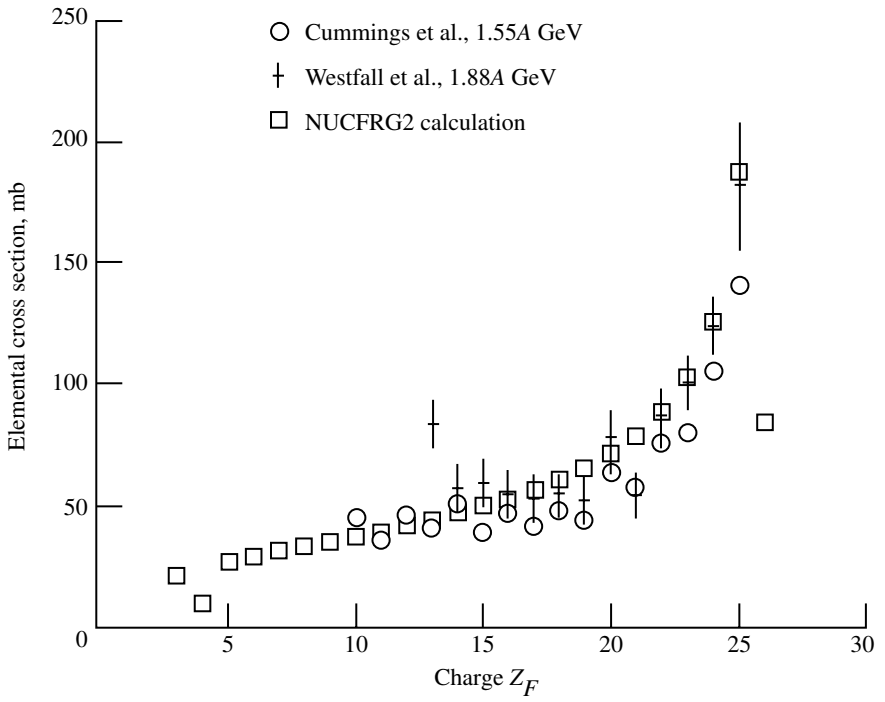

(a) Carbon target.

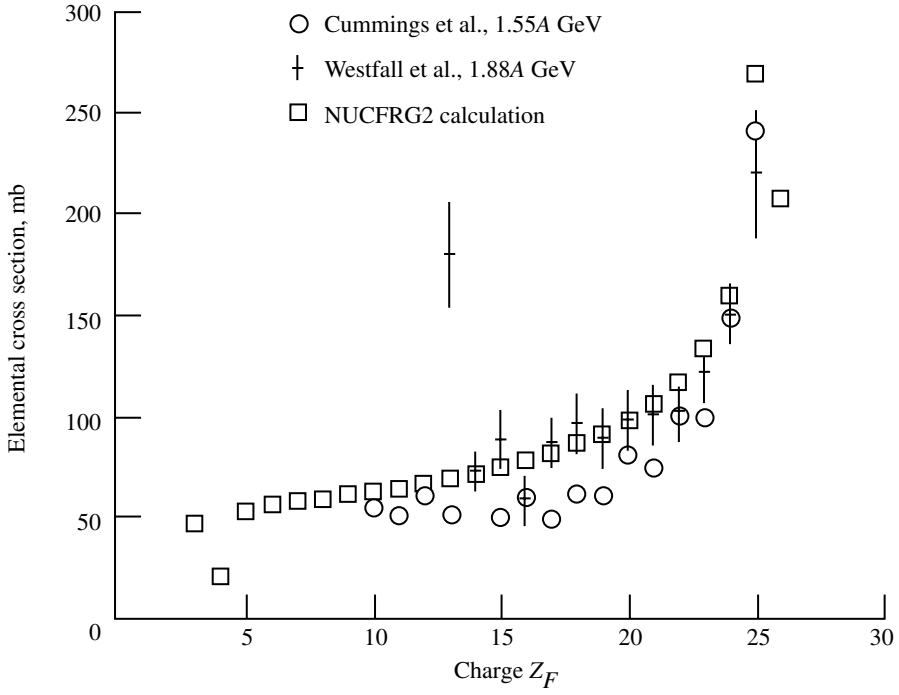

(b) Copper target.

Figure 6. Charge-removal cross sections for 1.88*A*-GeV iron projectile.

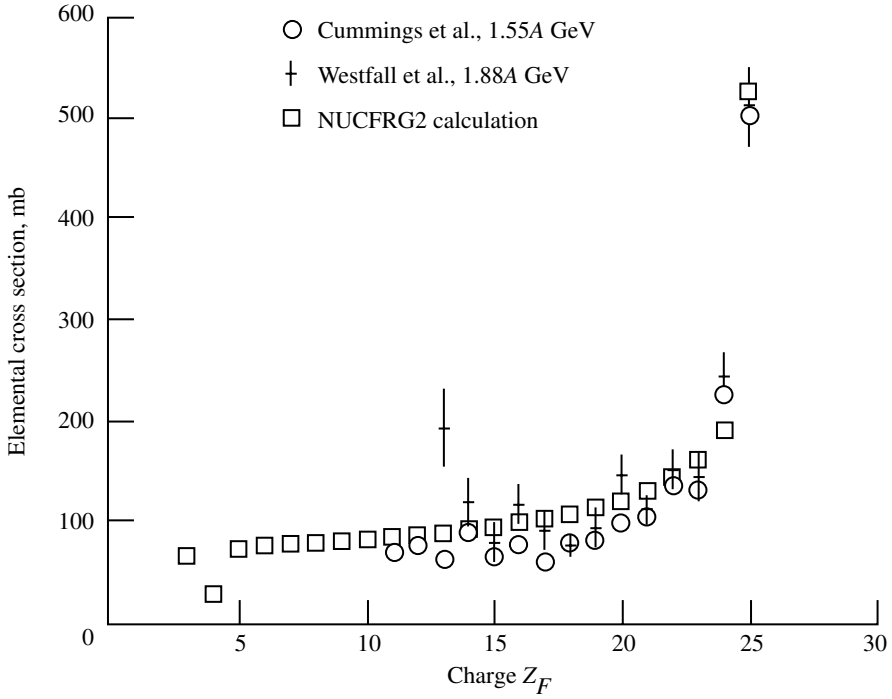

(c) Lead target.

Figure 6. Concluded.

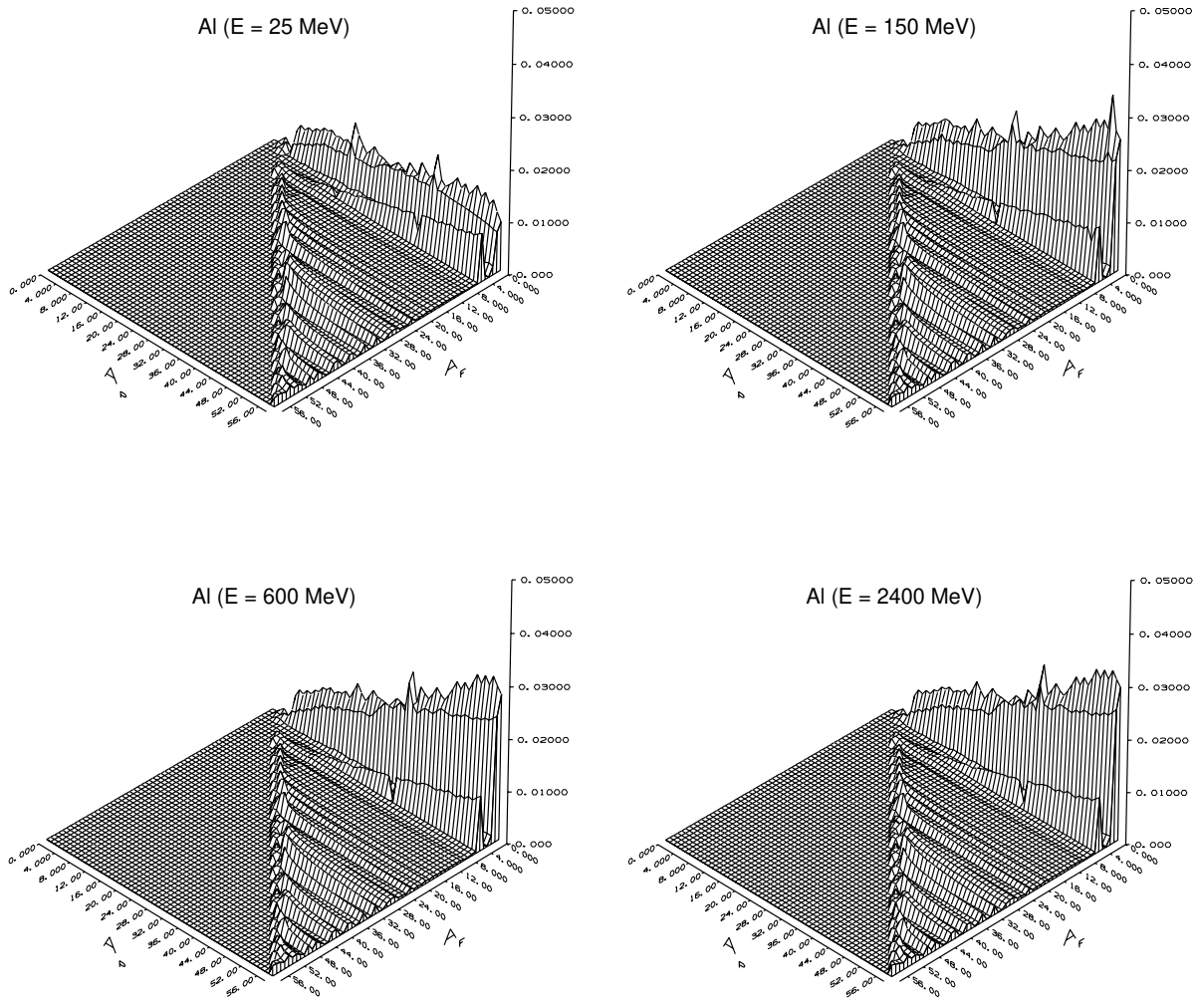

(a) Four energy levels in aluminum.

Figure 7. Fragmentation cross sections.

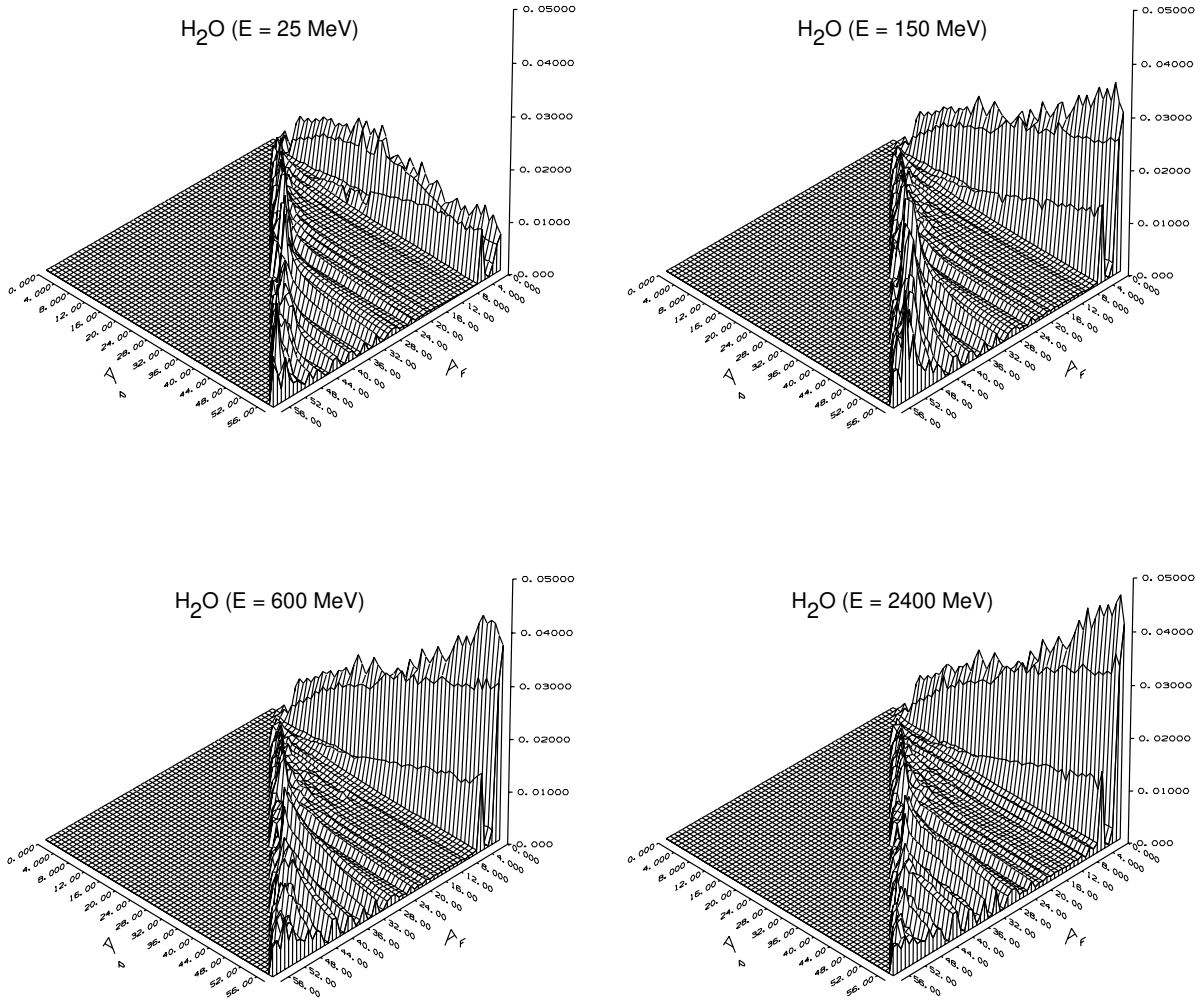

(b) Four energy levels in water.

Figure 7. Continued.

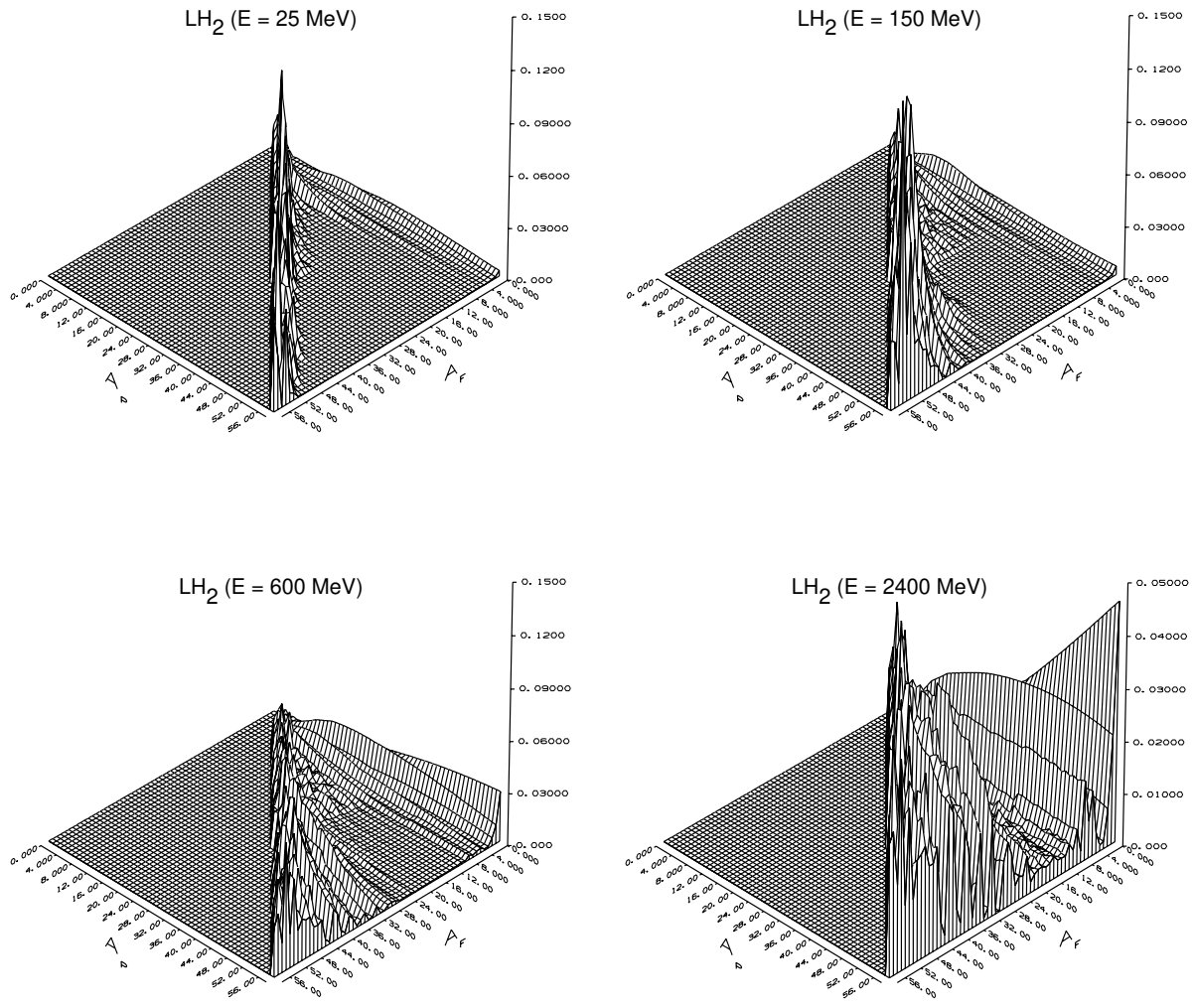

(c) Four energy levels in liquid hydrogen.

Figure 7. Concluded.

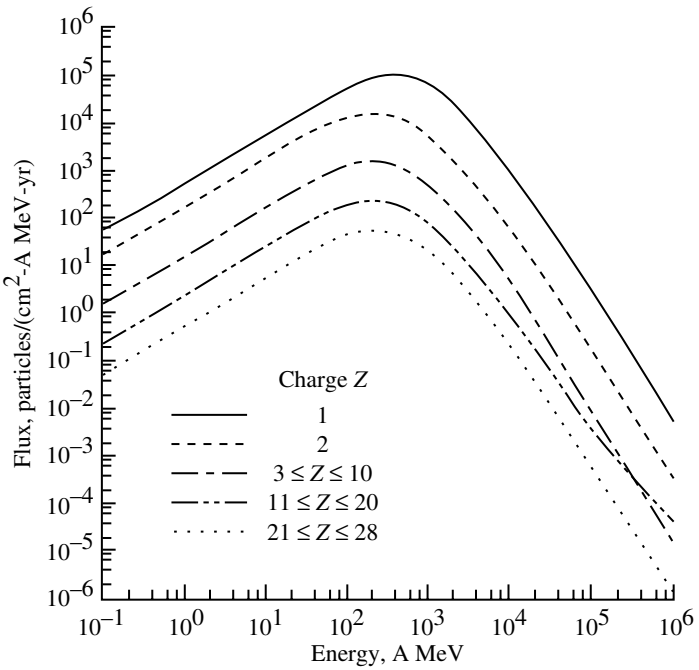

(a) GCR ion flux for 1977 solar minimum.

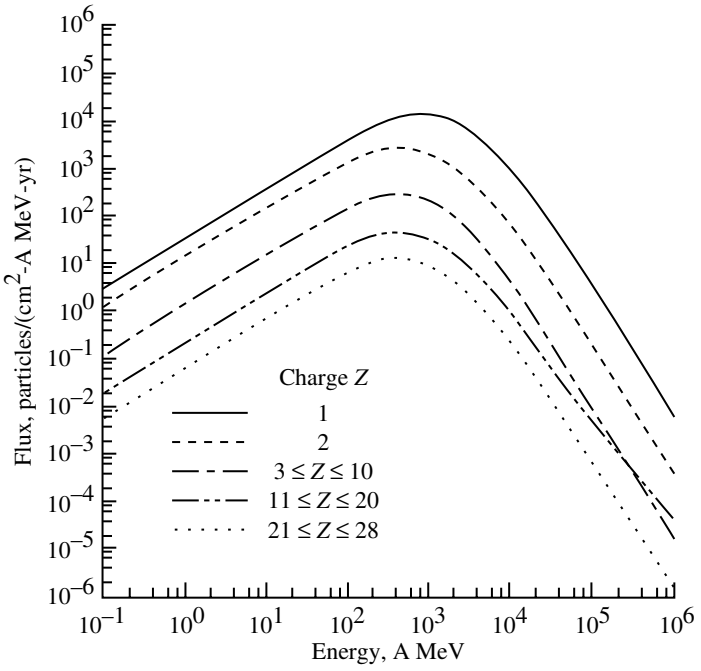

(b) GCR ion flux for 1981 solar maximum.

Figure 8. Differential fluence spectra.

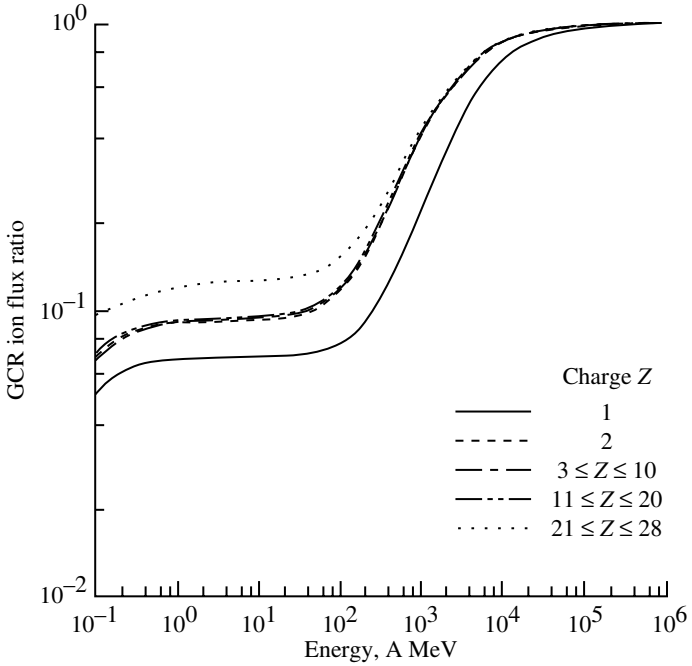

Figure 9. GCR ion flux ratio of 1981 solar maximum to 1977 solar minimum.

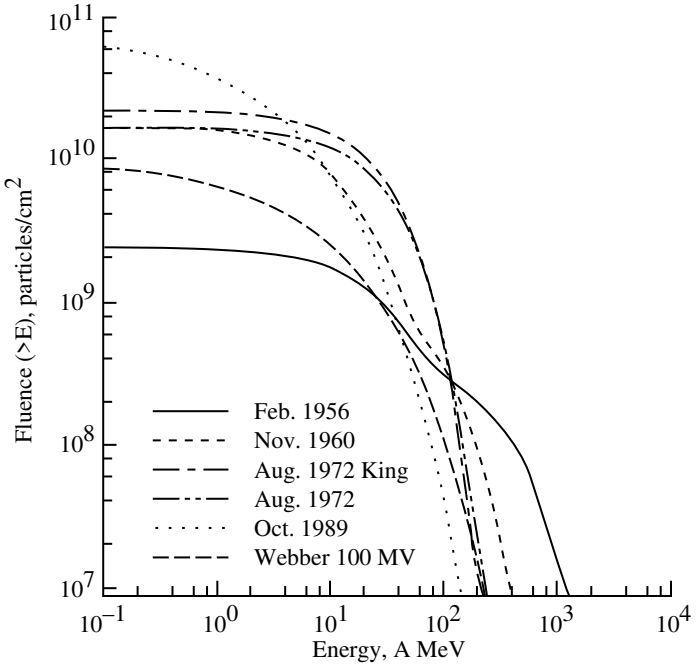

Figure 10. Integral fluence spectra of important solar particle events.

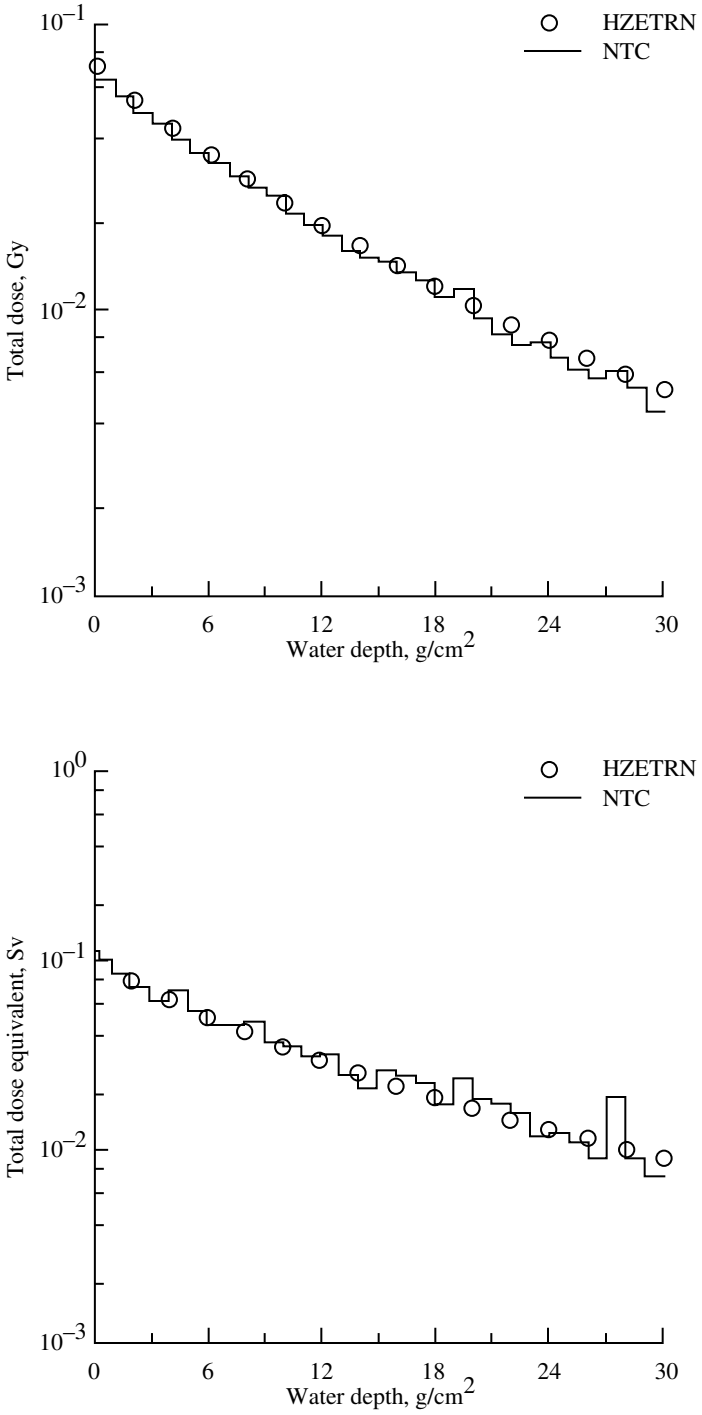

(a) Aluminum shield on water. 20 g/cm^2 Al; 30 g/cm^2 water.

Figure 11. Total dose and total dose equivalent.

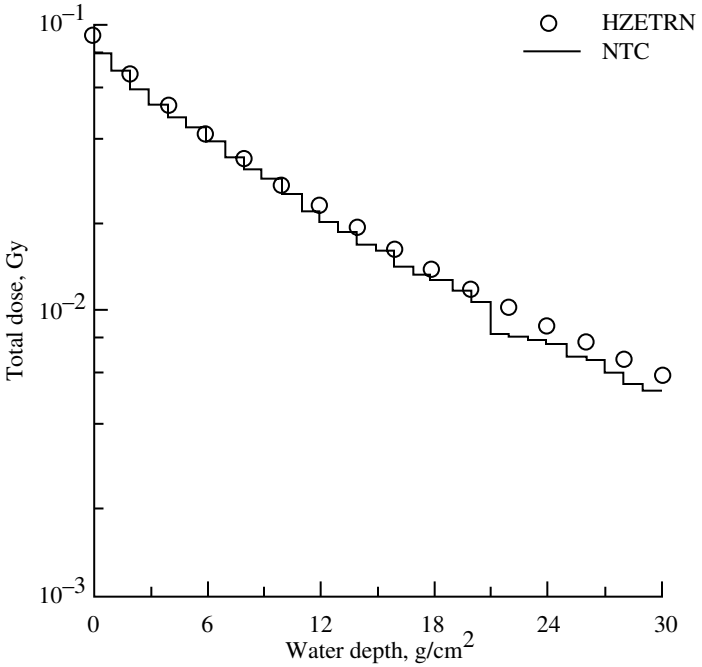

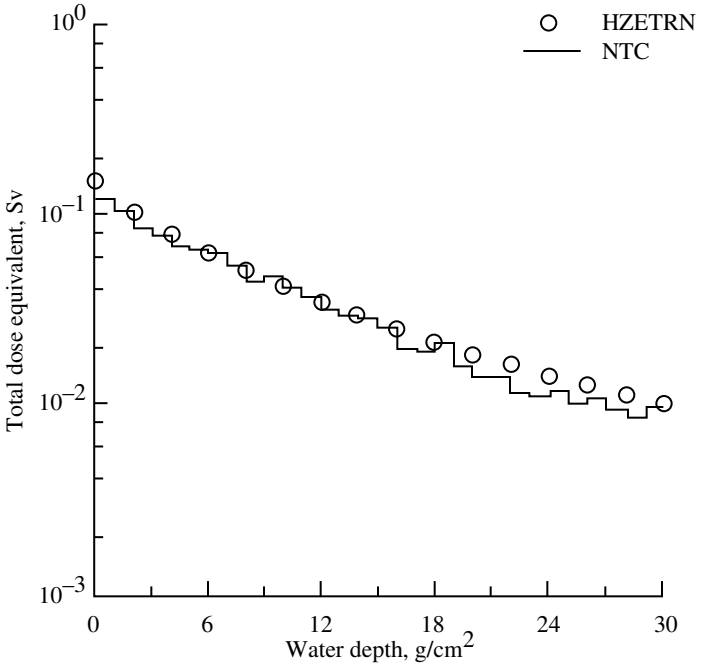

(b) Iron shield on water. 20 g/cm^2 Fe; 30 g/cm^2 water.

Figure 11. Concluded.

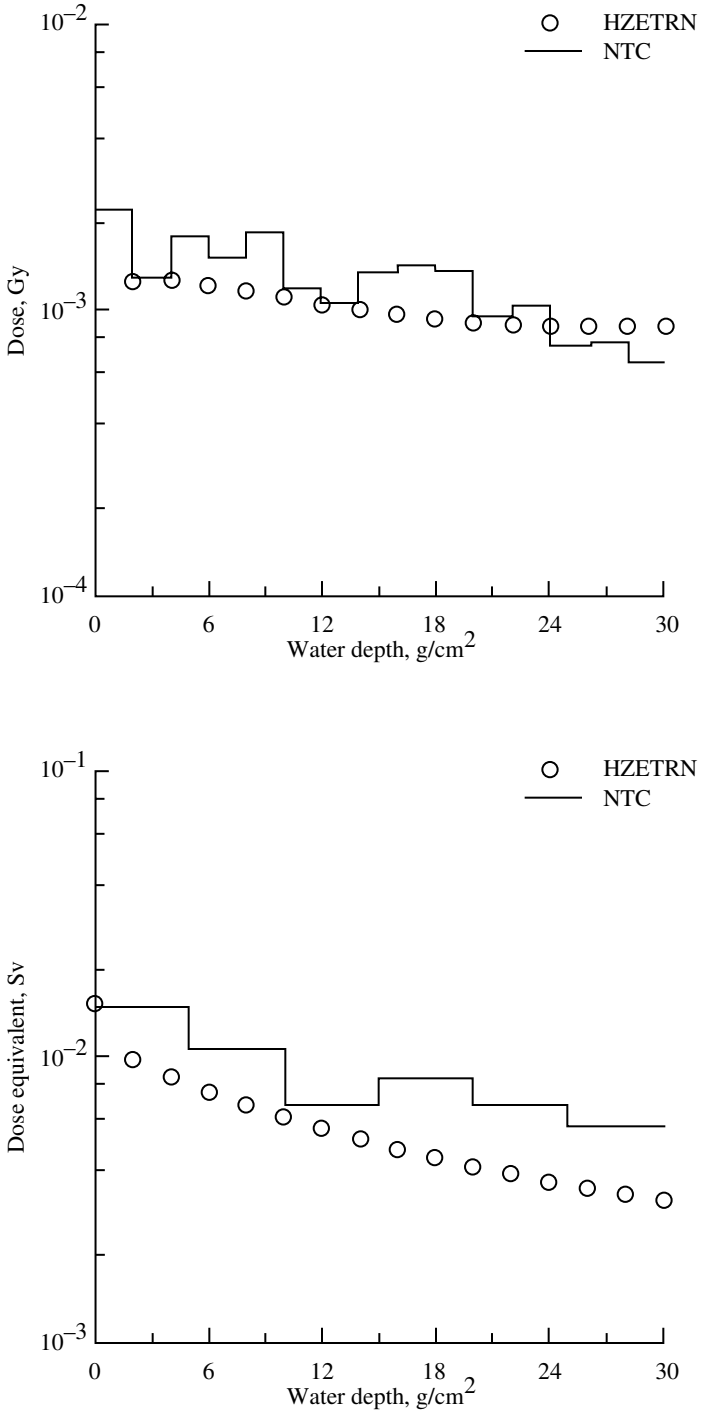

(a) Aluminum shield on water. 20 g/cm^2 Al; 30 g/cm^2 water.

Figure 12. Secondary neutron dose and dose equivalent.

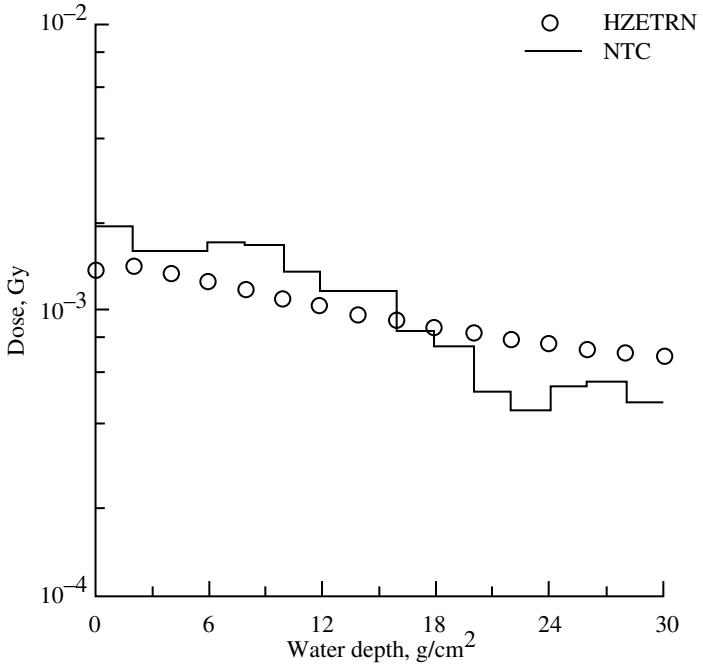

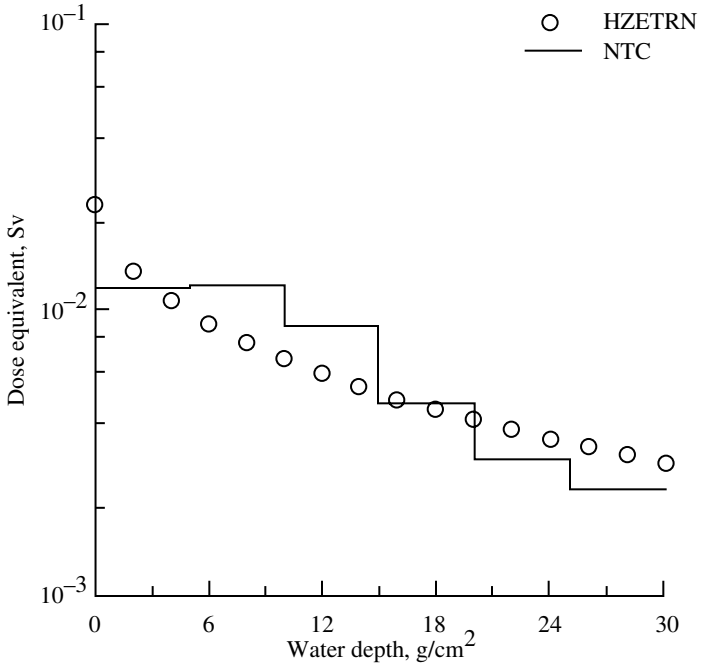

(b) Iron shield on water. 20 g/cm^2 Fe; 30 g/cm^2 water.

Figure 12. Concluded.

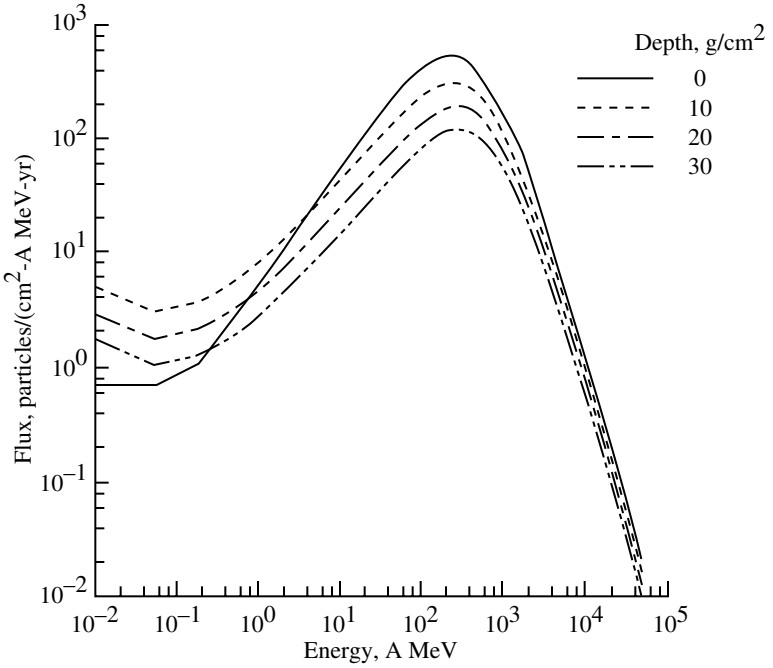

(a) 1977 solar minimum.

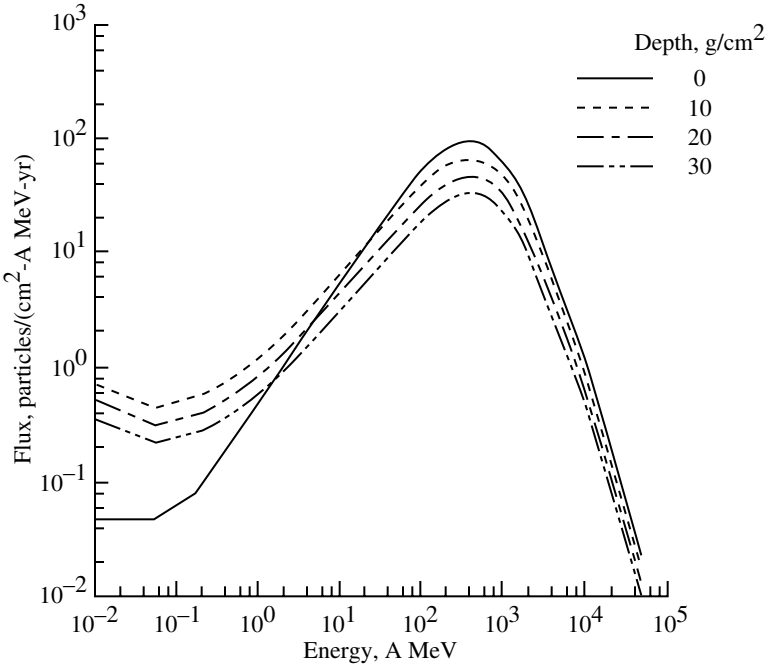

(b) 1981 solar maximum.

Figure 13. GCR energy flux for carbon ion in aluminum.

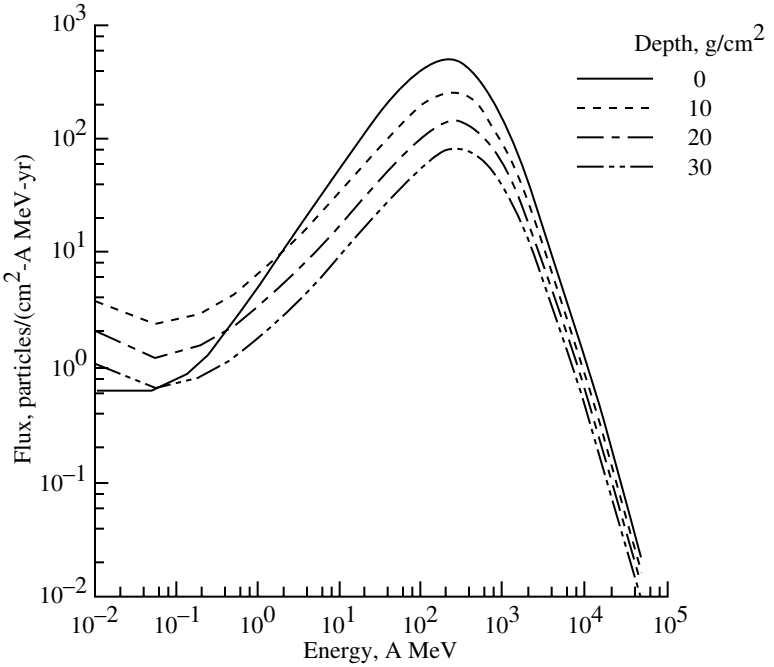

(a) 1977 solar minimum.

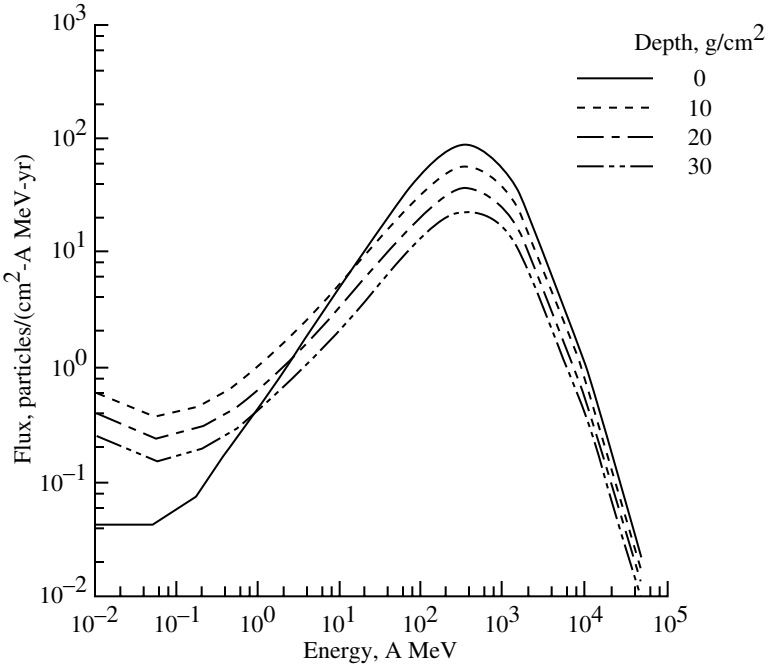

(b) 1981 solar maximum.

Figure 14. GCR energy flux for oxygen ion in aluminum.

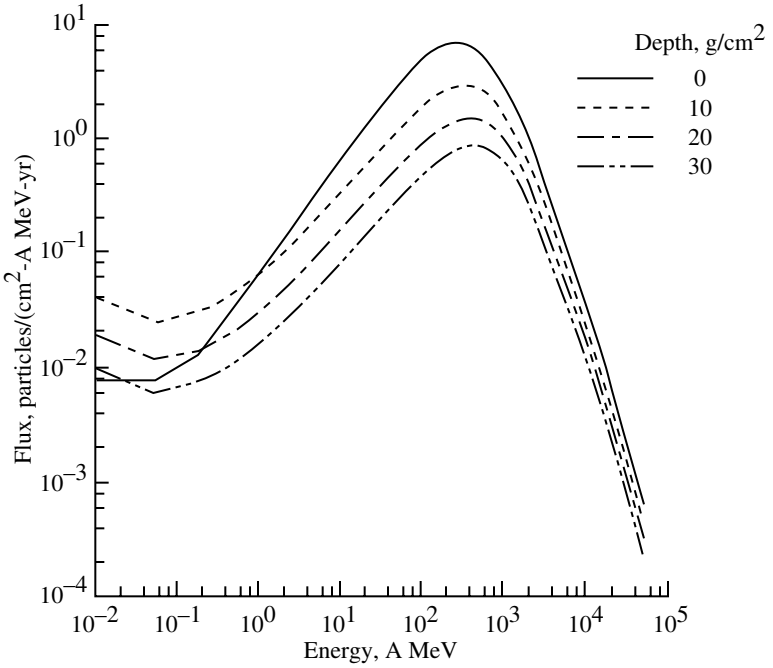

(a) 1977 solar minimum.

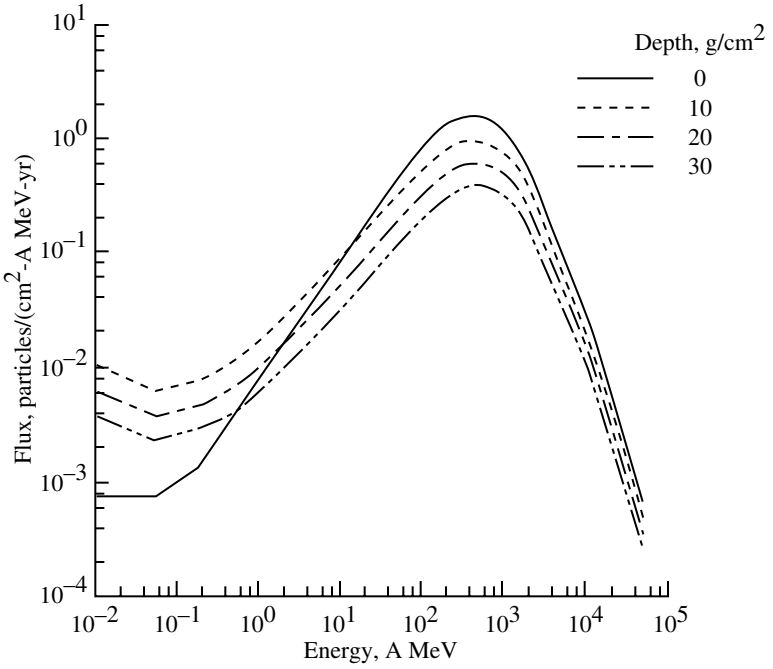

(b) 1981 solar maximum.

Figure 15. GCR energy flux for calcium ion in aluminum.

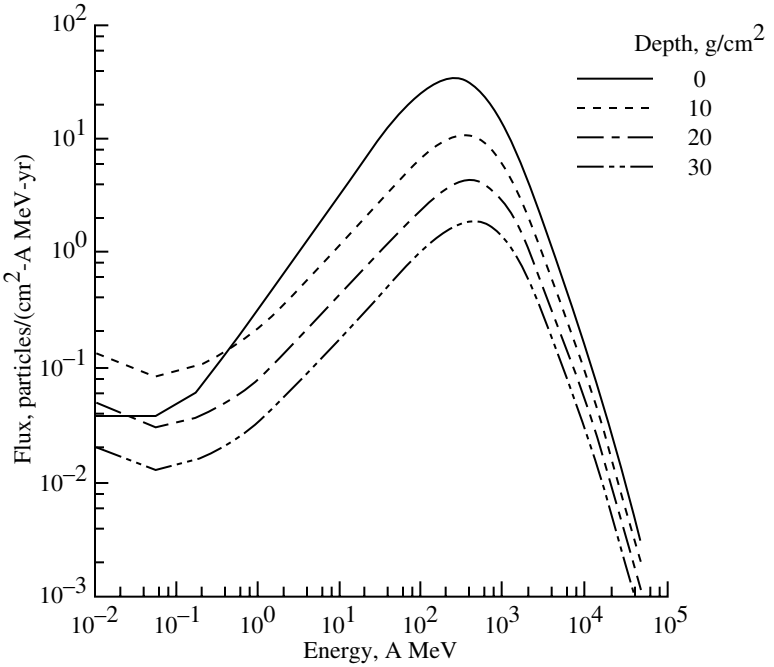

(a) 1977 solar minimum.

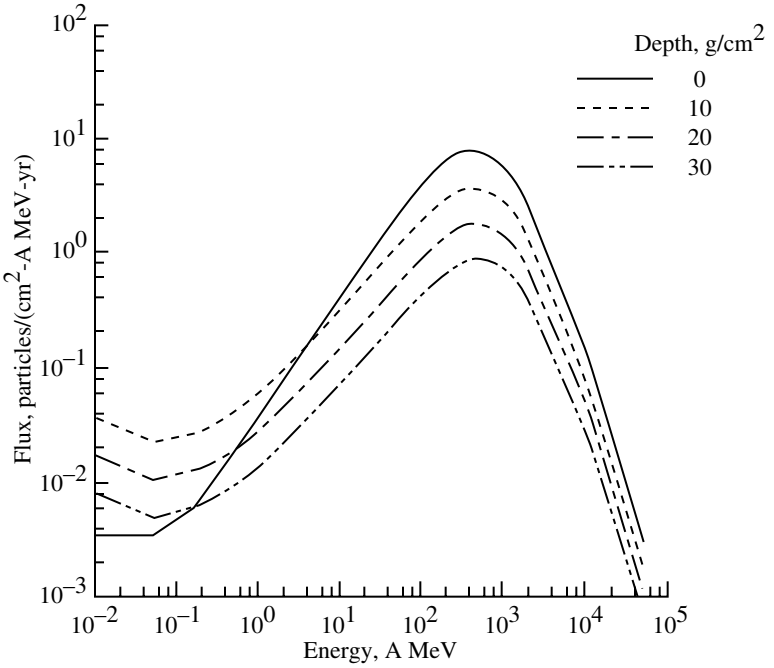

(b) 1981 solar maximum.

Figure 16. GCR energy flux for iron ion in aluminum.

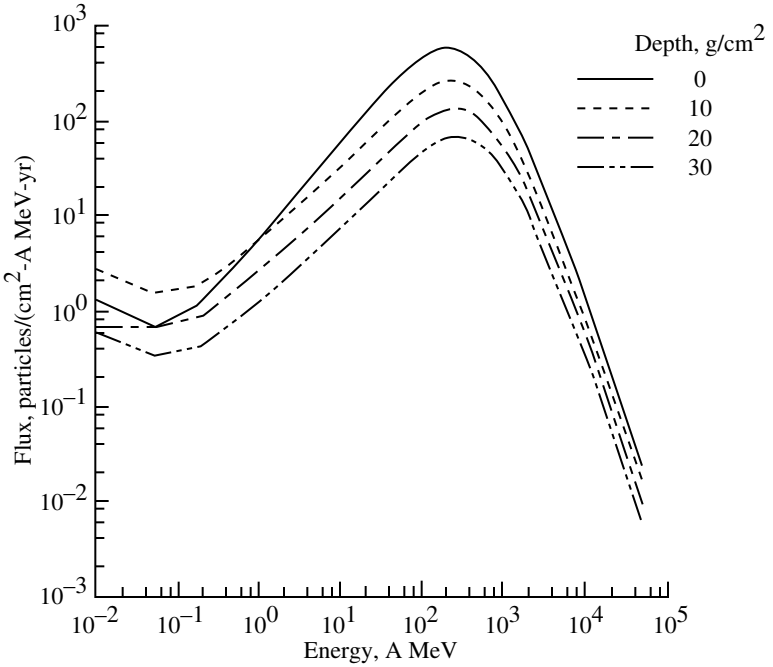

(a) 1977 solar minimum.

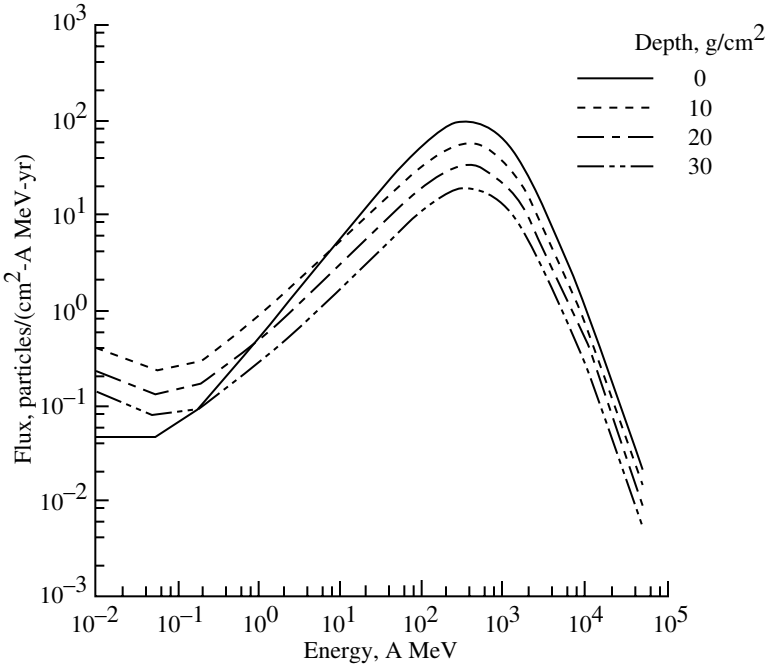

(b) 1981 solar maximum.

Figure 17. GCR energy flux for carbon ion in water.

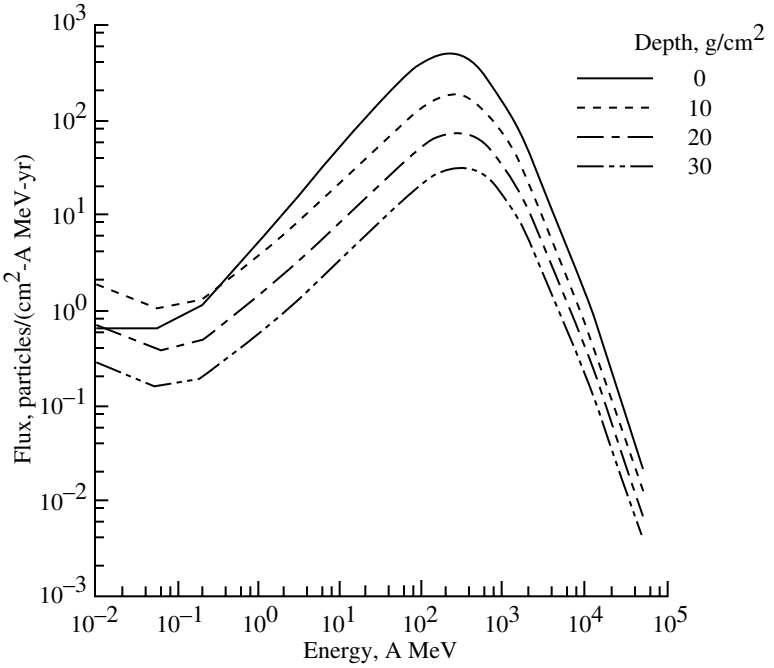

(a) 1977 solar minimum.

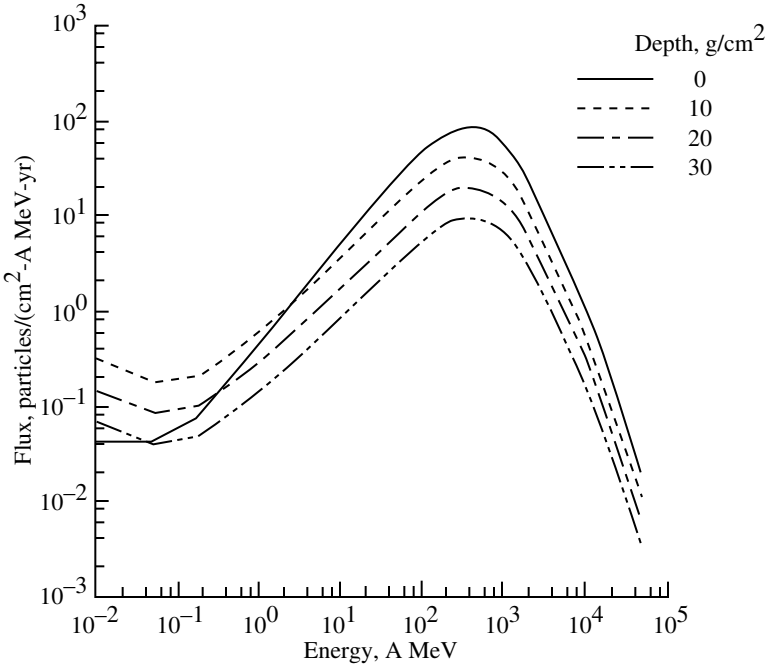

(b) 1981 solar maximum.

Figure 18. GCR energy flux for oxygen ion in water.

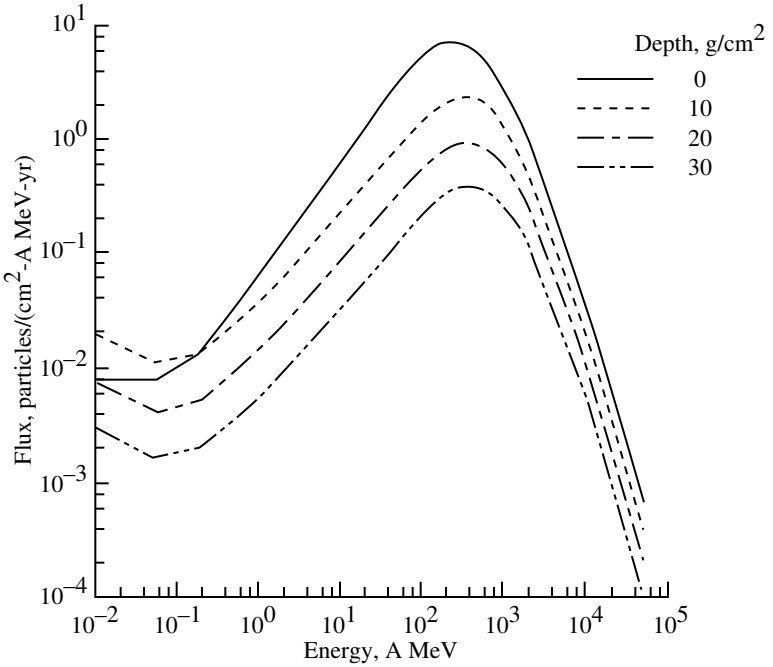

(a) 1977 solar minimum.

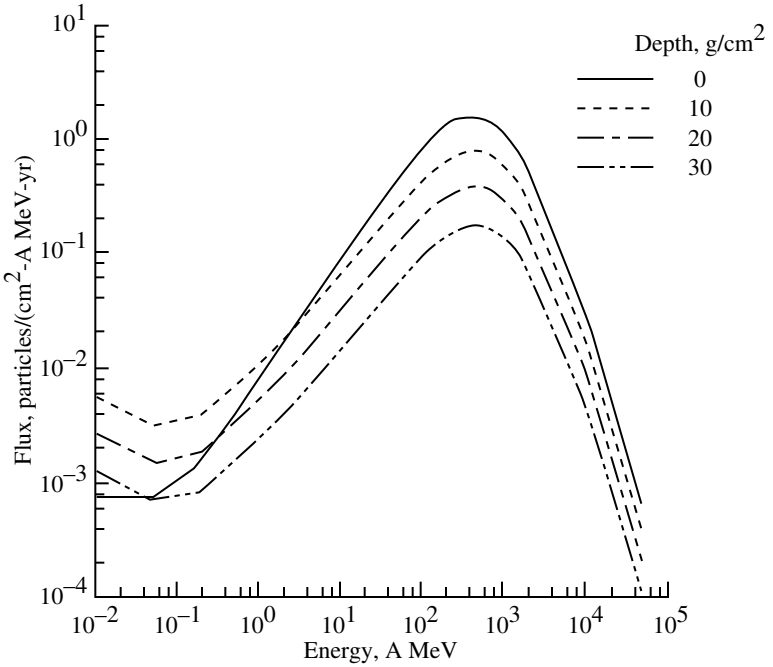

(b) 1981 solar maximum.

Figure 19. GCR energy flux for calcium ion in water.

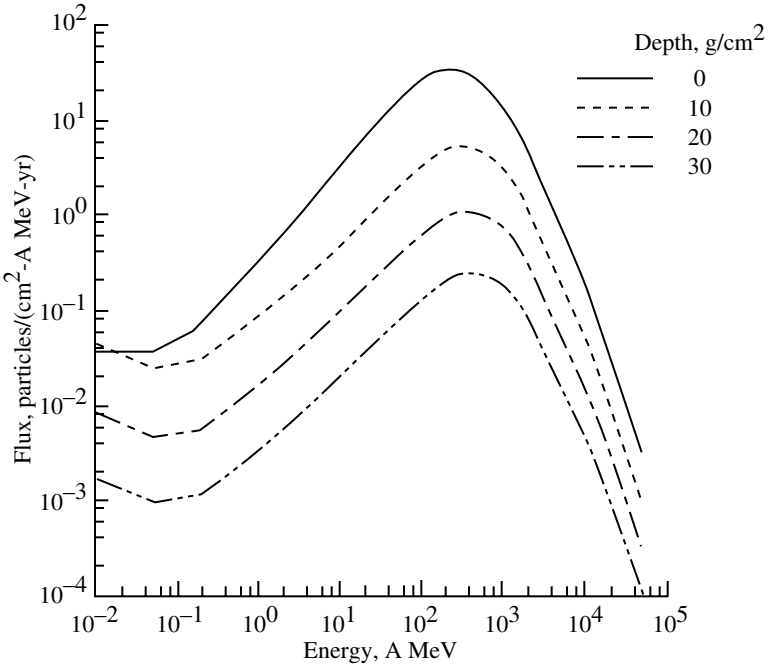

(a) 1977 solar minimum.

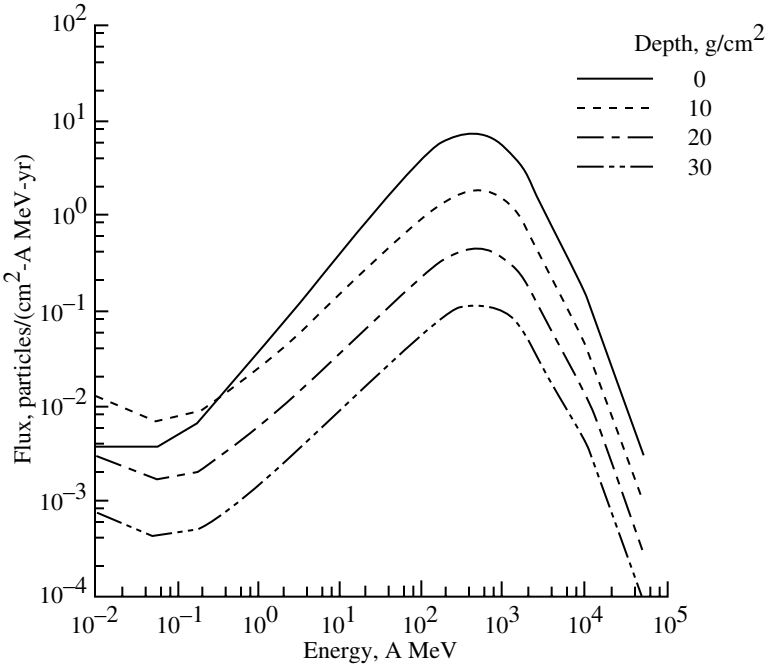

(b) 1981 solar maximum.

Figure 20. GCR energy flux for iron ion in water.

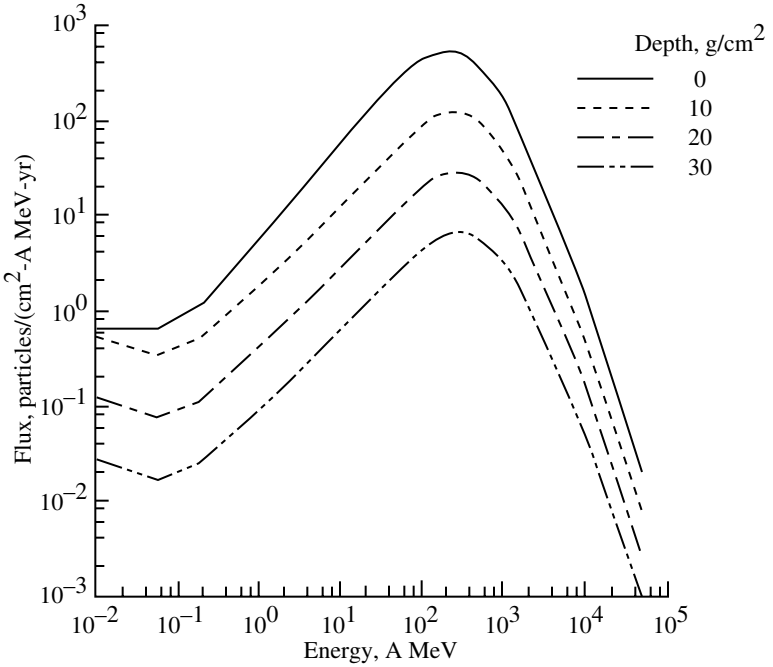

(a) 1977 solar minimum.

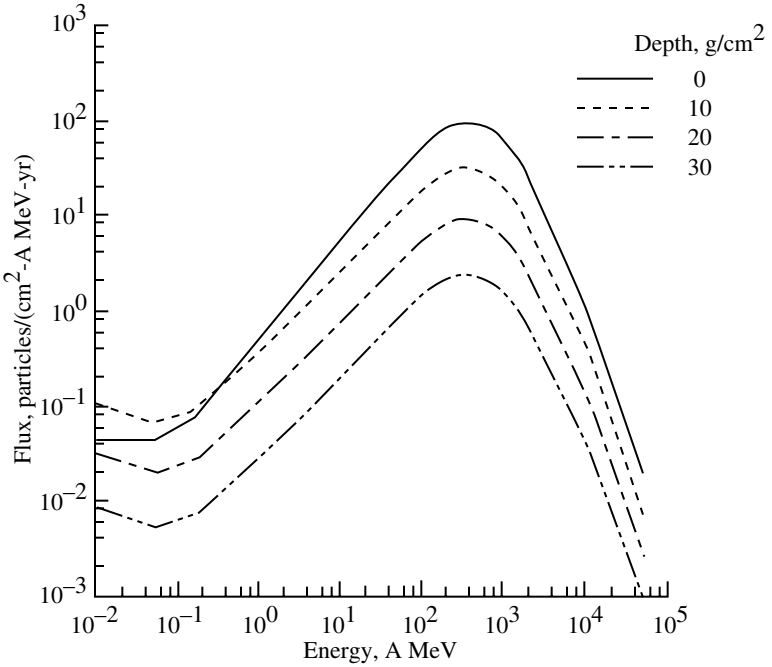

(b) 1981 solar maximum.

Figure 21. GCR energy flux for carbon ion in liquid hydrogen.

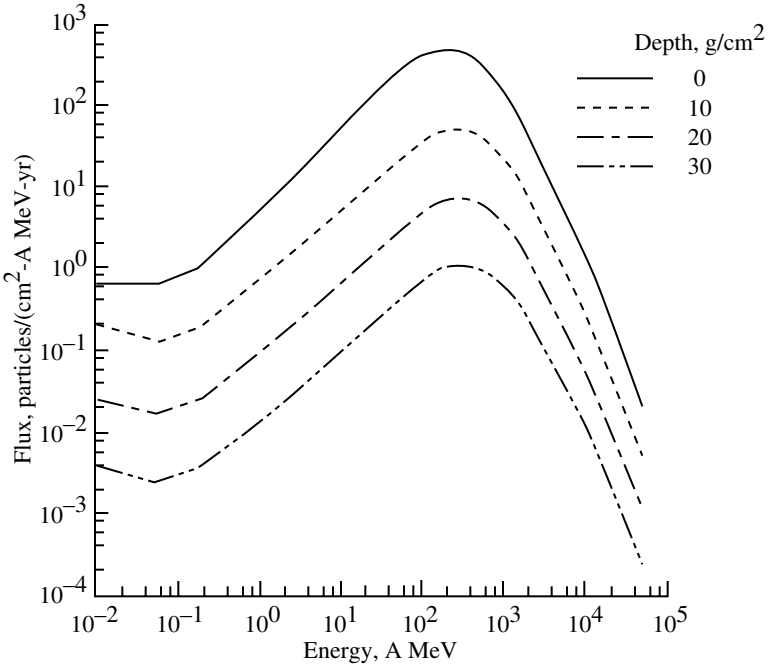

(a) 1977 solar minimum.

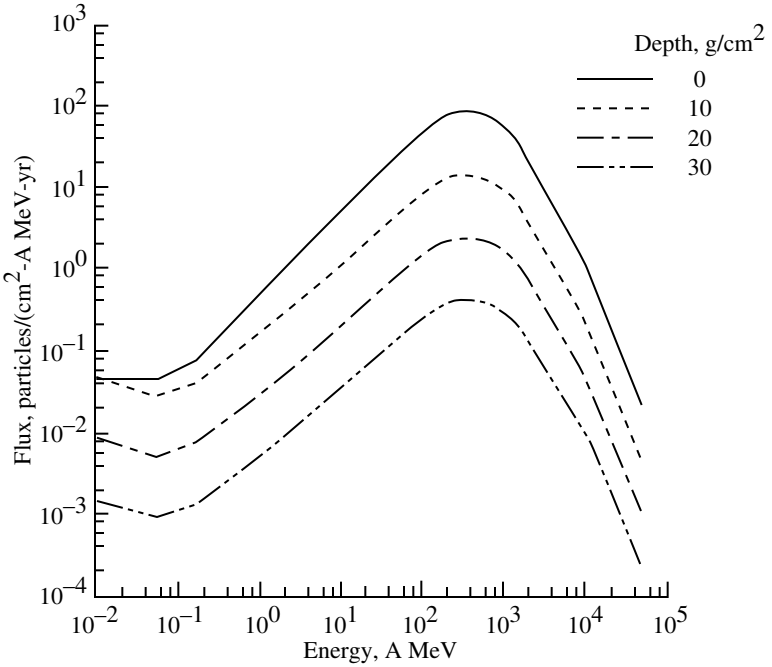

(b) 1981 solar maximum.

Figure 22. GCR energy flux for oxygen ion in liquid hydrogen.

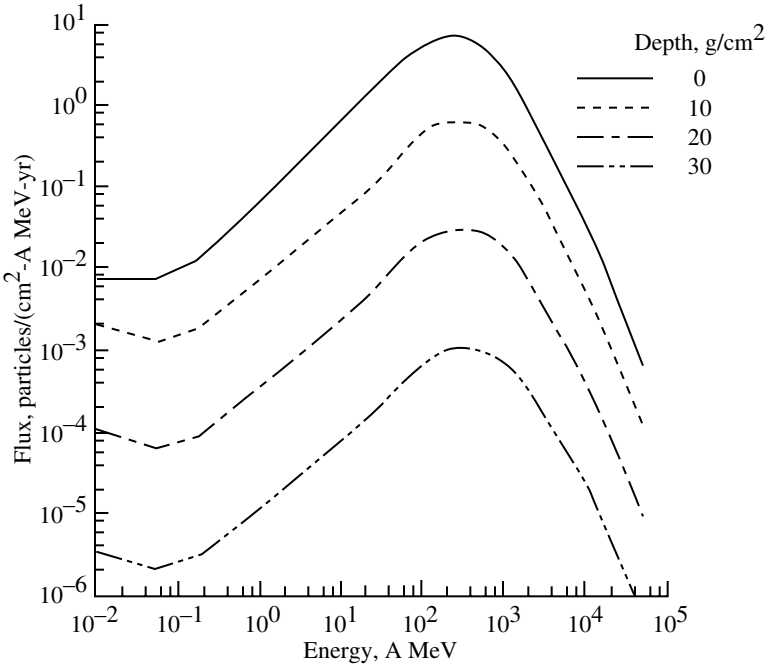

(a) 1977 solar minimum.

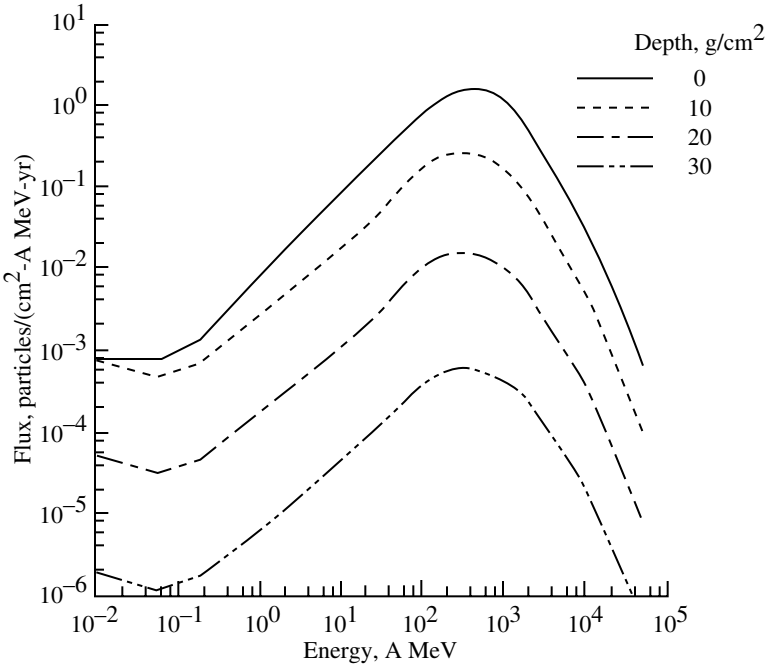

(b) 1981 solar maximum.

Figure 23. GCR energy flux for calcium ion in liquid hydrogen.

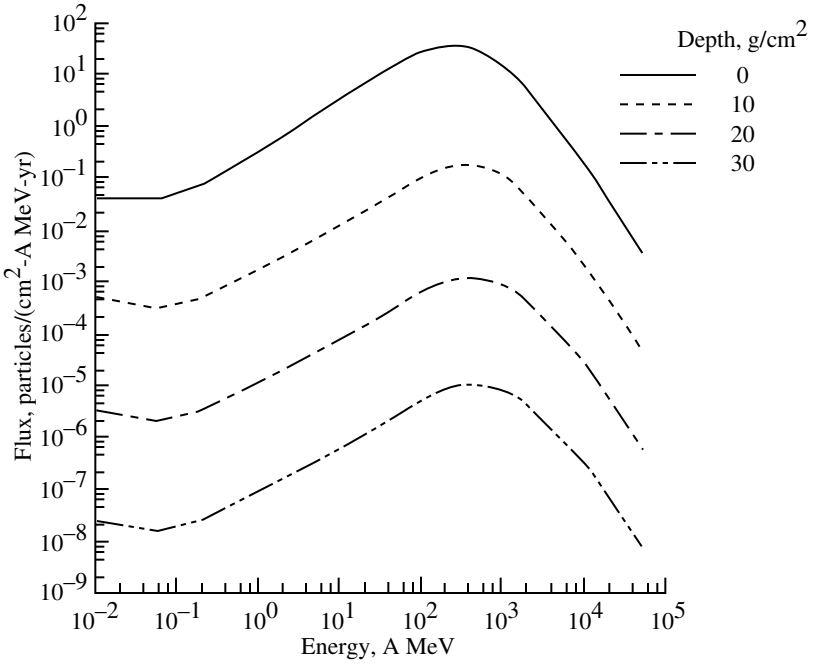

(a) 1977 solar minimum.

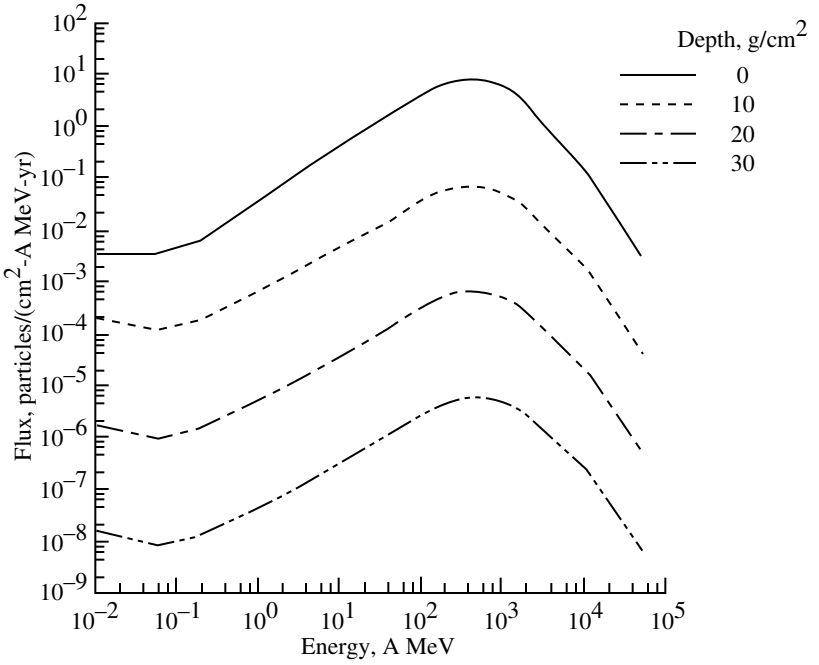

(b) 1981 solar maximum.

Figure 24. GCR energy flux for iron ion in liquid hydrogen.

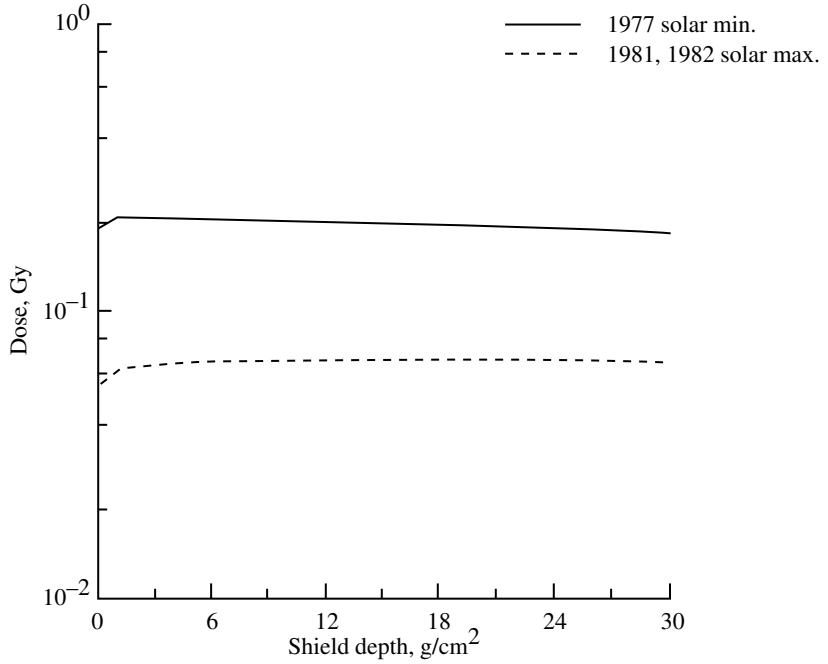

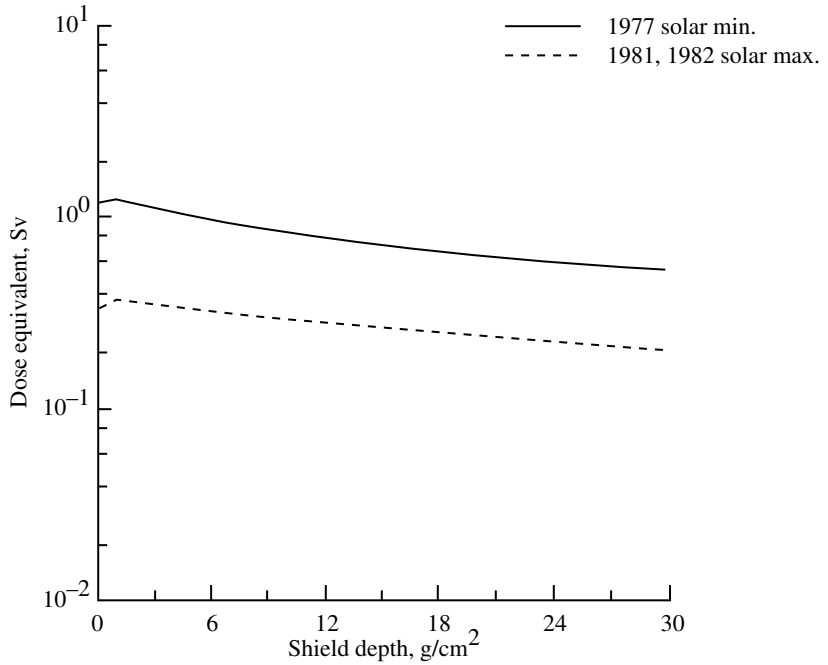

(a) In aluminum.

Figure 25. GCR skin dose and dose equivalent.

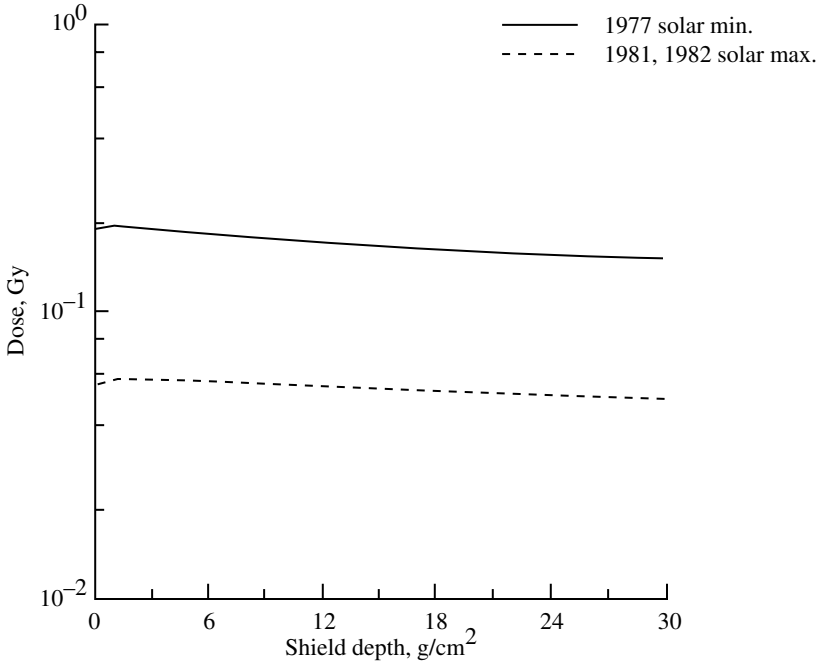

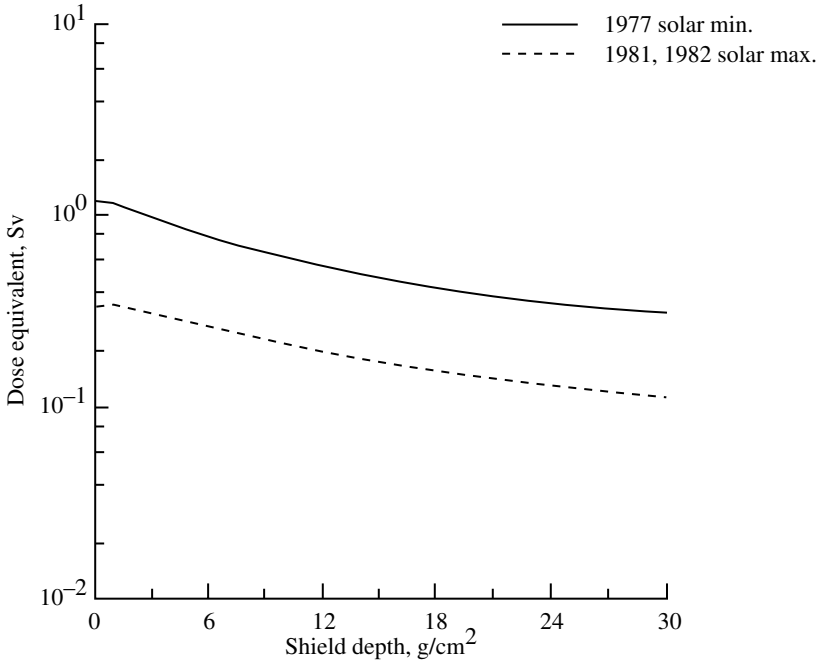

(b) In water.

Figure 25. Continued.

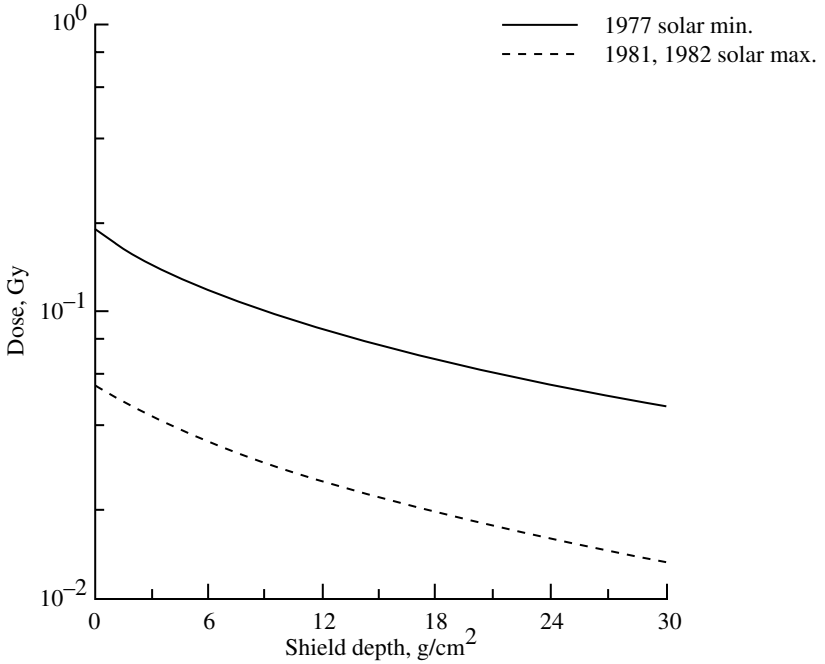

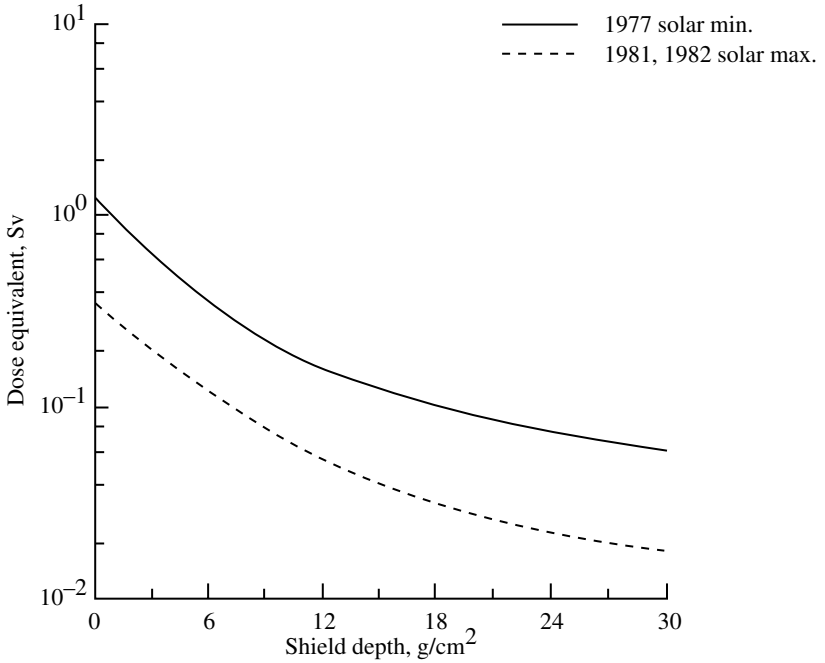

(c) In liquid hydrogen.

Figure 25. Concluded.

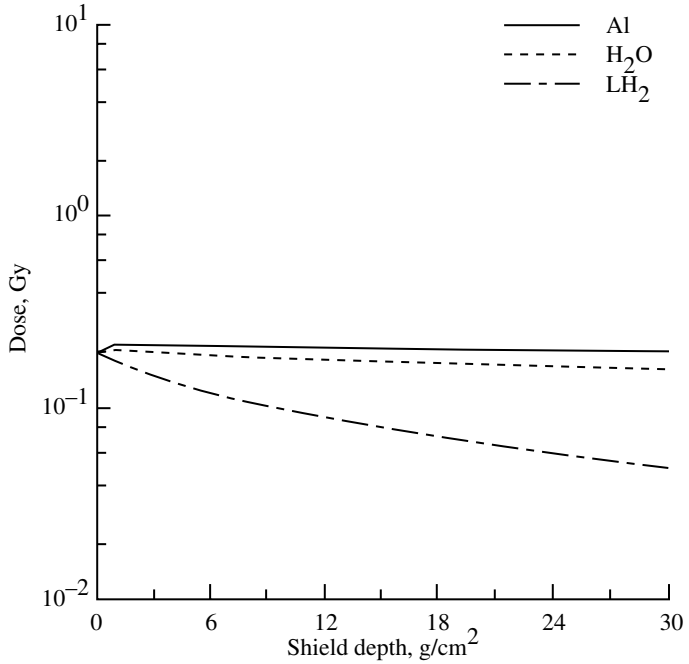

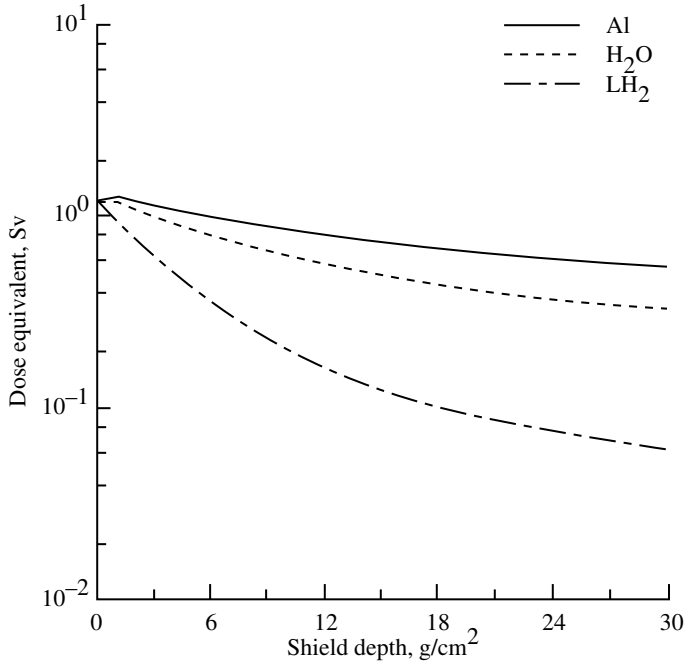

(a) 1977 solar minimum.

Figure 26. GCR skin dose and dose equivalent in aluminum, water, and liquid hydrogen.

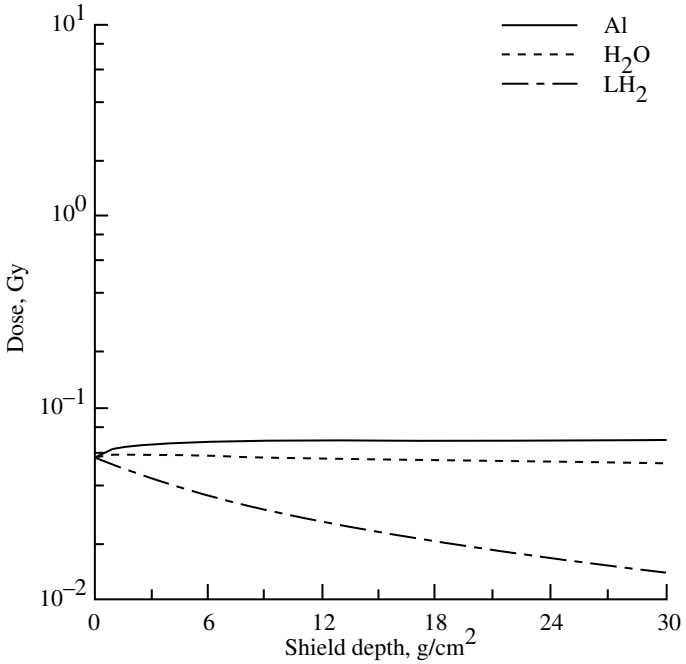

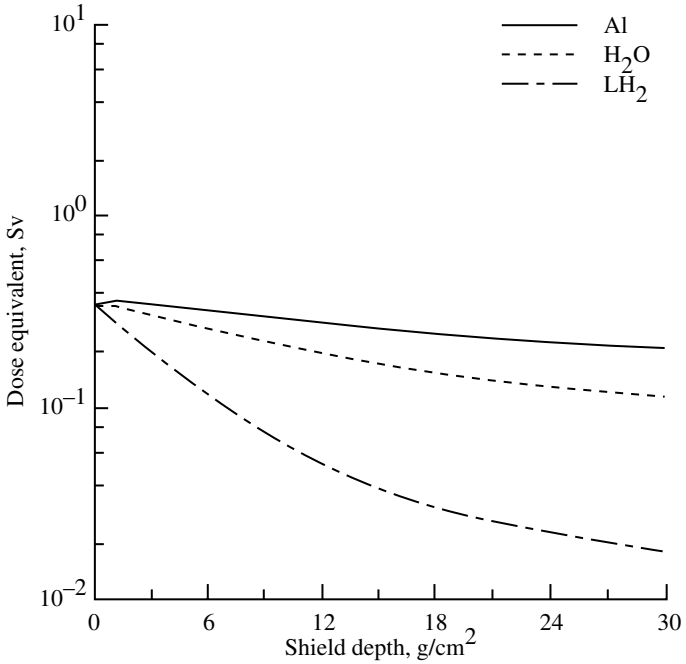

(b) 1981 solar maximum.

Figure 26. Concluded.

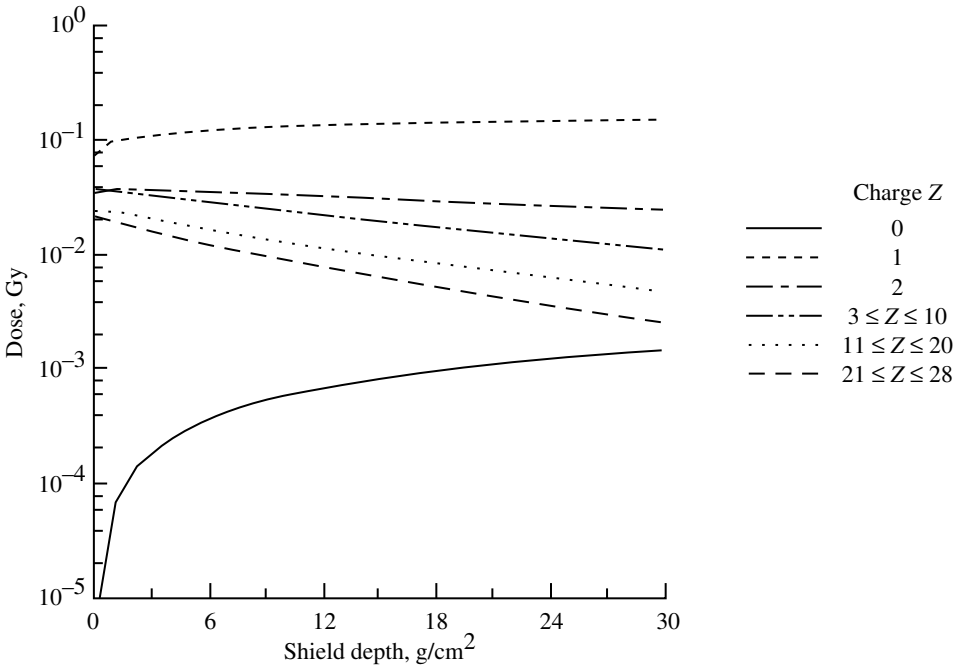

(a) 1977 solar minimum.

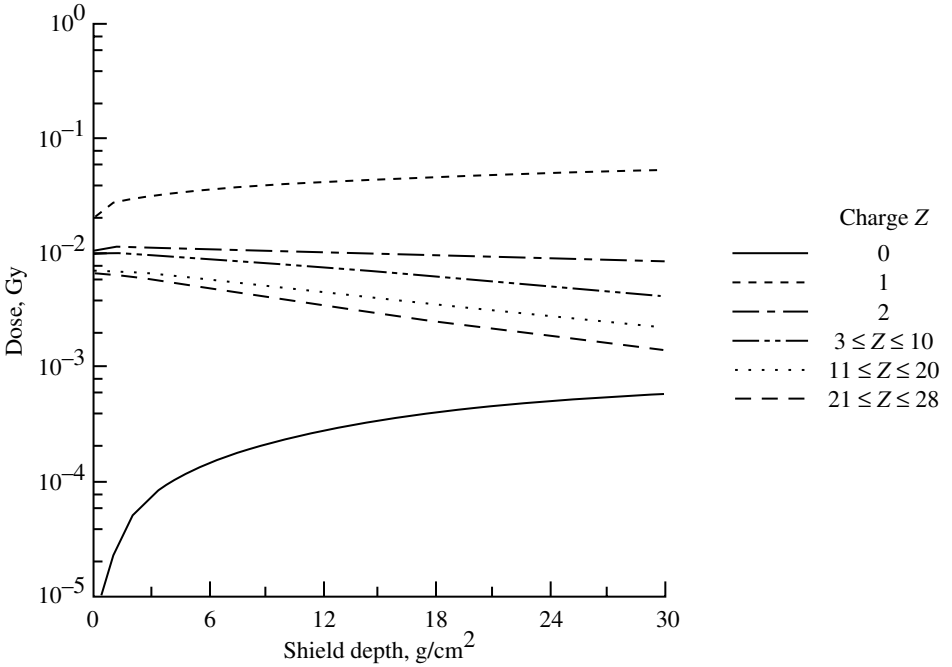

(b) 1981 solar maximum.

Figure 27. GCR skin dose for six charge Z groups in aluminum.

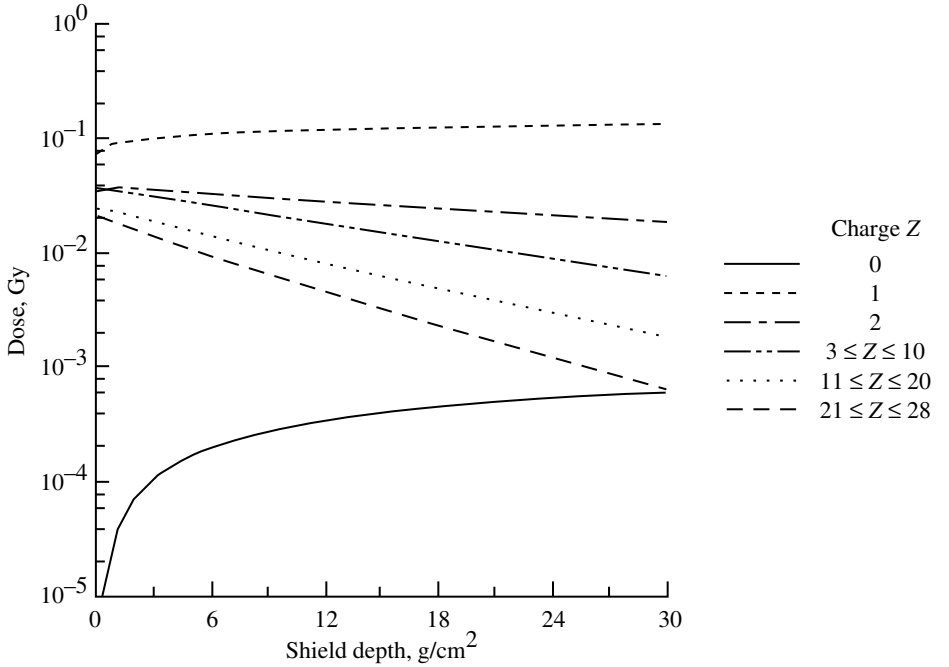

(a) 1977 solar minimum.

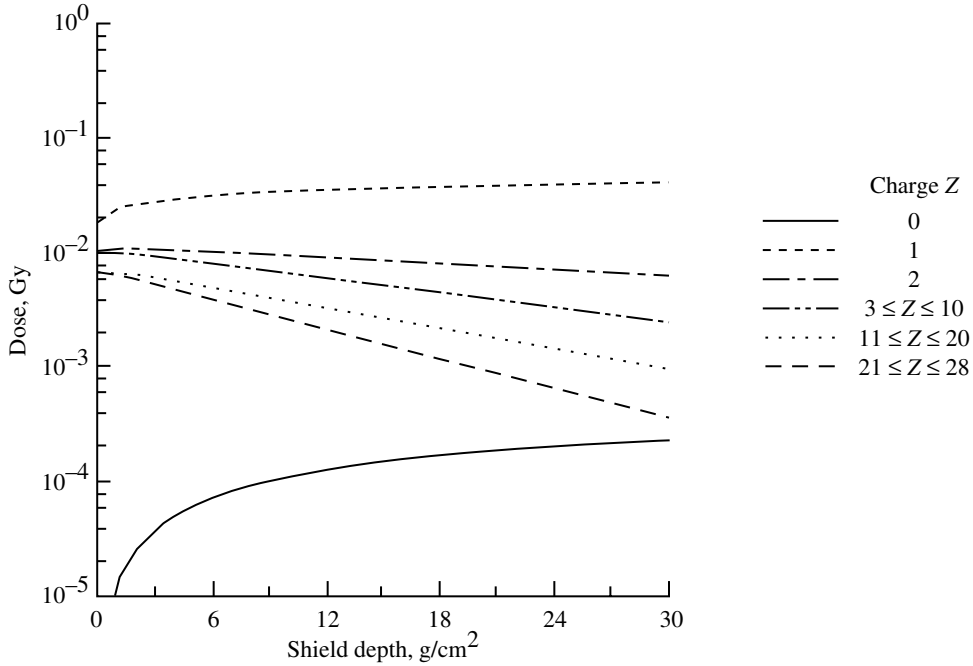

(b) 1981 solar maximum.

Figure 28. GCR skin dose for six charge Z groups in water.

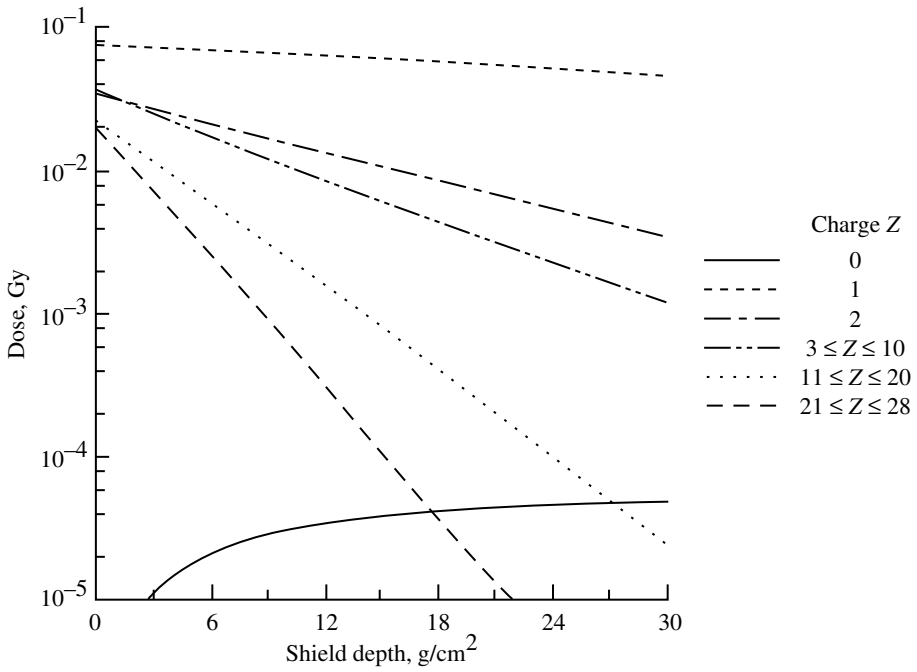

(a) 1977 solar minimum.

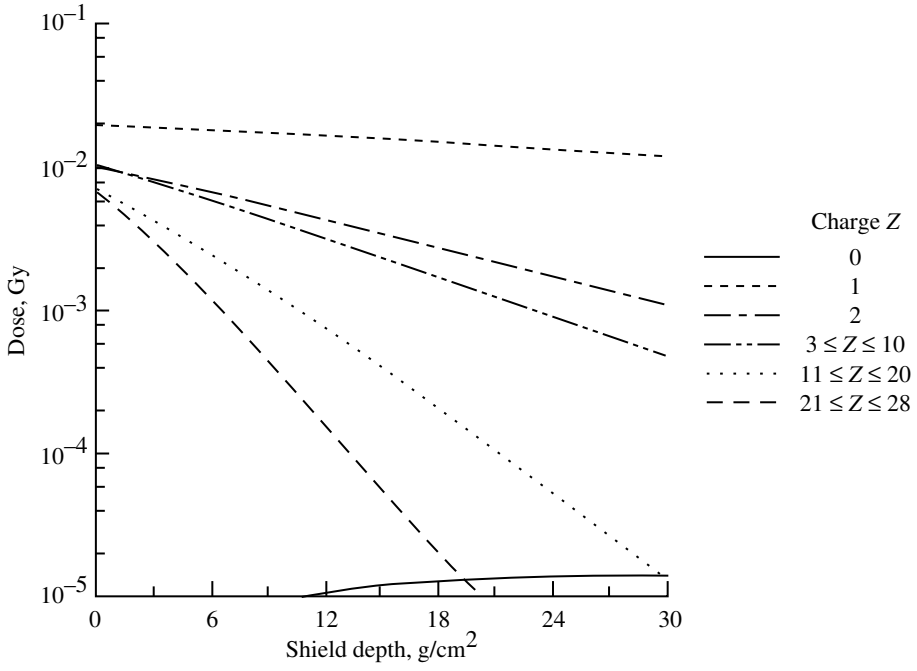

(b) 1981 solar maximum.

Figure 29. GCR skin dose for six charge Z groups in liquid hydrogen.

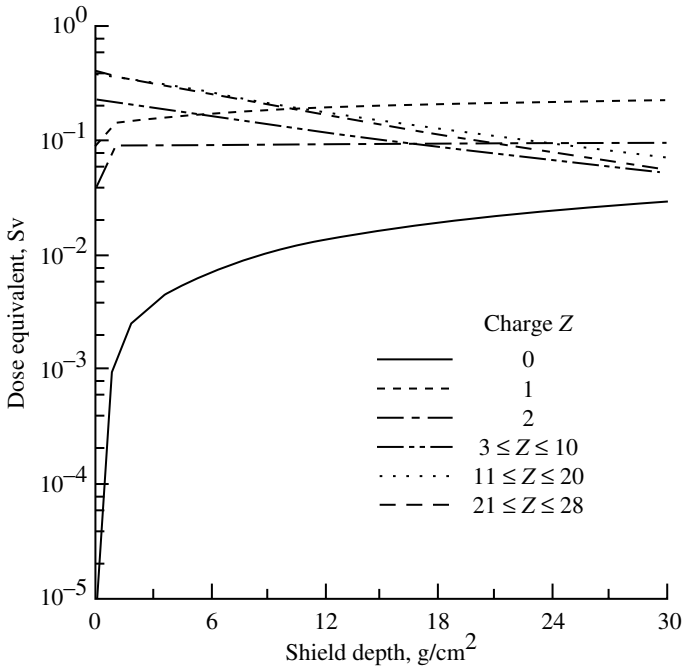

(a) 1977 solar minimum.

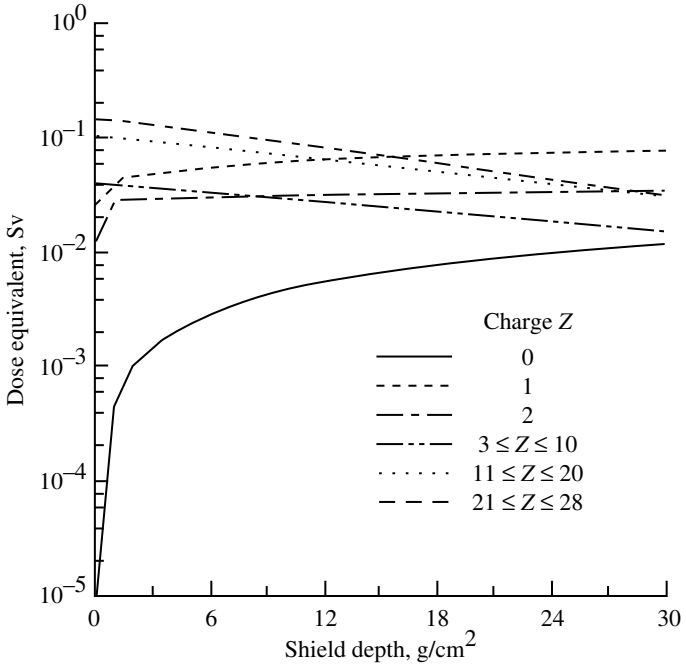

(b) 1981 solar maximum.

Figure 30. GCR skin dose equivalent for six charge Z groups in aluminum.

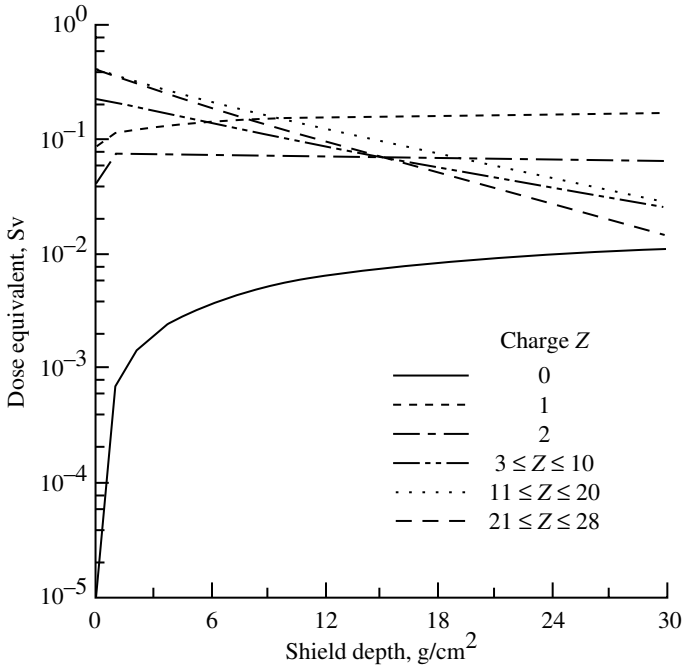

(a) 1977 solar minimum.

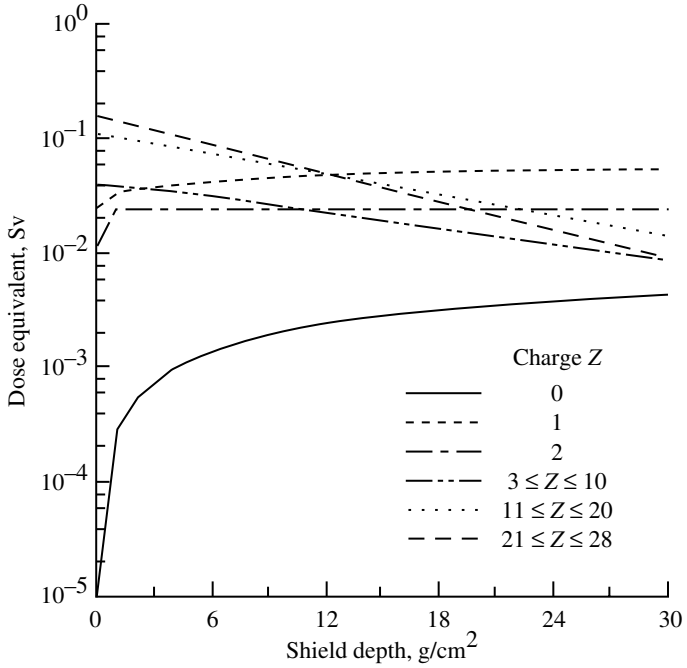

(b) 1981 solar maximum.

Figure 31. GCR skin dose equivalent for six charge Z groups in water.

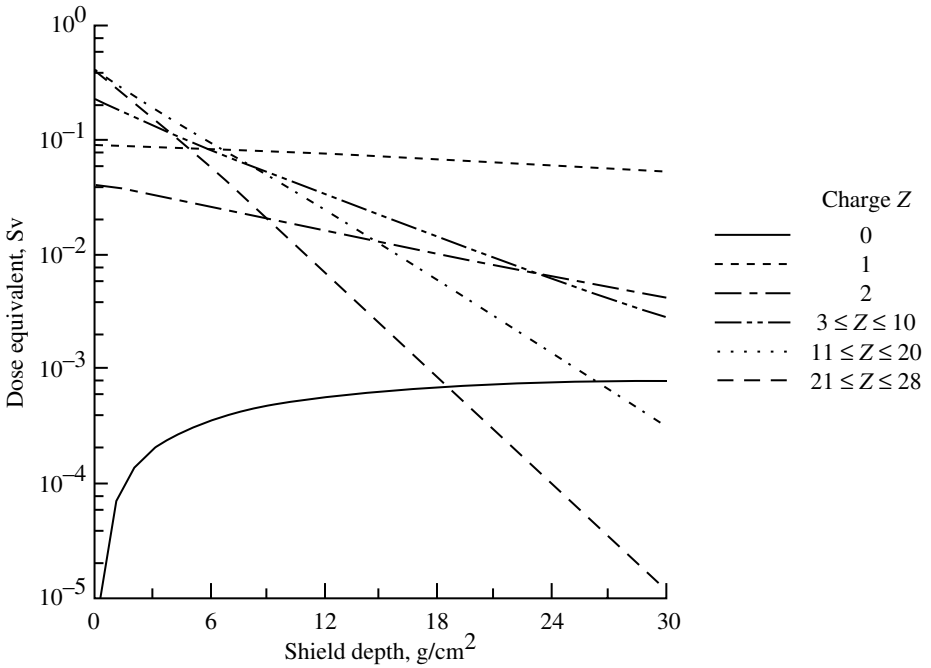

(a) 1977 solar minimum.

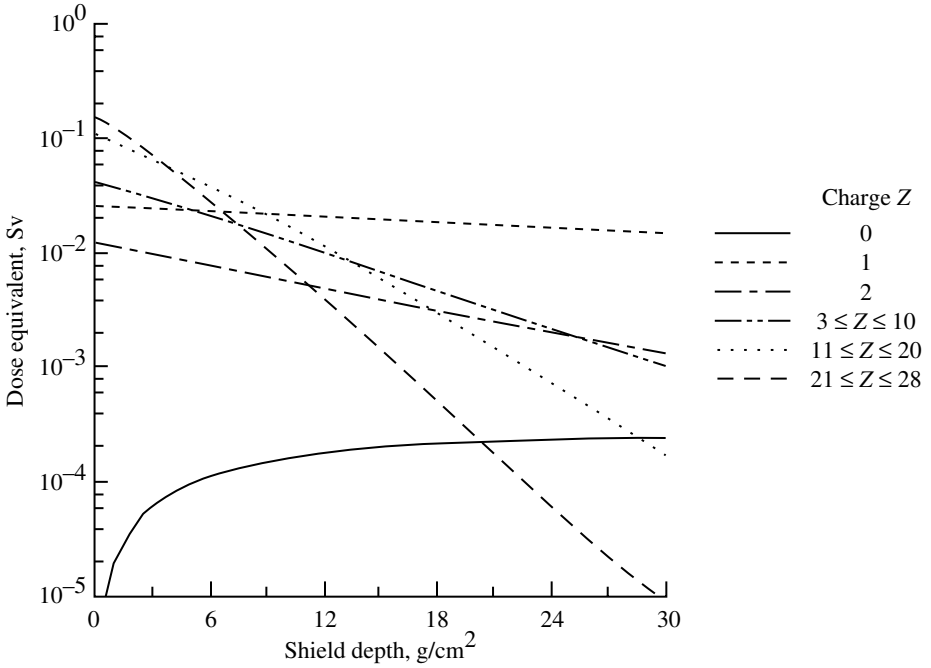

(b) 1981 solar maximum.

Figure 32. GCR skin dose equivalent for six charge Z groups in liquid hydrogen.

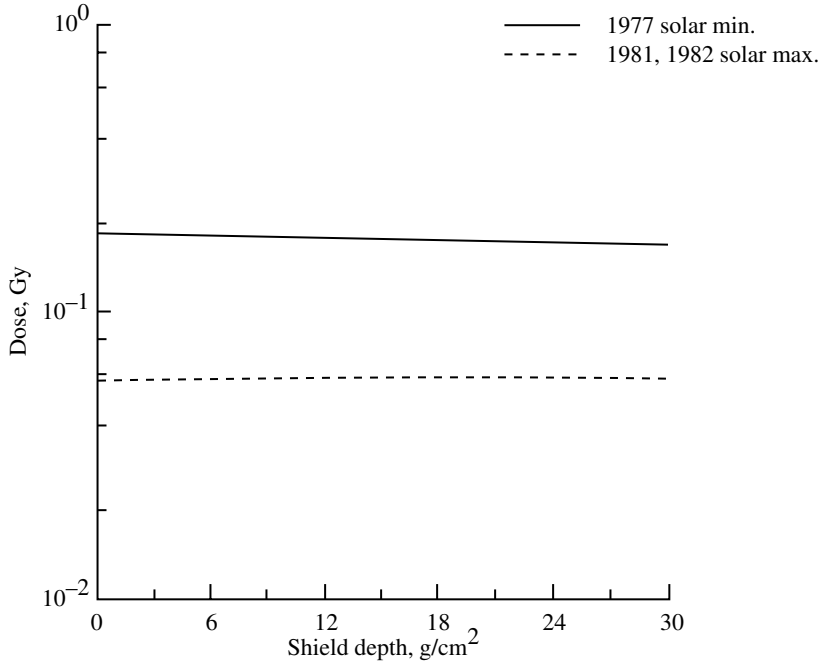

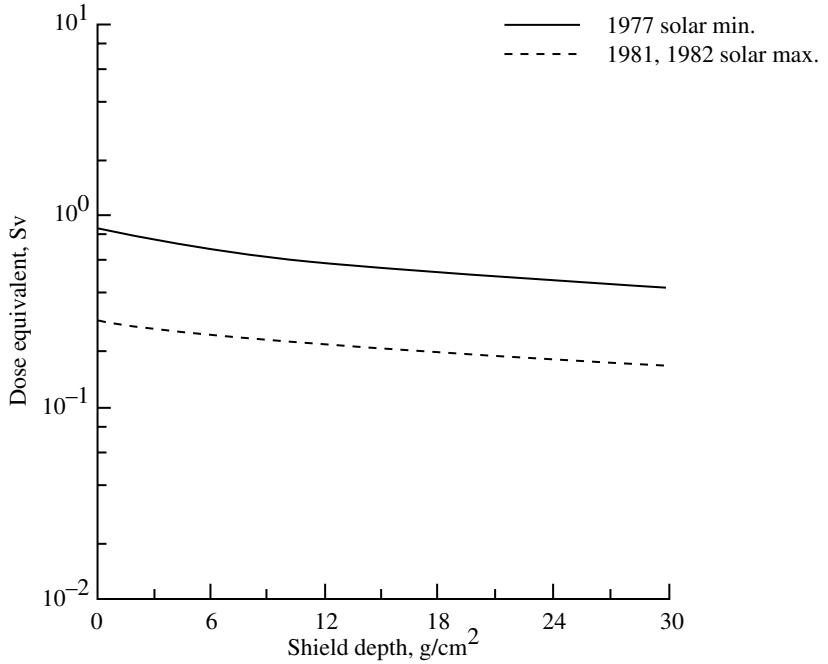

(a) In aluminum.

Figure 33. GCR 5-cm-BFO dose and dose equivalent.

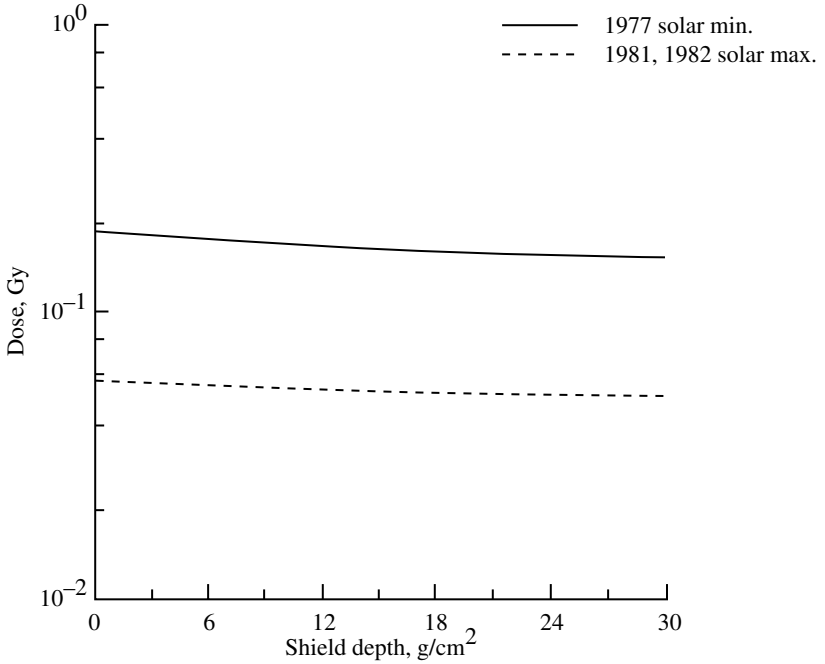

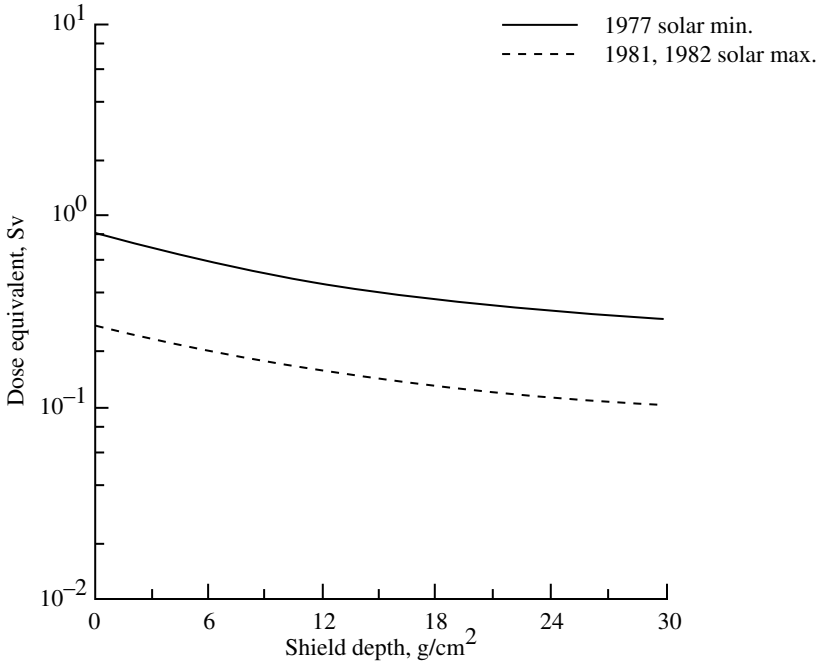

(b) In water.

Figure 33. Continued.

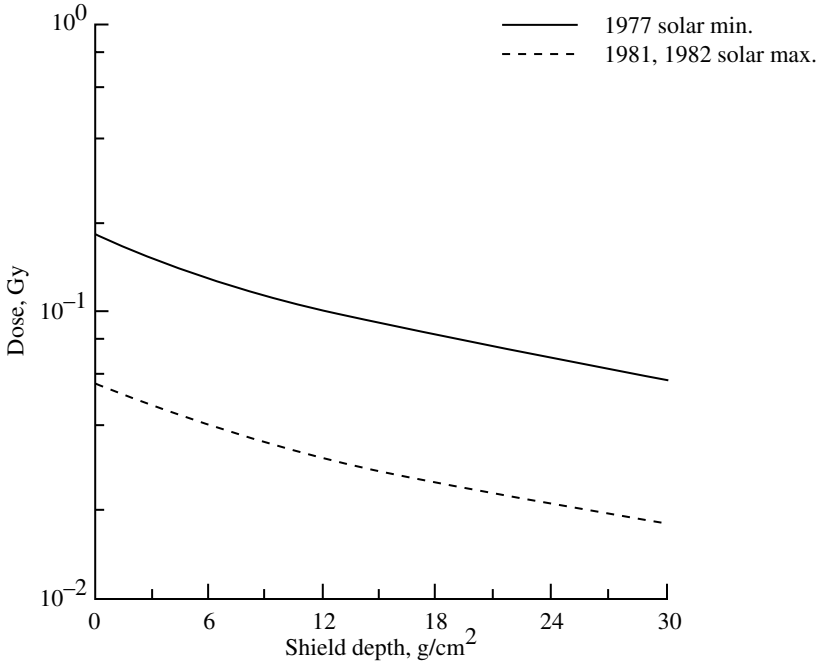

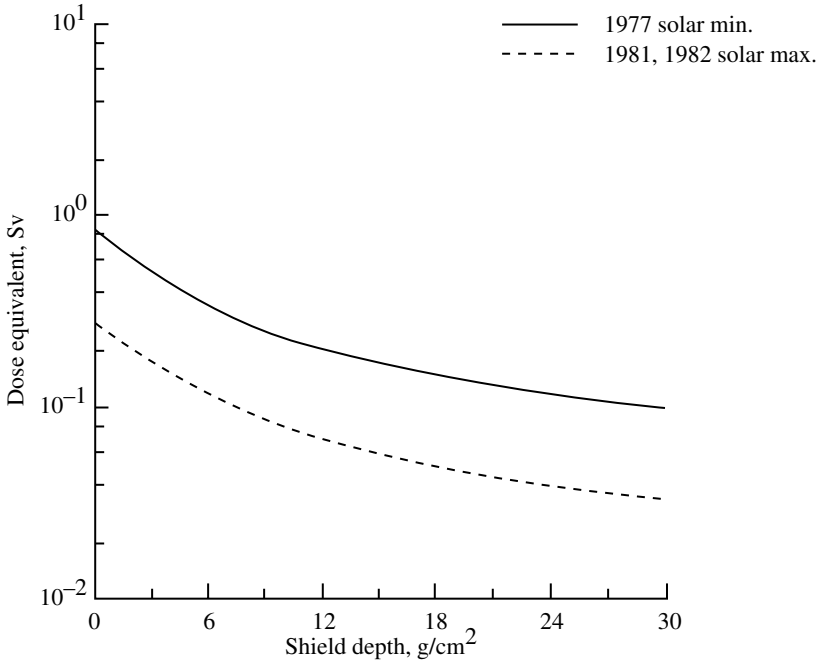

(c) In liquid hydrogen.

Figure 33. Concluded.

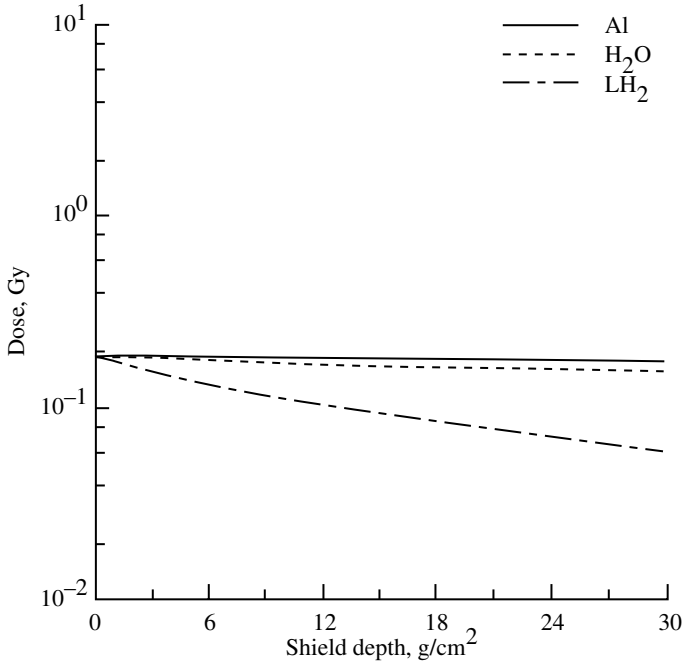

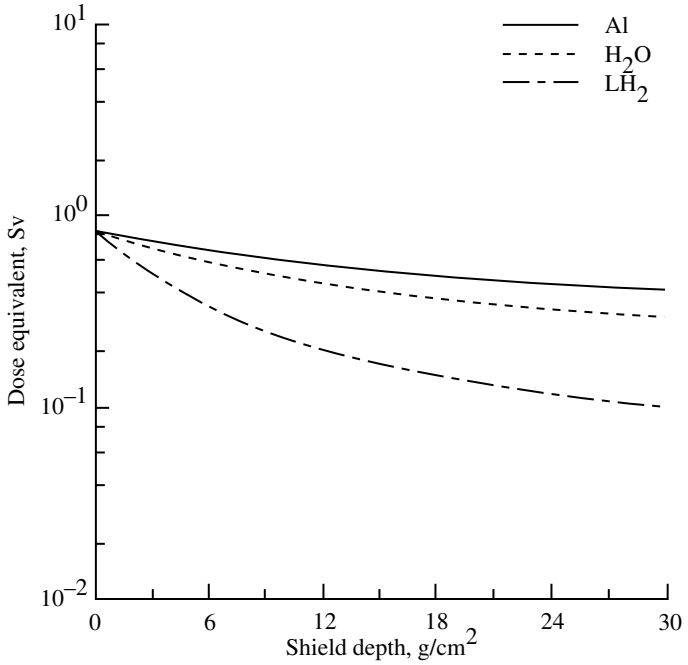

(a) 1977 solar minimum.

Figure 34. GCR 5-cm-BFO dose and dose equivalent in aluminum, water, and liquid hydrogen.

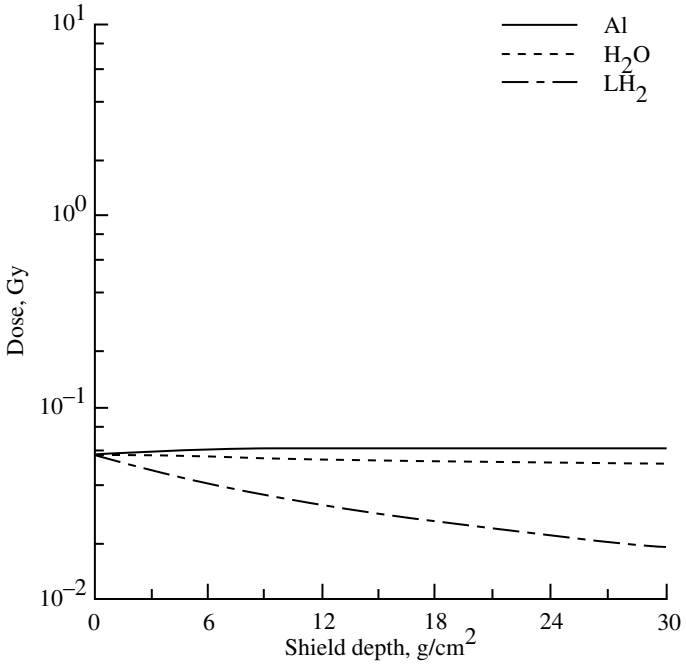

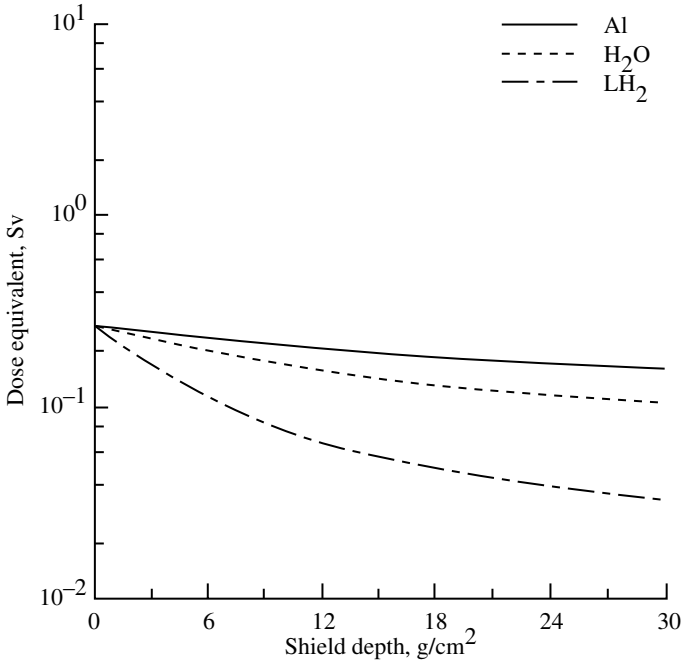

(b) 1981 solar maximum.

Figure 34. Concluded.

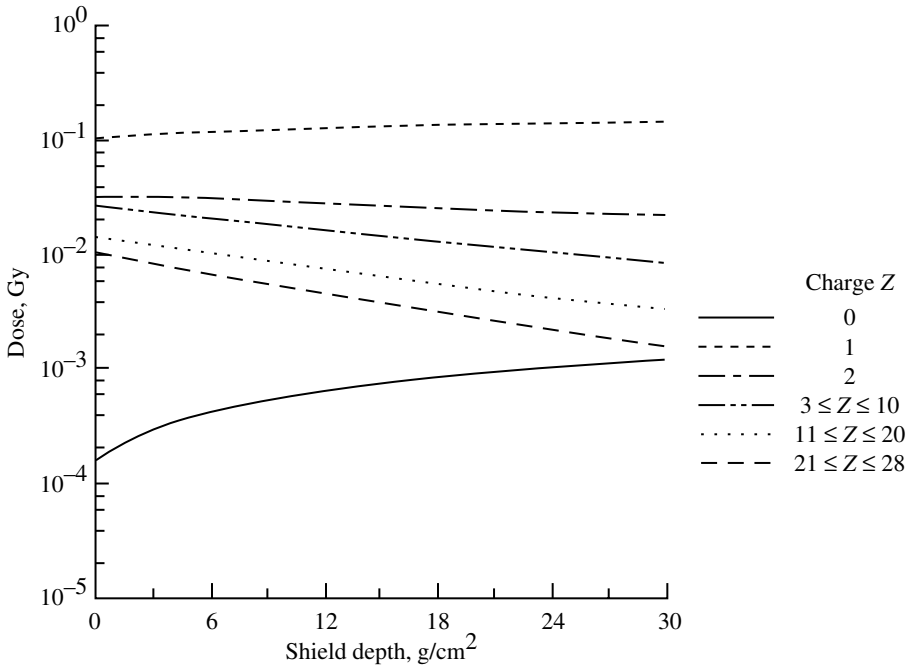

(a) 1977 solar minimum.

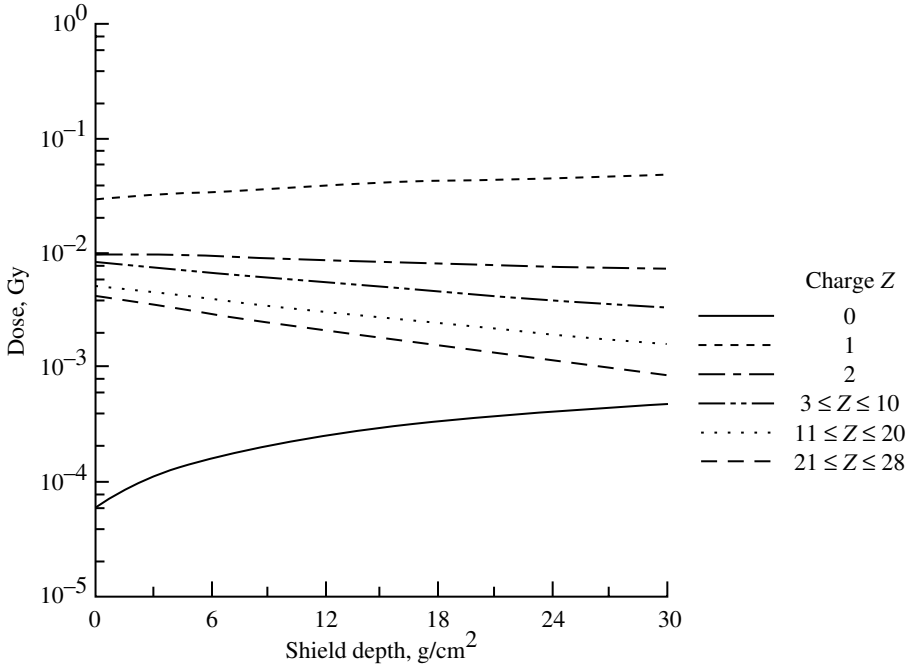

(b) 1981 solar maximum.

Figure 35. GCR 5-cm-BFO dose for six charge Z groups in aluminum.

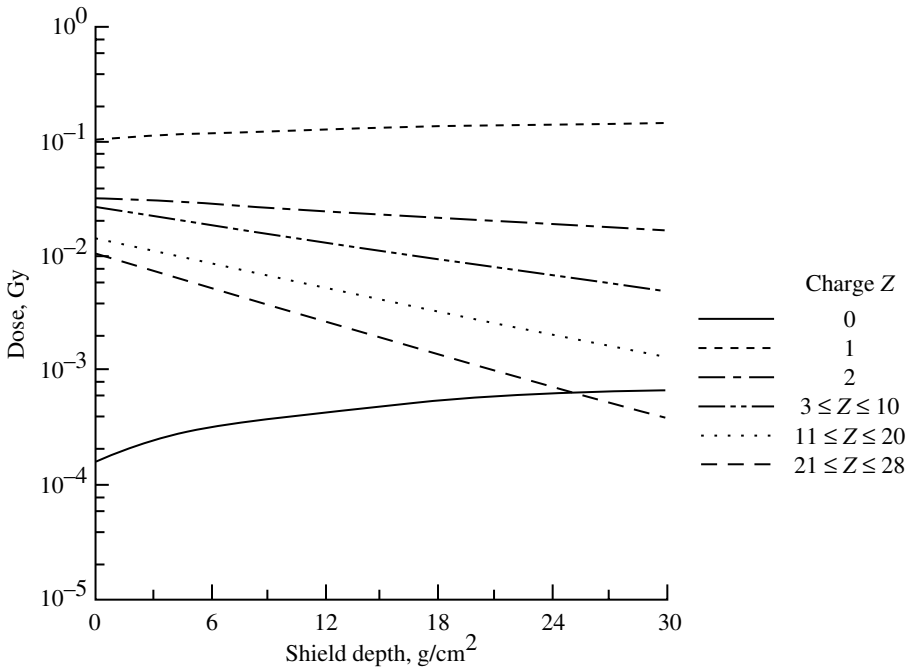

(a) 1977 solar minimum.

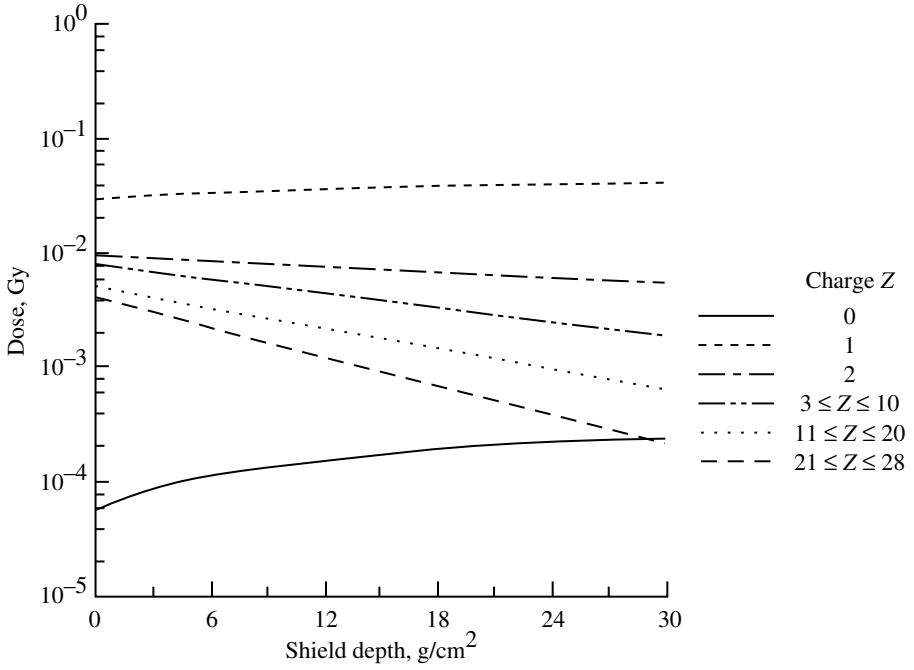

(b) 1981 solar maximum.

Figure 36. GCR 5-cm-BFO dose for six charge Z groups in water.

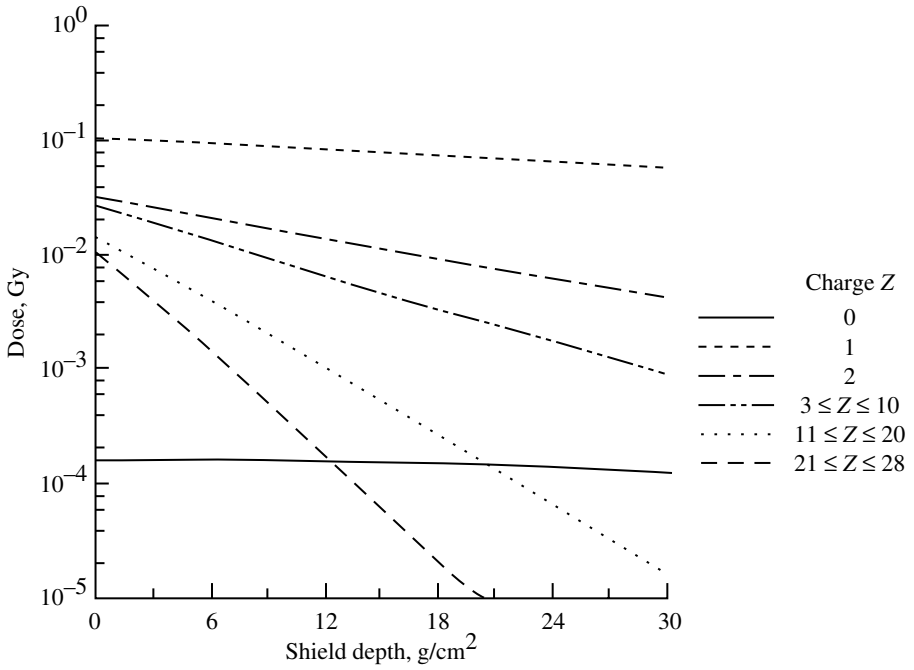

(a) 1977 solar minimum.

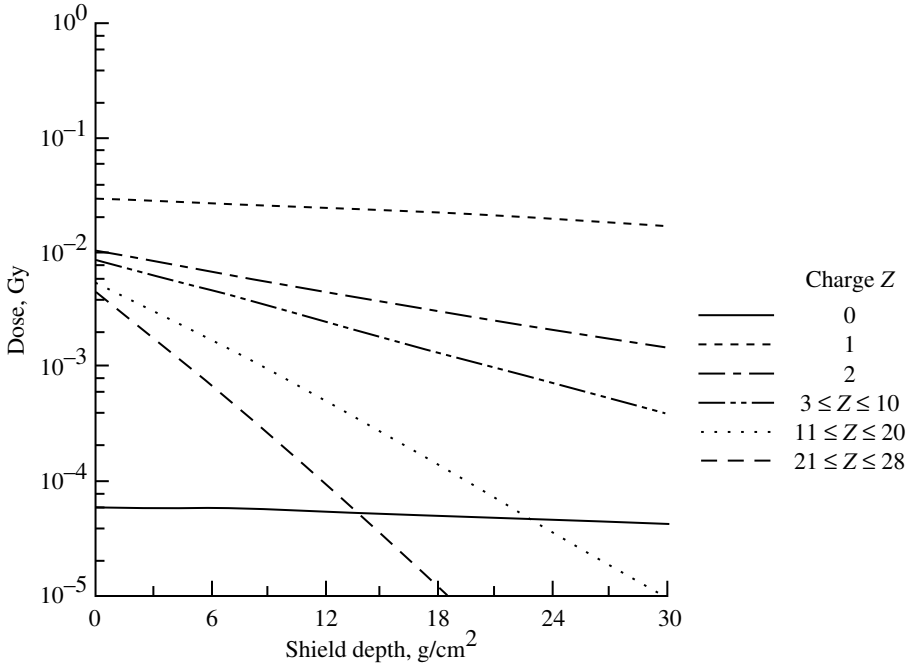

(b) 1981 solar maximum.

Figure 37. GCR 5-cm-BFO dose for six charge Z groups in liquid hydrogen.

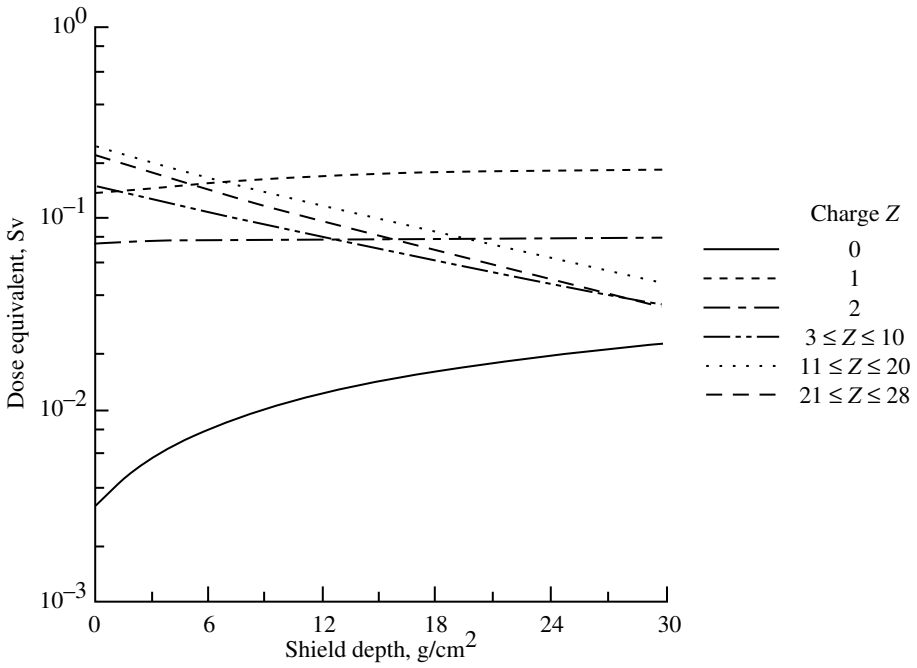

(a) 1977 solar minimum.

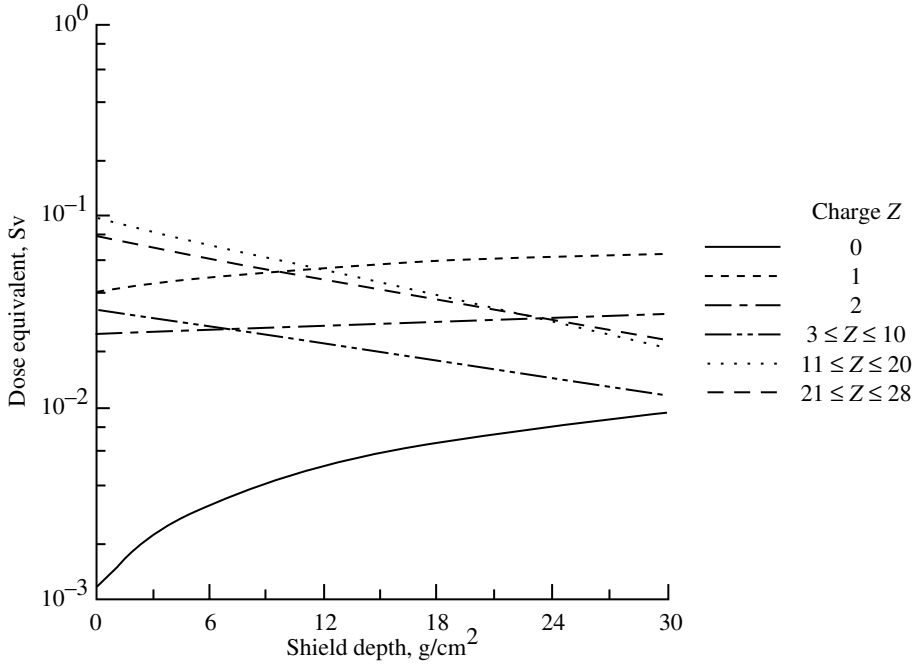

(b) 1981 solar maximum.

Figure 38. GCR 5-cm-BFO dose equivalent for six charge Z groups in aluminum.

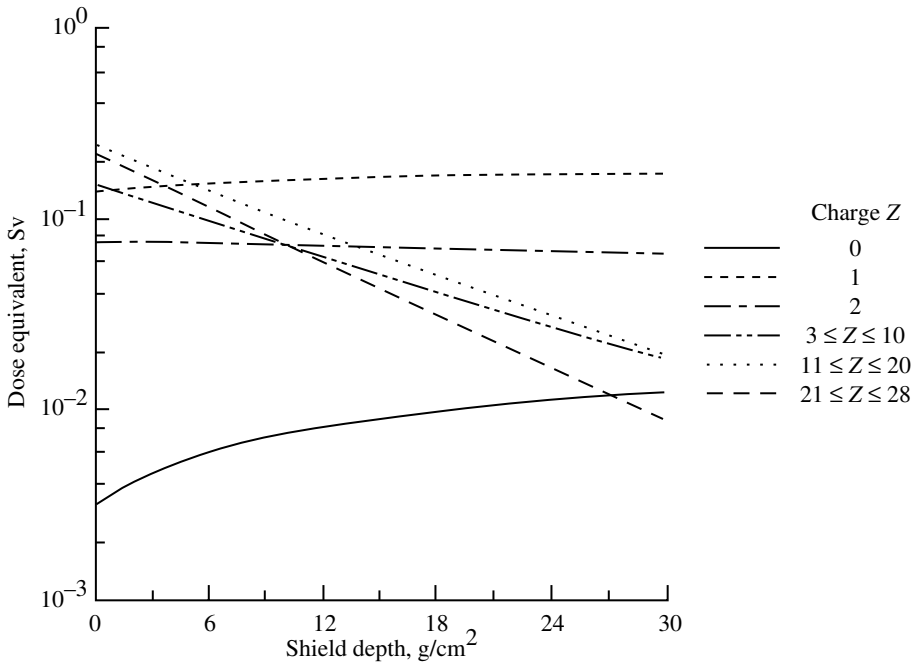

(a) 1977 solar minimum.

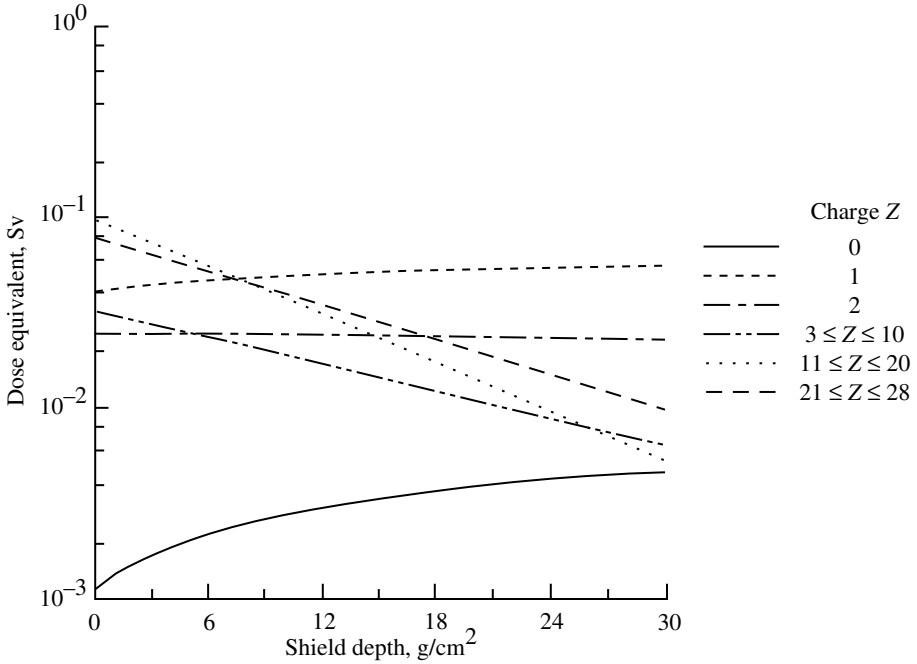

(b) 1981 solar maximum.

Figure 39. GCR 5-cm-BFO dose equivalent for six charge Z groups in water.

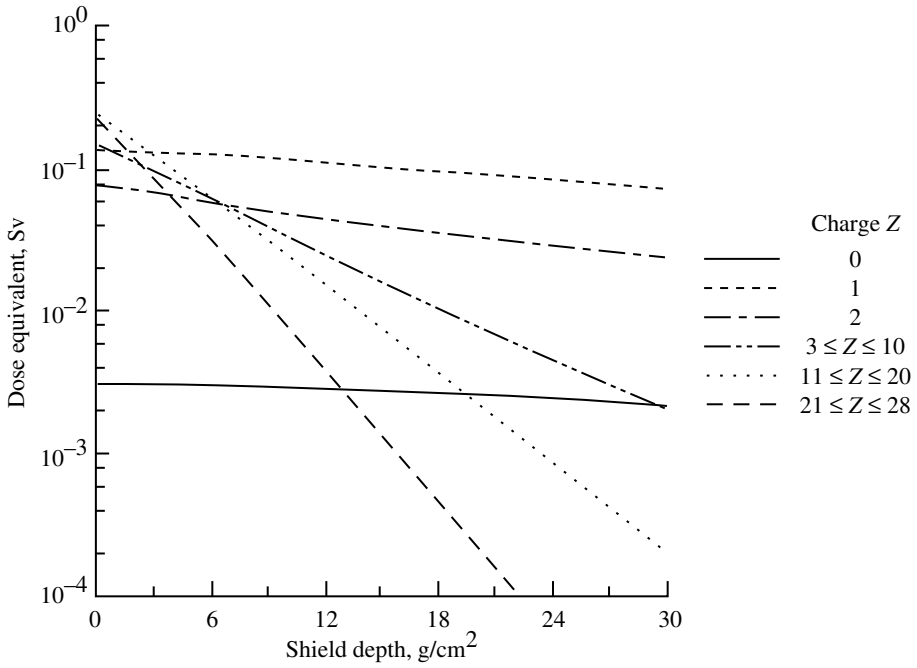

(a) 1977 solar minimum.

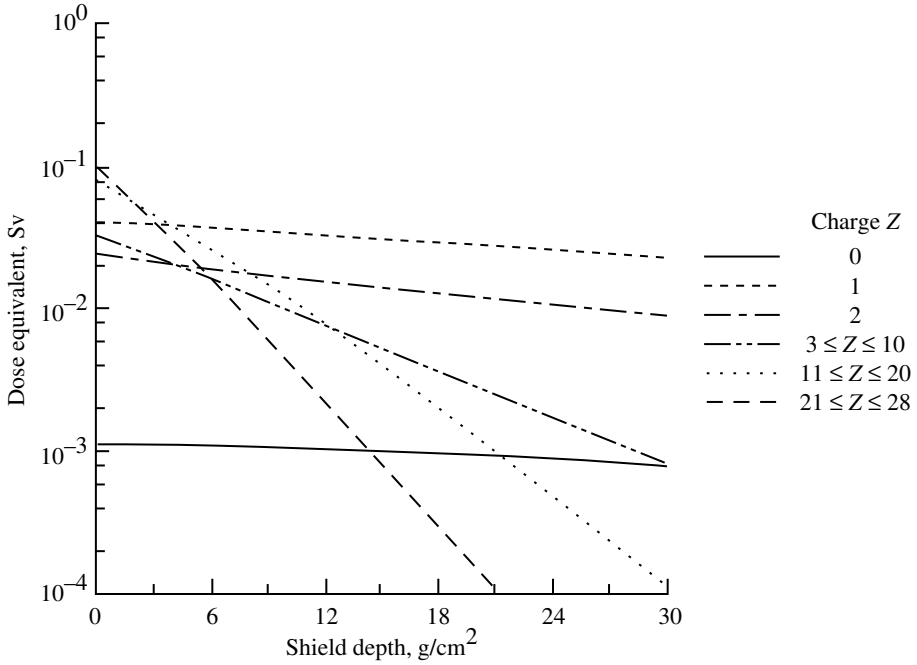

(b) 1981 solar maximum.

Figure 40. GCR 5-cm-BFO dose equivalent for six charge Z groups in liquid hydrogen.

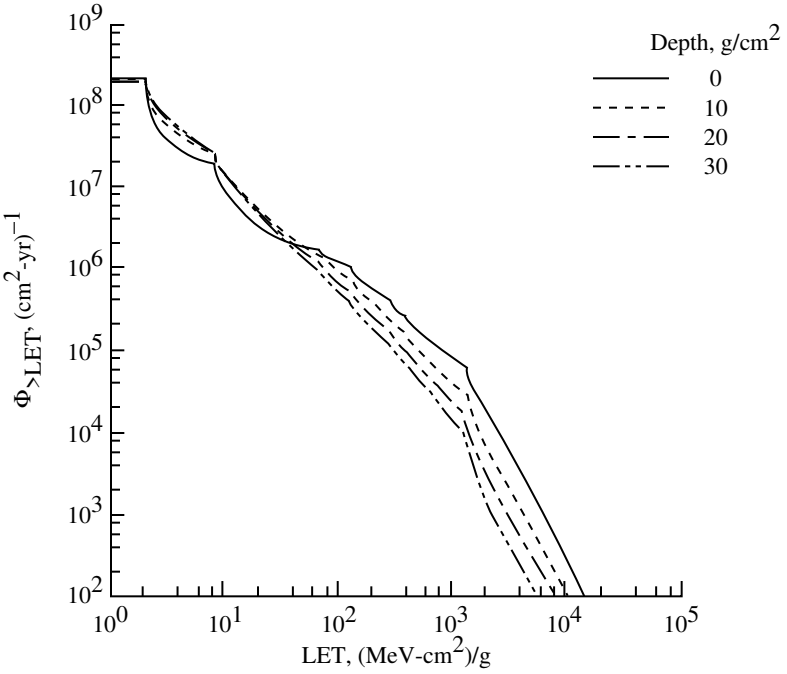

(a) 1977 solar minimum.

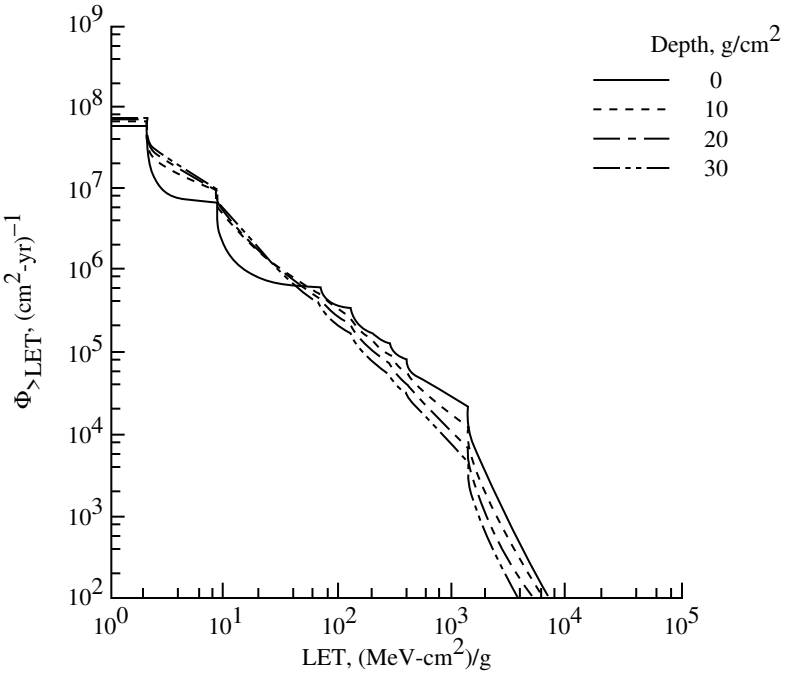

(b) 1981 solar maximum.

Figure 41. GCR skin integral flux LET spectra in aluminum.

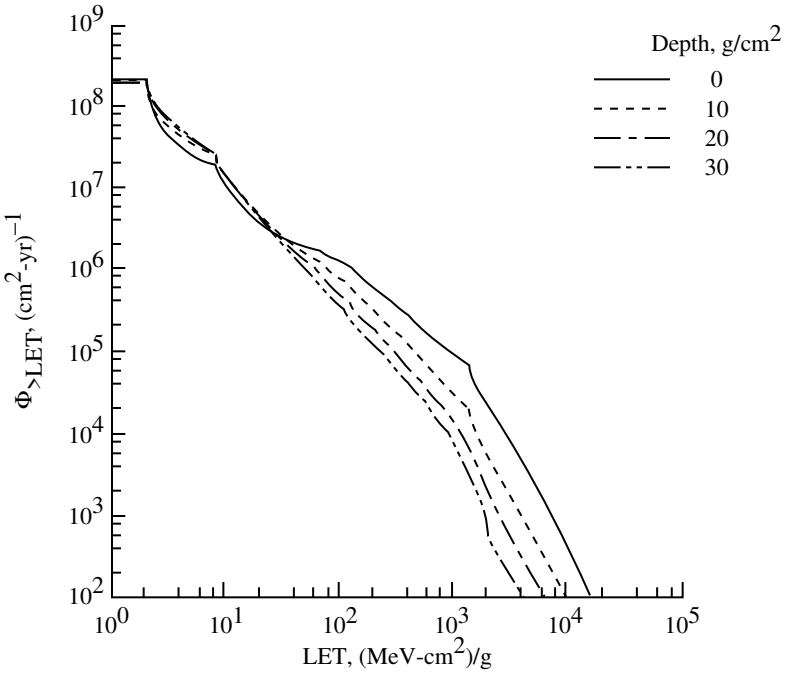

(a) 1977 solar minimum.

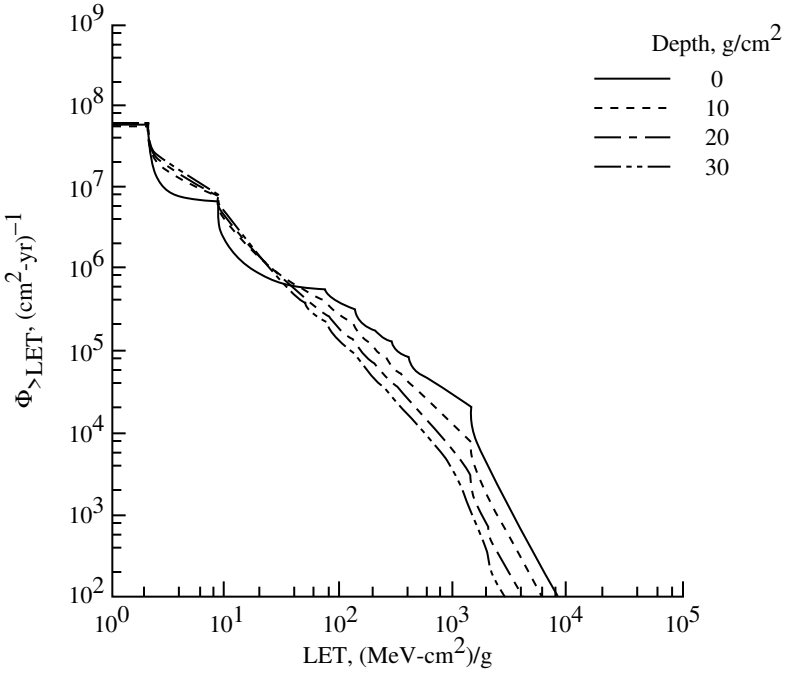

(b) 1981 solar maximum.

Figure 42. GCR skin integral flux LET spectra in water.

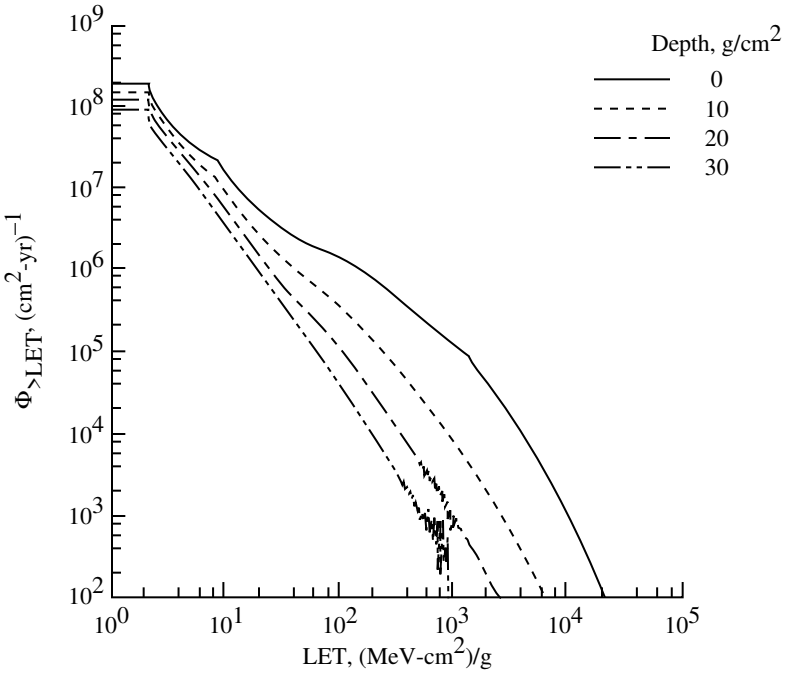

(a) 1977 solar minimum.

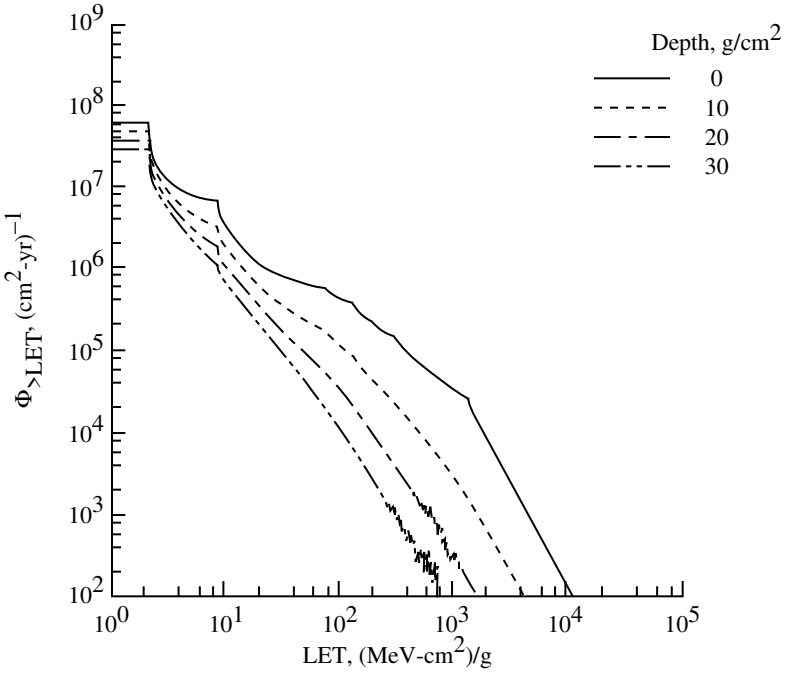

(b) 1981 solar maximum.

Figure 43. GCR skin integral flux LET spectra in liquid hydrogen.

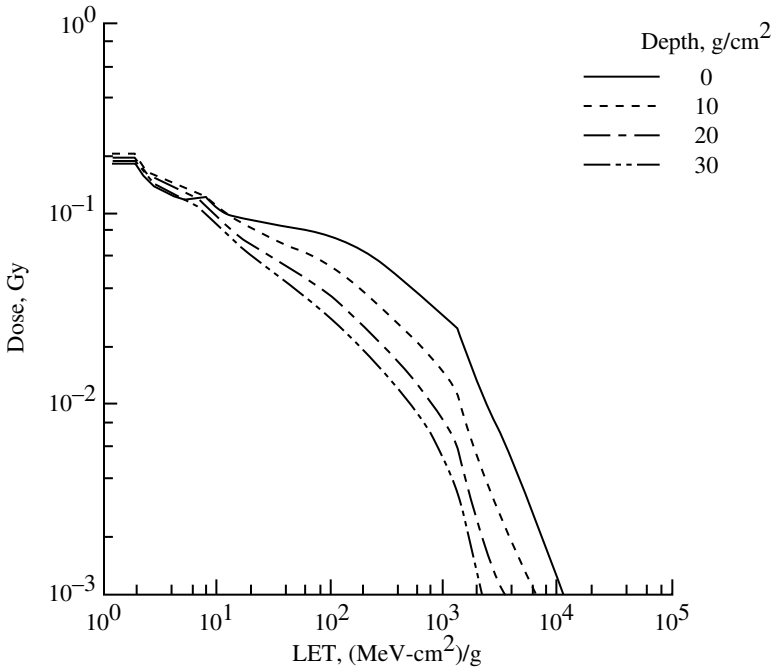

(a) 1977 solar minimum.

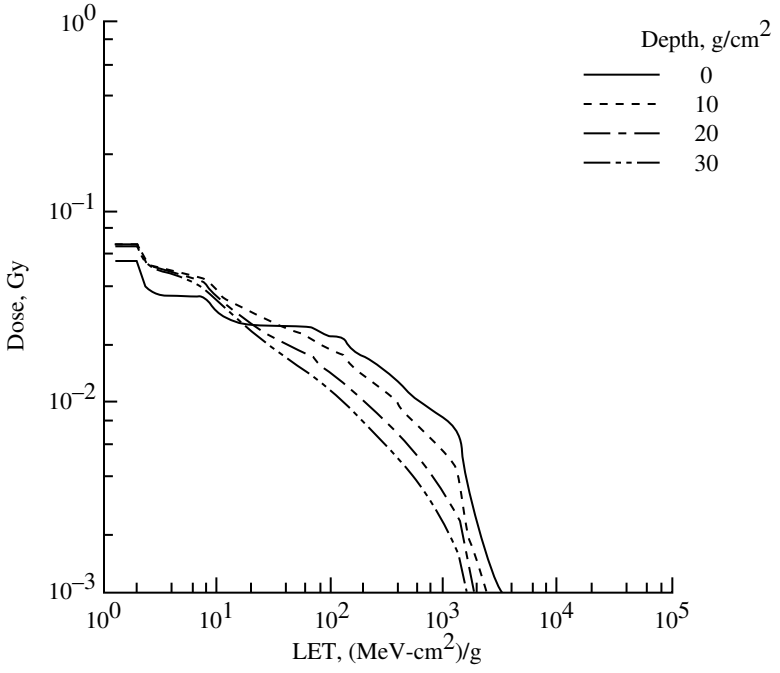

(b) 1981 solar maximum.

Figure 44. GCR skin dose LET spectra in aluminum.

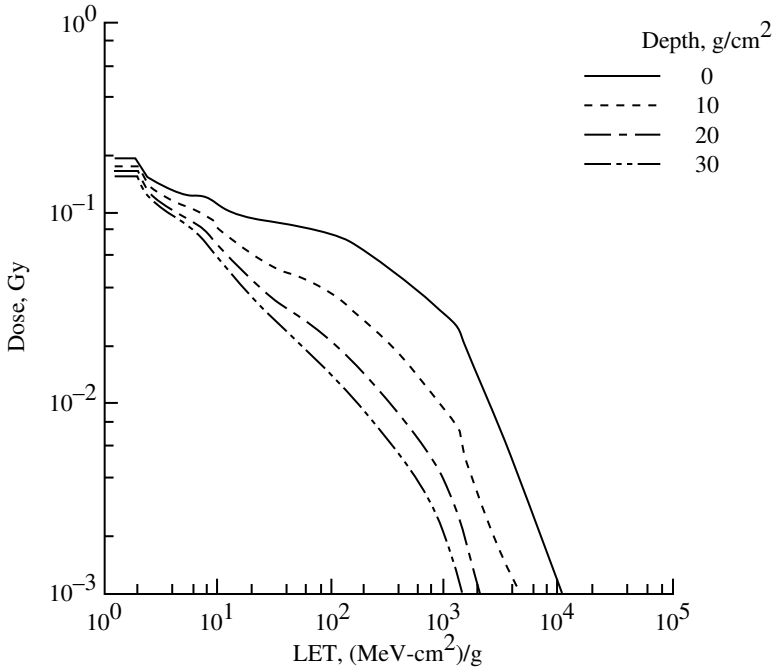

(a) 1977 solar minimum.

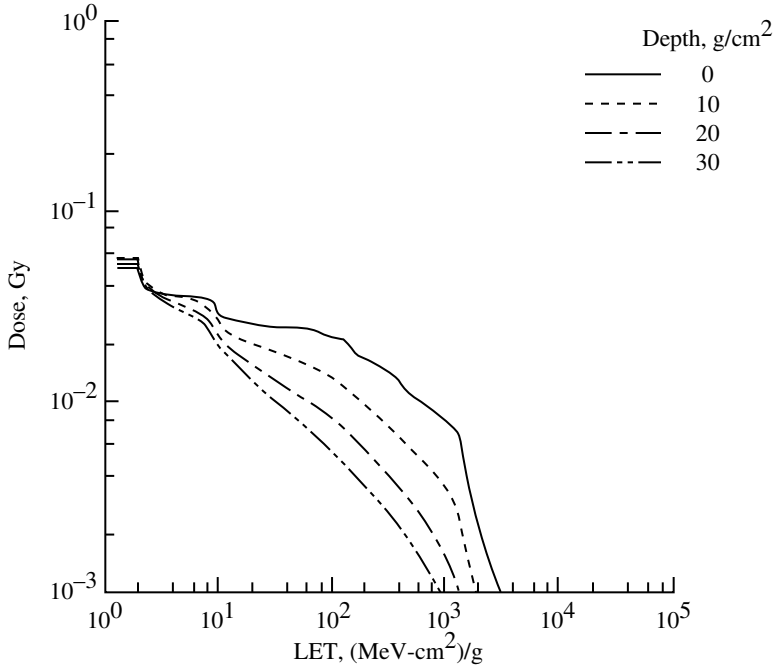

(b) 1981 solar maximum.

Figure 45. GCR skin dose LET spectra in water.

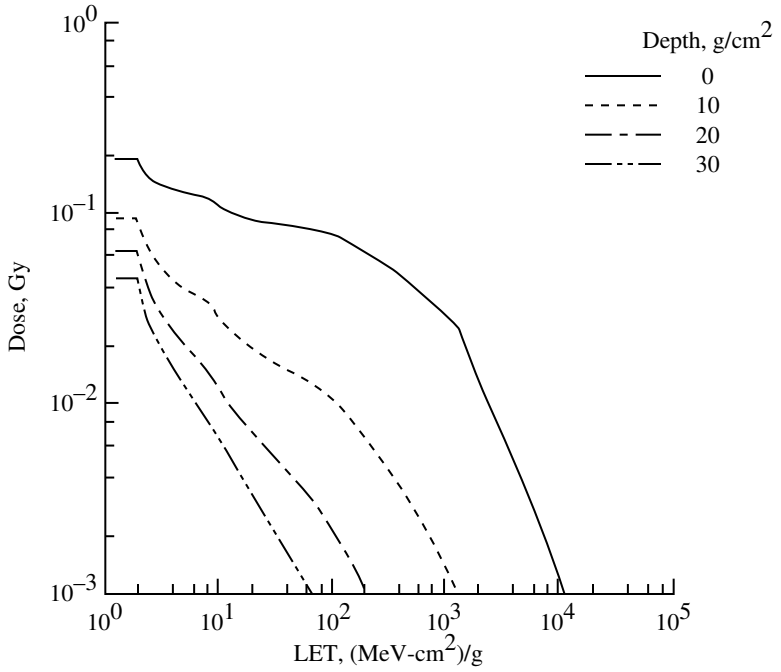

(a) 1977 solar minimum.

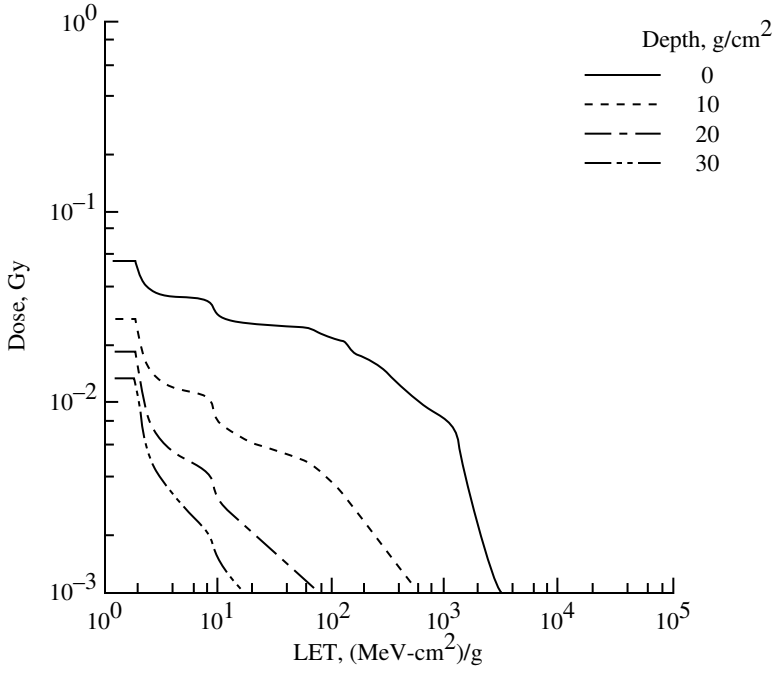

(b) 1981 solar maximum.

Figure 46. GCR skin dose LET spectra in liquid hydrogen.

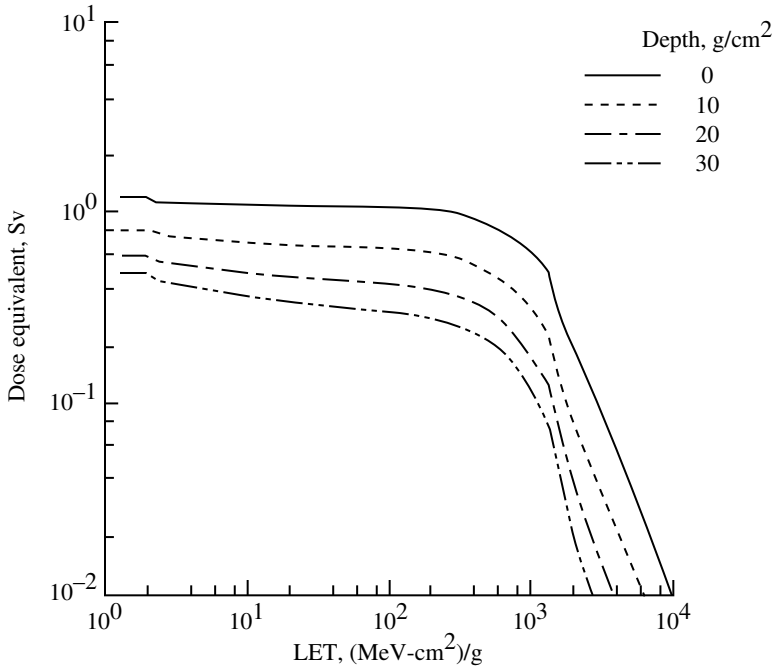

(a) 1977 solar minimum.

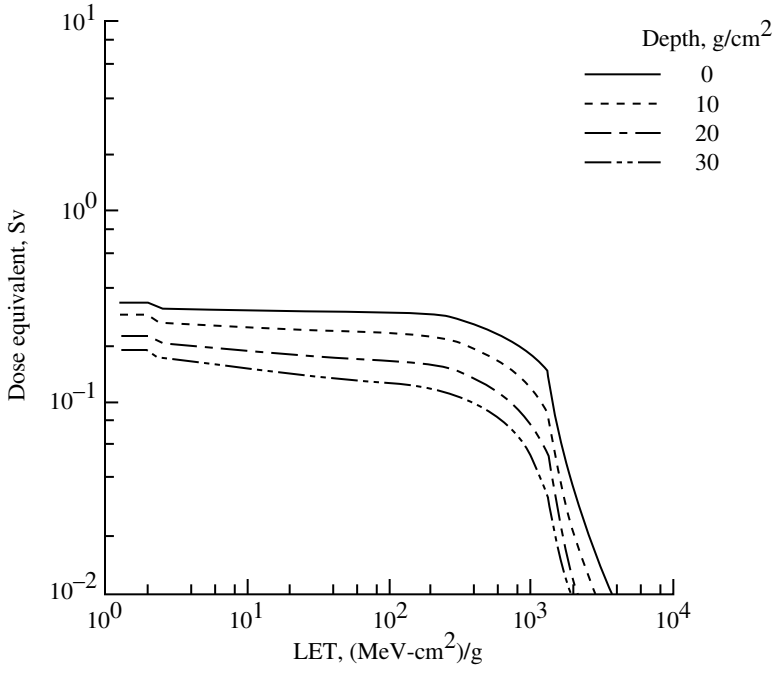

(b) 1981 solar maximum.

Figure 47. GCR skin dose equivalent LET spectra in aluminum.

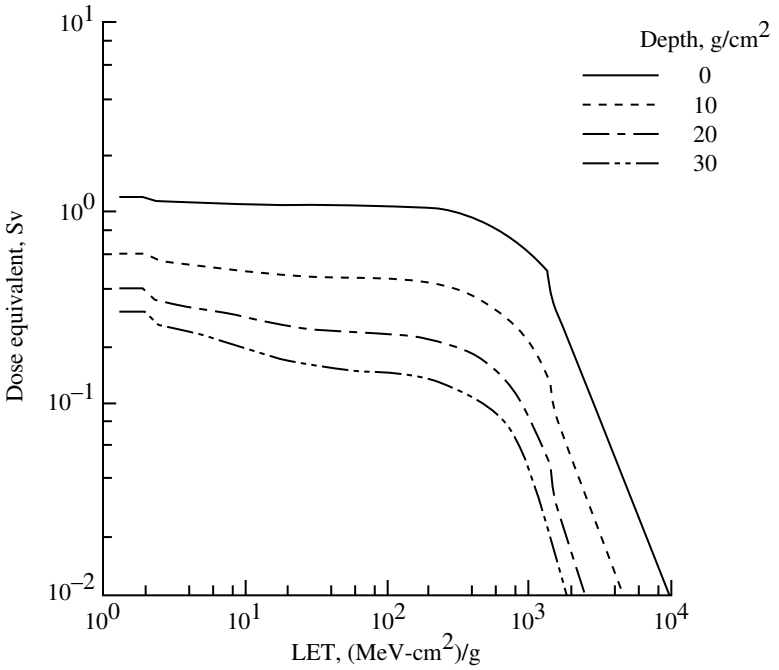

(a) 1977 solar minimum.

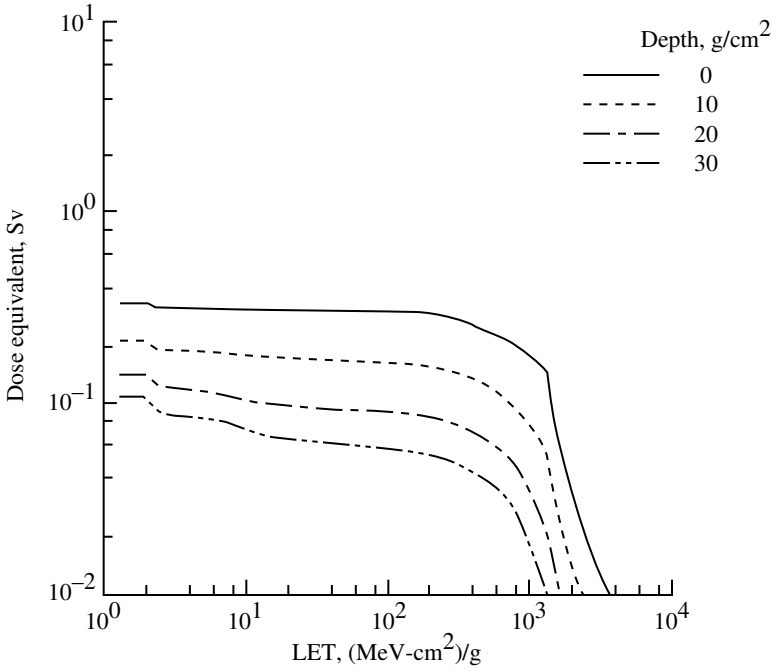

(b) 1981 solar maximum.

Figure 48. GCR skin dose equivalent LET spectra in water.

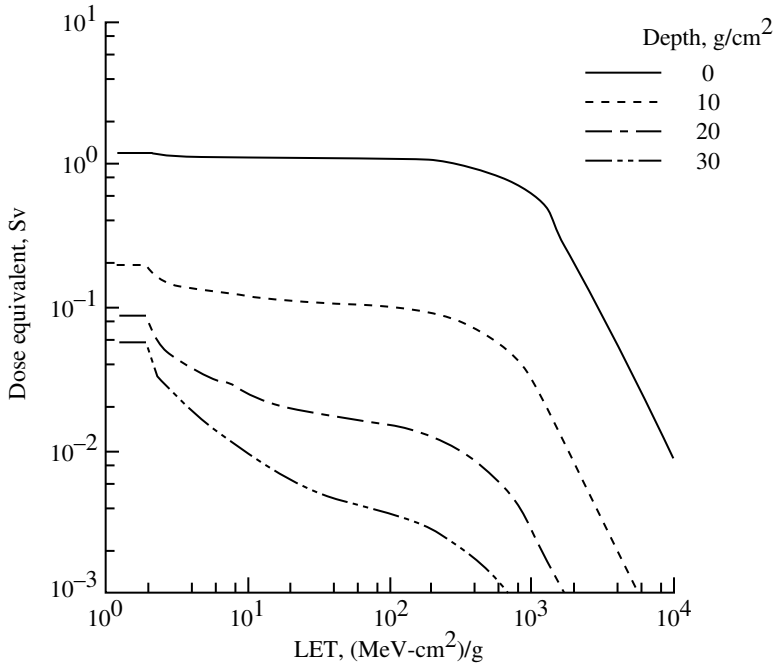

(a) 1977 solar minimum.

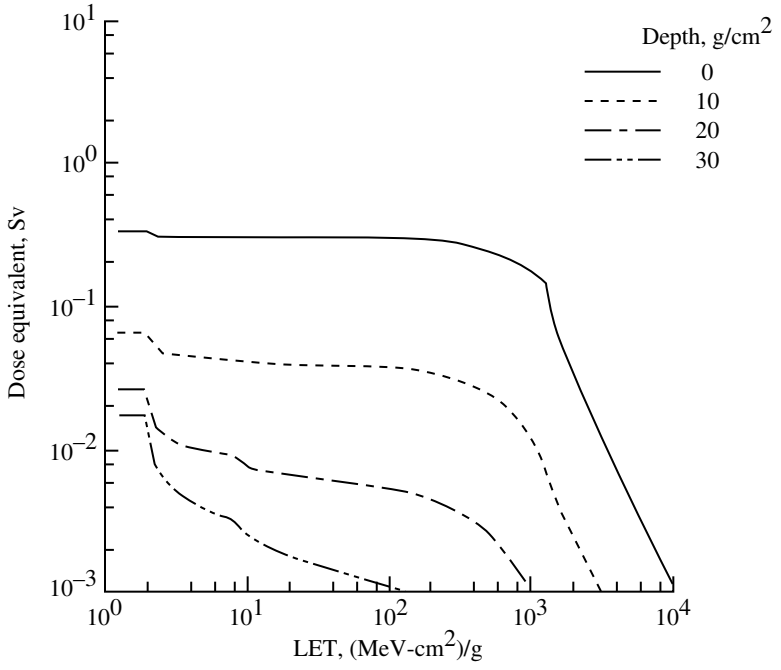

(b) 1981 solar maximum.

Figure 49. GCR skin dose equivalent LET spectra in liquid hydrogen.

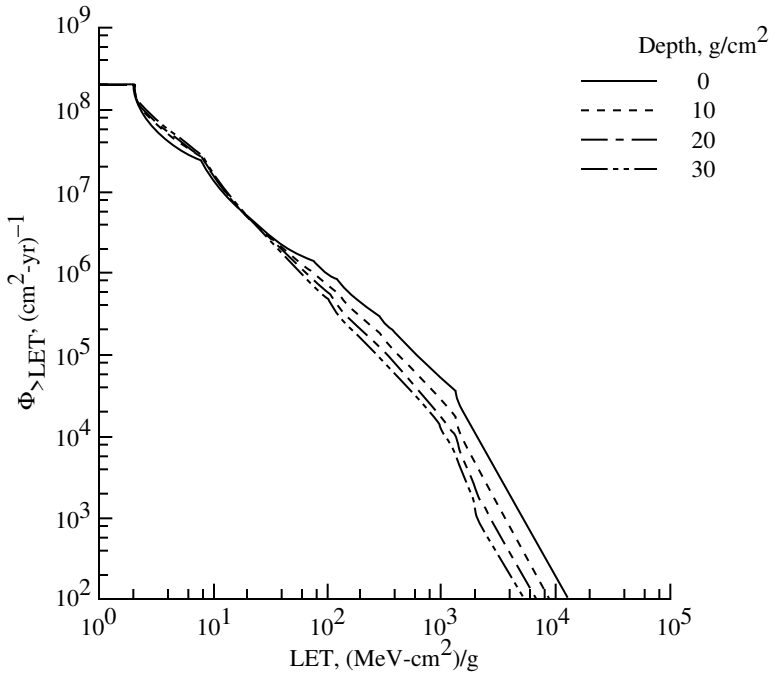

(a) 1977 solar minimum.

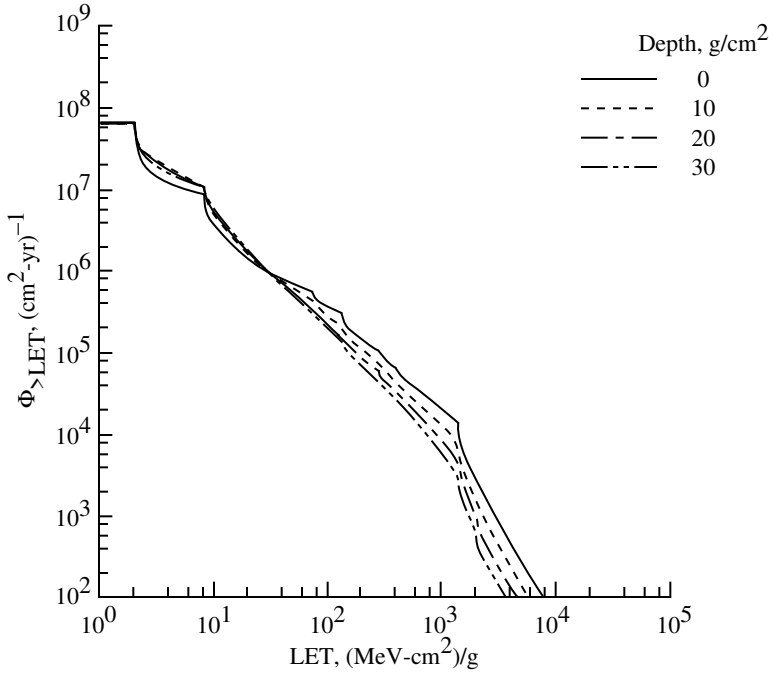

(b) 1981 solar maximum.

Figure 50. GCR 5-cm-BFO integral flux LET spectra in aluminum.

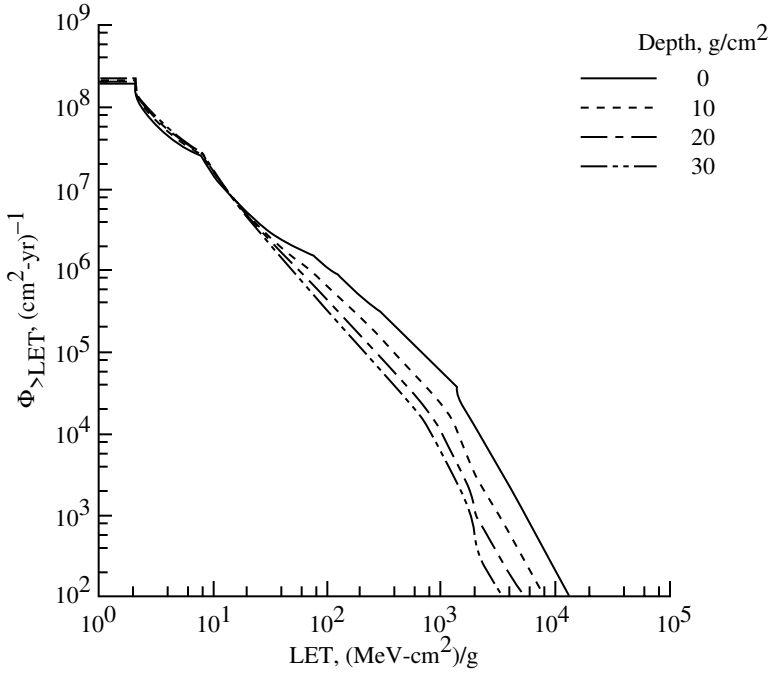

(a) 1977 solar minimum.

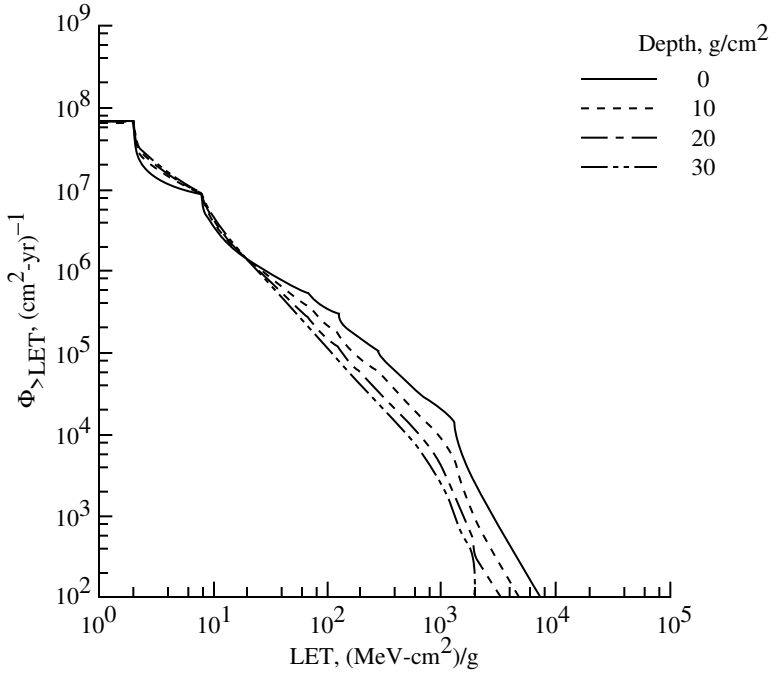

(b) 1981 solar maximum.

Figure 51. GCR 5-cm-BFO integral flux LET spectra in water.

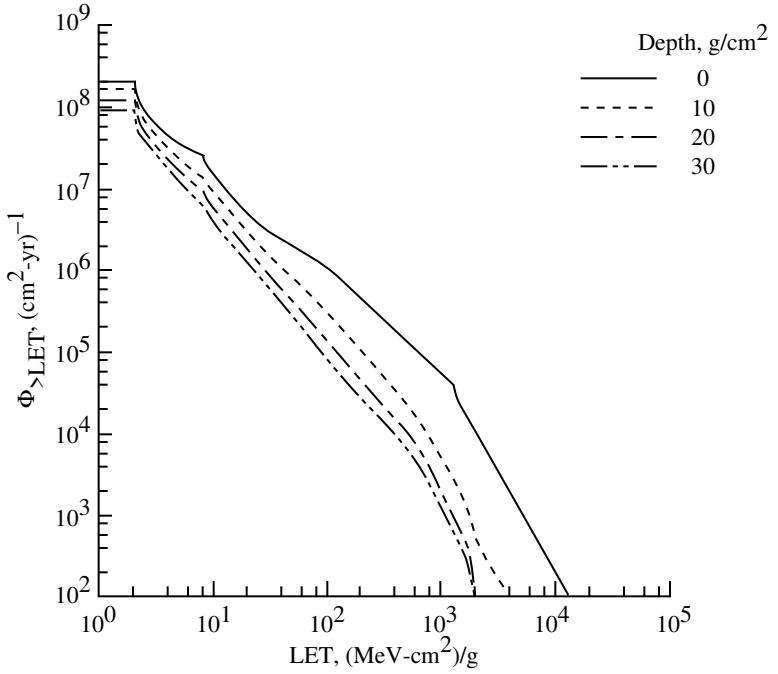

(a) 1977 solar minimum.

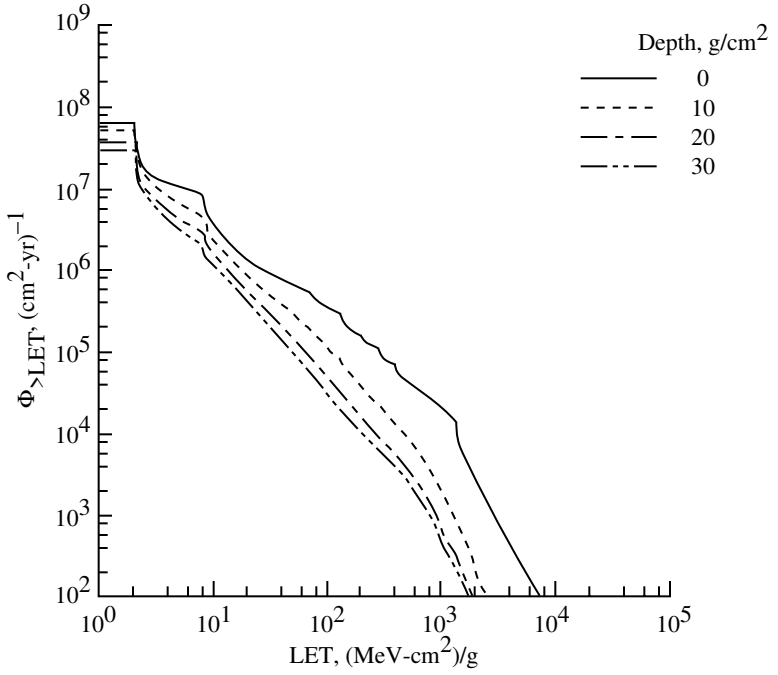

(b) 1981 solar maximum.

Figure 52. GCR 5-cm-BFO integral flux LET spectra in liquid hydrogen.

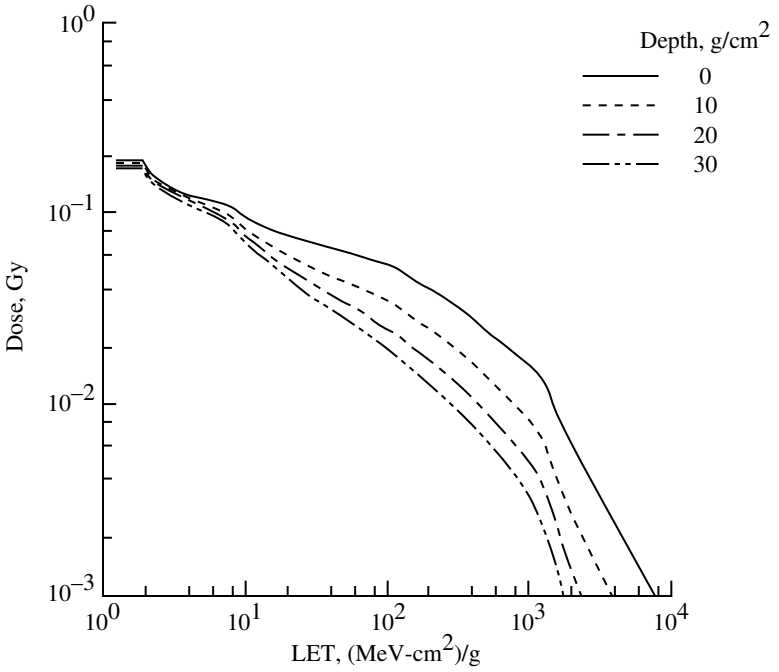

(a) 1977 solar minimum.

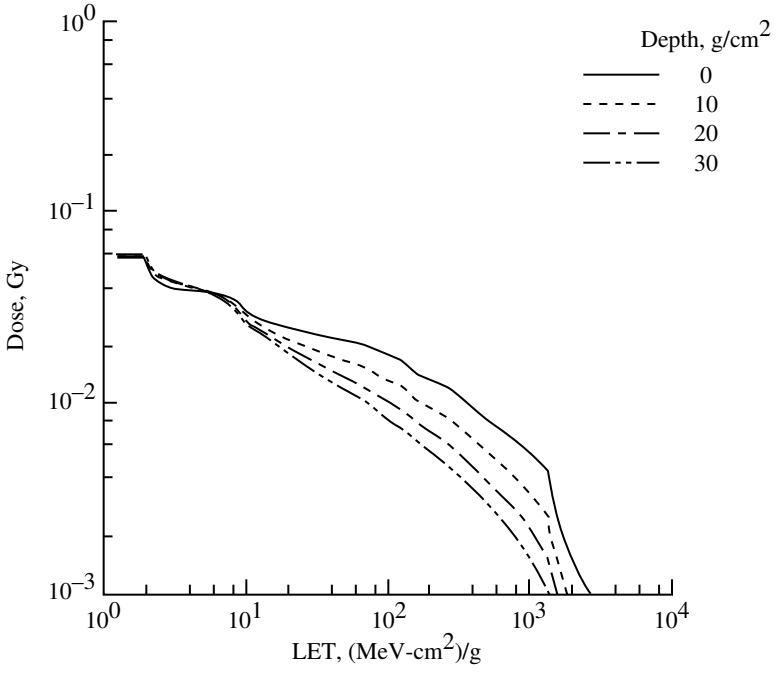

(b) 1981 solar maximum.

Figure 53. GCR 5-cm-BFO dose LET spectra in aluminum.

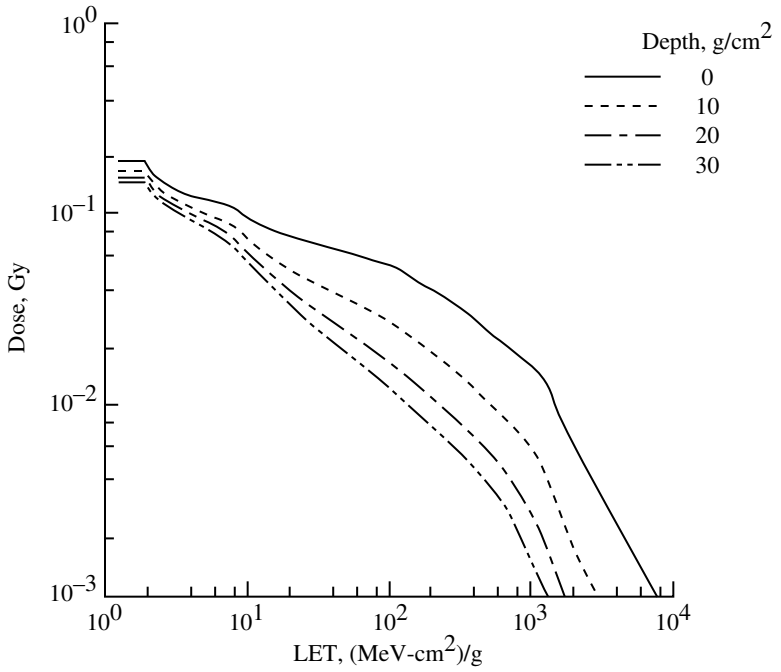

(a) 1977 solar minimum.

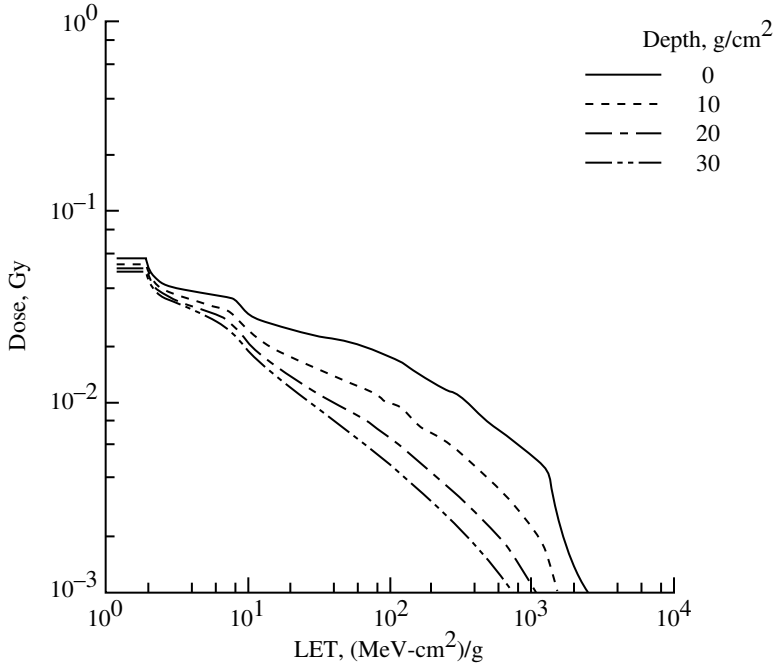

(b) 1981 solar maximum.

Figure 54. GCR 5-cm-BFO dose LET spectra in water.

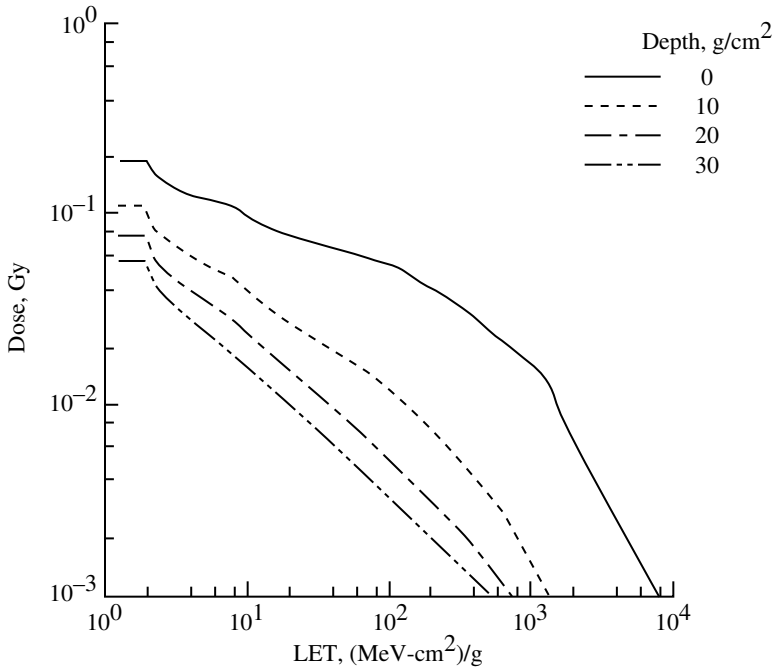

(a) 1977 solar minimum.

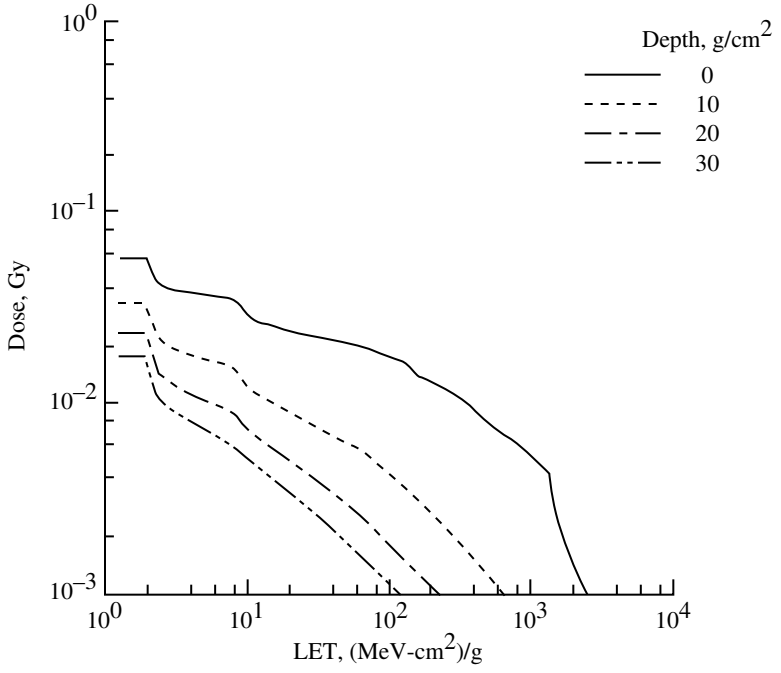

(b) 1981 solar maximum.

Figure 55. GCR 5-cm-BFO dose LET spectra in liquid hydrogen.

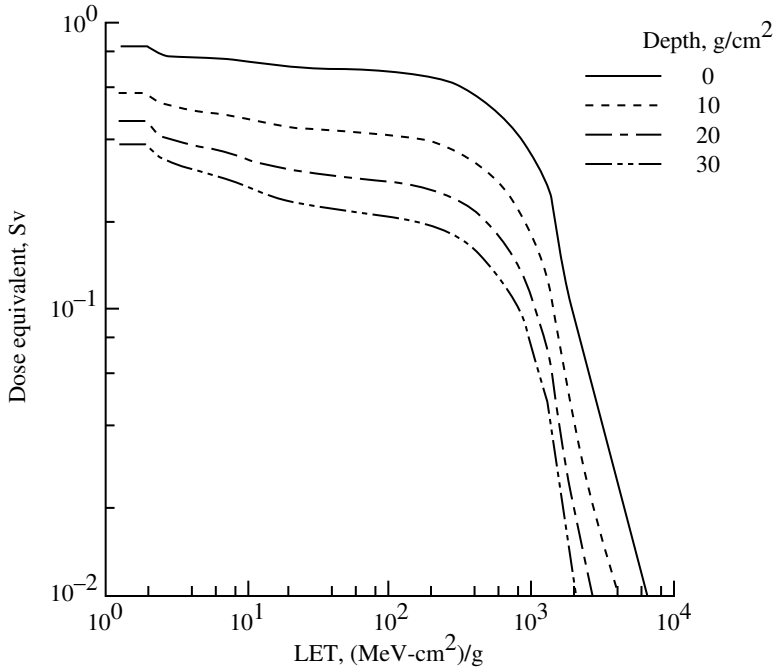

(a) 1977 solar minimum.

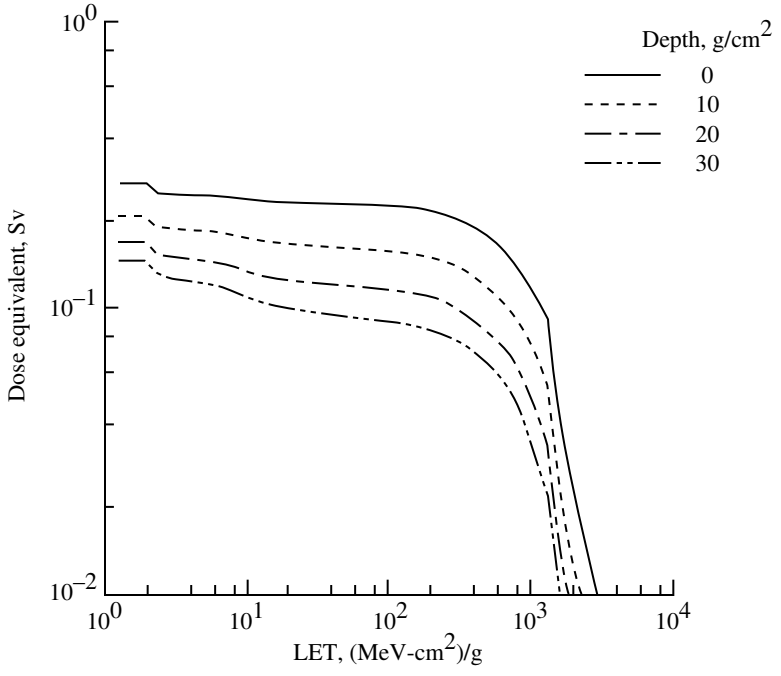

(b) 1981 solar maximum.

Figure 56. GCR 5-cm-BFO dose equivalent LET spectra in aluminum.

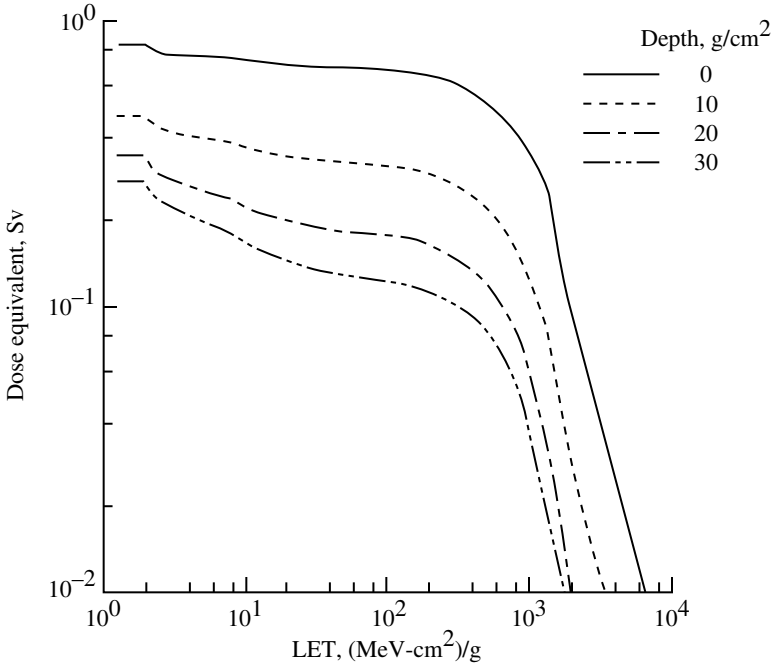

(a) 1977 solar minimum.

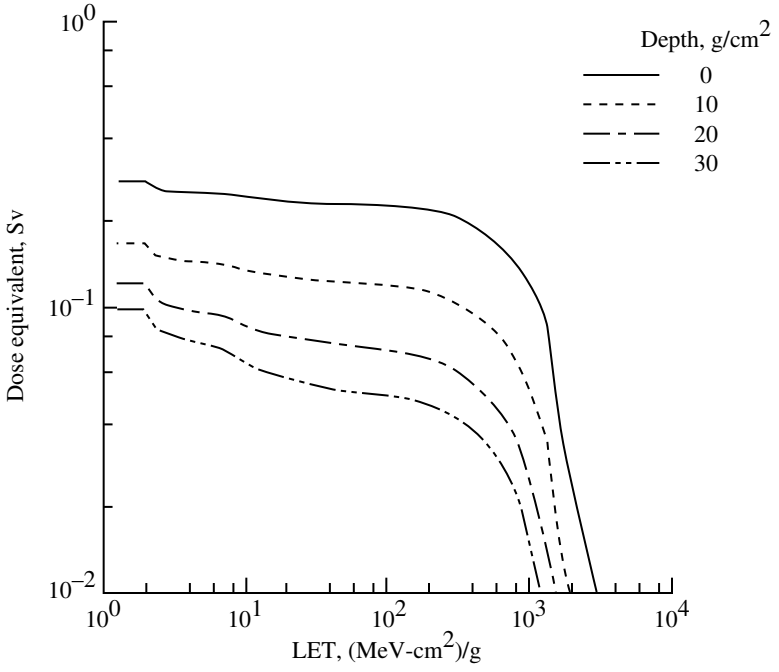

(b) 1981 solar maximum.

Figure 57. GCR 5-cm-BFO dose equivalent LET spectra in water.

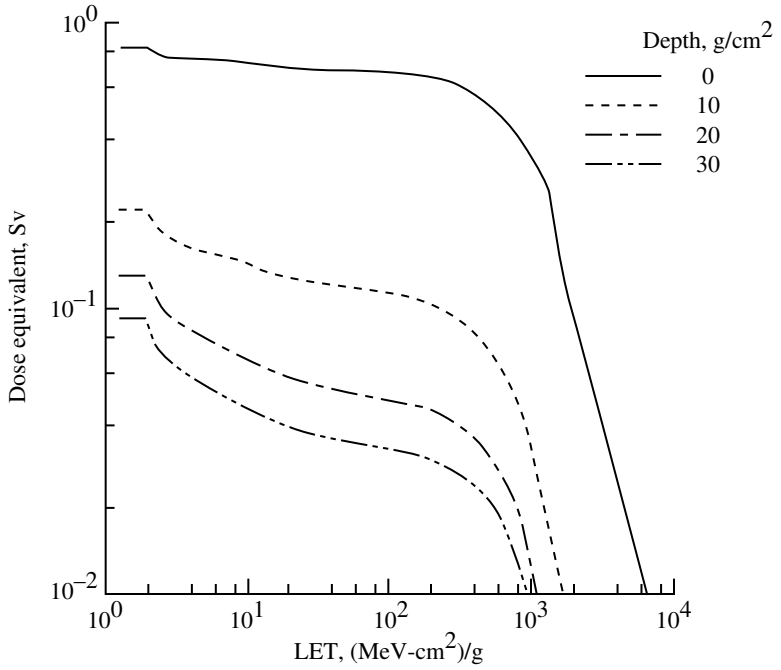

(a) 1977 solar minimum.

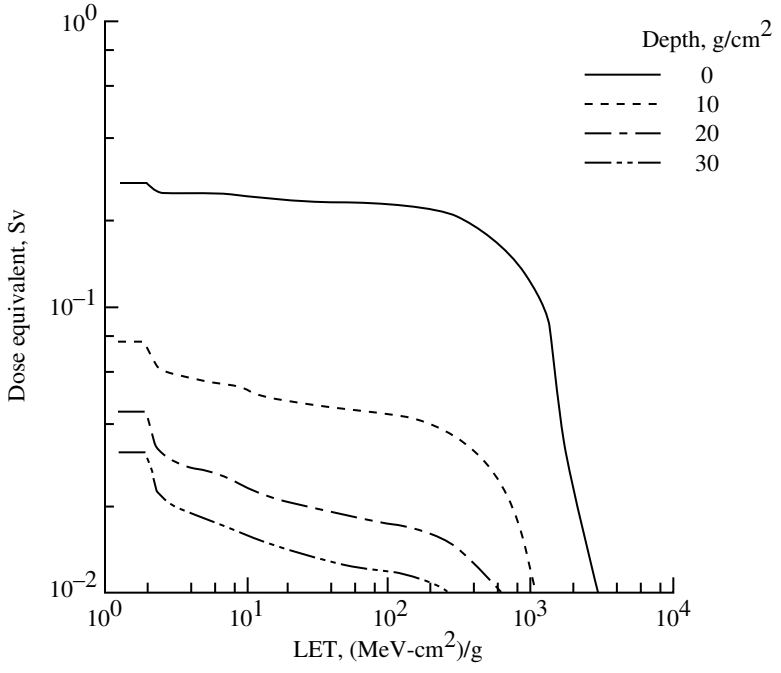

(b) 1981 solar maximum.

Figure 58. GCR 5-cm-BFO dose equivalent LET spectra in liquid hydrogen.

REPORT DOCUMENTATION PAGE

Form Approved
OMB No. 0704-0188

1. AGENCY USE ONLY *(Leave blank)*	2. REPORT DATE	3. REPORT TYPE AND DATES COVERED
	May 1995	Technical Paper

4. TITLE AND SUBTITLE
HZETRN: Description of a Free-Space Ion and Nucleon Transport and Shielding Computer Program

5. FUNDING NUMBERS
WU 199-45-16-11

6. AUTHOR(S)
John W. Wilson, Francis F. Badavi, Francis A. Cucinotta, Judy L. Shinn, Gautam D. Badhwar, R. Silberberg, C. H. Tsao, Lawrence W. Townsend, and Ram K. Tripathi

7. PERFORMING ORGANZATION NAME(S) AND ADDRESS(ES)
NASA Langley Research Center
Hampton, VA 23681-0001

8. PERFORMING ORGANIZATION REPORT NUMBER
L-17417

9. SPONSORIING/MONITORING AGENCY NAME(S) AND ADDRESS(ES)
National Aeronautics and Space Administration
Washington, DC 20546-0001

10. SPONSORING/MONITORING AGENCY REPORT NUMBER
NASA TP-3495

11. SUPPLEMENTARY NOTES
Wilson, Cucinotta, Shinn, and Townsend: Langley Research Center, Hampton, VA; Badavi and Tripathi: Christopher Newport University, Newport News, VA; Badhwar: Johnson Space Center, Houston, TX; Silberberg: Universities Space Research Association, Washington, D.C.; Tsao: Naval Research Laboratory, Washington, D.C. Software and documentation are available as LAR-15225 through COSMIC, 382 E. Broad Street, University of Georgia, Athens, GA 30602.

12a. DISTRIBUTION/AVAILABILITY STATEMENT
Unclassified–Unlimited
Subject Category 93
Availability: NASA CASI (301) 621-0390

12b. DISTRIBUTION CODE

13. ABSTRACT *(Maximum 200 words)*
The high-charge-and-energy (HZE) transport computer program HZETRN is developed to address the problems of free-space radiation transport and shielding. The HZETRN program is intended specifically for the design engineer who is interested in obtaining fast and accurate dosimetric information for the design and construction of space modules and devices. The program is based on a one-dimensional space-marching formulation of the Boltzmann transport equation with a straight-ahead approximation. The effect of the long-range Coulomb force and electron interaction is treated as a continuous slowing-down process. Atomic (electronic) stopping power coefficients with energies above a few A MeV are calculated by using Bethe's theory including Bragg's rule, Ziegler's shell corrections, and effective charge. Nuclear absorption cross sections are obtained from fits to quantum calculations and total cross sections are obtained with a Ramsauer formalism. Nuclear fragmentation cross sections are calculated with a semiempirical abrasion-ablation fragmentation model. The relation of the final computer code to the Boltzmann equation is discussed in the context of simplifying assumptions. A detailed description of the flow of the computer code, input requirements, sample output, and compatibility requirements for non-VAX platforms are provided.

14. SUBJECT TERMS
Space radiation; Heavy ions; Shielding

15. NUMBER OF PAGES
146

16. PRICE CODE
A07

17. SECURITY CLASSIFICATION OF REPORT	18. SECURITY CLASSIFICATION OF THIS PAGE	19. SECURITY CLASSIFICATION OF ABSTRACT	20. LIMITATION OF ABSTRACT
Unclassified	Unclassified	Unclassified	